SPRINGER BRIEFS IN PHYSICS

Suzairi Daud
Sevia Mahdaliza Idrus
Jalil Ali

Simulation of Optical Soliton Control in Micro- and Nanoring Resonator Systems

Springer

SpringerBriefs in Physics

More information about this series at http://www.springer.com/series/8902

Suzairi Daud · Sevia Mahdaliza Idrus
Jalil Ali

Simulation of Optical Soliton Control in Micro- and Nanoring Resonator Systems

Springer

Suzairi Daud
Laser Centre, Ibnu Sina ISIR
Universiti Teknologi Malaysia
Johor Bahru
Malaysia

Jalil Ali
Laser Centre, Ibnu Sina ISIR
Universiti Teknologi Malaysia
Johor Bahru
Malaysia

Sevia Mahdaliza Idrus
Department of Communication
Engineering, Faculty of Electrical
Engineering
Universiti Teknologi Malaysia
Johor Bahru
Malaysia

ISSN 2191-5423 ISSN 2191-5431 (electronic)
SpringerBriefs in Physics
ISBN 978-3-319-15484-8 ISBN 978-3-319-15485-5 (eBook)
DOI 10.1007/978-3-319-15485-5

Library of Congress Control Number: 2015933366

Springer Cham Heidelberg New York Dordrecht London

Printed on acid-free paper

Springer International Publishing AG Switzerland is part of Springer Science+Business Media (www.springer.com)

Preface

Praise be to Allah s.w.t… Peace and Blessing be to Prophet Muhammad s.a.w…

In preparation of this research book, we were in contact with numerous researchers and academicians. They have contributed toward the understanding and thoughts of Physics and communication systems link. In particular, we wish to express our sincere appreciation and gratitude to Prof. Dr. Preecha P. Yupapin from KMITL, Thailand, Prof. Dr. Noriah Bidin from Laser Centre, Ibnu Sina ISIR, and Dr. Saktioto from the Physics Department, Universiti Teknologi Malaysia for their motivations and support. Also, we like to thank our family members for their patience. Without their continued support and interest, the completion of this book would definitely have been impossible.

This research book serves to design and analyze the optical soliton control in micro- and nanoring resonator systems. Optical soliton control in communication and sensors is performed with the ring resonator systems described in the book. The ring resonator systems are optimized as optical tweezers for photodetection. Numerous arrangements and configurations of micro- and nanoring resonator systems are explained. The analytical formulation and optical transfer function for each model and the interaction of the optical signals in the systems are discussed. The book shows that the models designed are able to control the dynamical behavior of generated signals.

This research book consists of six chapters, namely as Introduction, Literature Review, Theory, Research Methodology, Results and Discussion, and Conclusion. The background of study, problem statements, scope, and significance of research is discussed in Chap. 1. The objectives of the research are also explained in details. Literature reviews of the research are discussed in Chap. 2. The characteristics of bright and dark solitons, temporal solitons, optical trapping, and historical perspective of ring resonators are described in this chapter. Chapter 3 explains the theoretical part of the research. The fundamental principles of ring resonator are discussed in details. The nonlinearity of the optical solitons is discussed based on the Kerr effect of optical fibre waveguides. The resonance characteristics of the fibre is also presented. Besides, the basic principles of SPM, SFG, and Z-transform

methods are also explained in this chapter. The mathematical formulation, modeling, and description of add-drop and PANDA ring resonator systems are explained in Chap. 4. The derivation of add-drop and PANDA ring resonator systems arrangements are discussed precisely. The transfer function of each model designed is derived based on the actual practical device values. The flowcharts that perform the simulation processes are described. Chapter 5 explains the results and discussions of the research findings. All parametric effects toward the system performance are discussed in details. The optimization process for both add-drop and PANDA ring resonator systems are explained accordingly. At the end, the conclusions of this research work are described in Chap. 6.

Contents

Abbreviations and Symbols

Abbreviations

FSR	Free spectral range
FWHM	Full width at half maximum
GVD	Group velocity dispersion
IDRI	Intensity dependent refractive index
MRR	Microring resonator
NLS	Nonlinear Schrödinger
NRR	Nanoring resonator
PMMA	Polymethyl methacrylate
SFG	Signal flow graph
SHG	Second harmonic generation
SOA	Semiconductor optical amplifier
SPM	Self-phase modulation
XPM	Cross-phase modulation

Symbols

A	Amplitude
A_{eff}	Effective mode core area
a	Acceleration
B	Build-up factor
c	Speed of light
D	Delay dispersion parameter
dB	Decibel
$\mathrm{dBkm^{-1}}$	Decibel per kilometre
E	Electric field
E_{add}	Add port
E_d	Drop port

E_{in}	Input port
E_t	Throughput port
E_1	Circulating field 1
E_2	Circulating field 2
E_3	Circulating field 3
E_4	Circulating field 4
F	Finesse
F_g	Gradient force
F_{net}	Net force
F_s	Scattering force
f	Frequency
f_o	Center frequency
GHz	Giga Hertz
h	Plank's constant (6.63 x 10^{-34} m^2kg/s)
I	Intensity
I_o	Peak intensity
k	Wave number
k_n	Propagation constant
L	Propagation distance
L_D	Dispersion length
L_{eff}	Effective length
L_L	Circumference of left ring
L_{NL}	Nonlinear length
L_R	Circumference of right ring
L_u	Smallest path length or the unit delay length
m	Mass
mW	miliWatt
N	Number of photon
n	Refractive index
nm	nanometer
ns	nanosecond
nL	Optical path length
n_{eff}	Effective refractive index
n_g	Group refractive index
n_o	Linear refractive index
n_2	Nonlinear refractive index
P	Dielectric polarization
P_L	Linear polarization
P_{NL}	Nonlinear polarization
P_t	Transmission power
p	Momentum
pm	pikometre
Q	Quality factor
R	Ring radius
R_L	Radius of left nanoring

R_R	Radius of right nanoring
s	Electron travelling distance
T	Unit delay
T_o	Pulse propagating time at initial input
t	Time
t_{ij}	Transmittance
u_1	Inertial velocity
u_2	Final velocity
v	Velocity
W	Watt
τ	Pulse duration
ϕ	Instantaneous phase shift of the pulse
ϕ_L	Linear phase
ϕ_{NL}	Nonlinear phase
κ	Coupling coefficient
λ	Wavelength
λ_o	Center wavelength
θ	Angle
θ_1	Incident angle
θ_2	Refractive angle
ω	Optical frequency
ω_0	Reference frequency
ω'	Instantaneous frequency
β	Propagation constant
v_c	Center frequency
γ	Coupling loss
μm	micrometer
μm^2	micrometer square
ϕ	Phase shift
ϕ_o	Linear phase shift
ϕ_{NL}	Nonlinear phase shift
*	Conjugate
α	Loss coefficient
β	Propagation constant
|t|	Coupling losses
φ_t	Phase of coupler
ε_o	Vacuum permittivity
χ_{eff}	Effective susceptibility of the medium
$\chi^{(1)}$	Linear susceptibility
$\chi^{(2)}$	Second-order susceptibility
$\chi^{(3)}$	Third-order susceptibility
Δf	Frequency shift
Δn	Change in refractive index

$\Delta\lambda$	Wavelength shift
$\Delta\phi$	Phase change
γ	Coupling loss
Γ	Length scale
3-D	Three dimensional

Abstract

Over the past few years, the development of optical soliton technologies has progressed rapidly. This research book has been written to design and analyze the optical soliton control in micro- and nanoring resonator systems. The add-drop and PANDA ring resonator systems have been proposed for optical soliton control in communications, sensors, and biological applications. The operating system consists of a modified nonlinear add-drop configuration system based on InGaAsP/InP fibre materials integrated with a series of nonlinear nanoring resonators. Numerous arrangements and configurations of micro- and nanoring resonator systems were designed. The analytical formulation and optical transfer function for each model designed were developed based on these configurations and Z-transform method was used to derive and prove the interaction of the optical signals for the systems. Both the add-drop and PANDA ring resonator systems could be optimized as optical tweezers for photodetection by controlling the input power, ring radii, and coupling coefficients of the systems. The system was tuned to trap and accelerate the particles. The system named as optical multiplexer can be used to optimize the channel capacity and security of the signals. In conclusion, this research shows that the models designed are able to control the dynamical behavior of the generated signals.

Chapter 1
Introduction

1.1 Background of Study

Solitons or solitary waves, have been the subject of theoretical and experimental studies in different fields, including hydrodynamics, nonlinear optics, plasma physics, engineering, sensors, and biology (Ablowitz and Clarkson 1991; Abdullaev et al. 1993; Drazin 1993; Gu 1995). The first investigation about the solitons was reported by James Scott Russel in 1834, which observed that a heap of water in canal propagated undistorted over several kilometres (Neuman et al. 2007). However, the properties of the solitons were not completely understood yet, even different mathematical models were introduced.

The terms solitons was coined in 1965 to reflect the particle-like nature of solitary waves that remained intact even after mutual collisions. In mathematics and physics, soliton is a self-reinforcing solitary wave that maintains its shape while it travels at the constant speed (Newell 1995). In the context of nonlinear optics, solitons can be classified to being either temporal or spatial solitons depending on whether the confinement of light occurs in time or space during the wave propagation (Shen 1984; Boyd 2001).

Various types of single-molecule force spectroscopy technique such as optical tweezers, magnetic tweezers, and atomic force microscopy have been invented to investigate tiny forces and motion associated with micro and nano-scaled particles. Among these techniques, optical tweezers is considered as one of the most successful technique for ultrafine positioning, measurement, and confinement of nanoscopic object. Since its interception in early 1970s, the field of optical tweezers has developed rapidly.

S. Daud et al., *Simulation of Optical Soliton Control in Micro- and Nanoring Resonator Systems*, SpringerBriefs in Physics, DOI 10.1007/978-3-319-15485-5_1

1.2 Problem Statement

Development of the optical soliton technology is typically very important because of its potential and diverse technological applications from communication to biological (Crisafuli et al. 2012). They have shown that such nonlinear behaviours are beneficial for various fields, such as signal processing, digital encoding, bistability switching, and others. However, the power attenuation of the signal output becomes a big problem for the large system link. For this reason, a suitable system is required to generate large bandwidth signal using soliton pulse propagates in a Kerr type nonlinear medium (Liu and Zhao 2012).

Tuned soliton pulses are obtained using add-drop and PANDA multiplexers. The characterization and optimization of the proposed systems are very important indeed. In this research, the optical soliton control in microring resonator (MRR) and nanoring resonator (NNR) systems will be studied including the characteristics of the systems, optical soliton nonlinear equations, and soliton interaction within the MRR and NNR systems.

Recently, this device has found its role in development of dynamic optical tweezers by employing the concept of dark soliton pulse controlled by Gaussian beam within the resonator system. Due to these special characteristics, the development of dynamic optical tweezers using dark soliton pulse been typically important in the research field with potential applications in various areas (Harada and Asakura 1996).

Thus, characterization and optimization of the systems are very crucial element that need to be considered. Development of ring resonator models with its analytical derivations and optimization of the output transmission will be studied in details. Analysing and examining the results establish a better understanding on the physics knowledge.

1.3 Research Objective

The general aims of this research are to design, demonstrate, control and analyze the optical soliton within the optical ring resonator systems.

The specific objectives of this research are:

(i) To design a number of different arrangements/configurations of micro- and nanoring resonator systems integrated with add-drop and PANDA configuration systems.
(ii) To develop the analytical formulation and derivation of the transfer function and examine the parametric effect of each proposed model designs.
(iii) To investigate and analyze the parametric effects on the dynamical behaviour of the signals within MRR and NRR systems.
(iv) To optimize the ring resonator parameters for specific applications.

1.4 Scope of Research

This research starts with the literature review on optical soliton control in ring resonator systems. The theoretical part involves in numerical experiments on several arrangements of integrated ring resonator systems consisting of micro-size ring resonator as the main component, couples with nano-size ring resonators embedded on the structure. Different arrangements of micro- and nanorings resonator systems will be designed for the purpose. The configurations of add-drop and PANDA ring resonator systems are integrated and described in details.

The proposed systems consist of an active ring resonator made of nonlinear material called InGaAsP/InP with core refractive index, n_o = 3.34. During simulation process, the coupling coefficient, κ is set to be in range of 0–1, and the ring radii are vary from 20 to 40 μm for microring and 40–90 nm for nanoring resonators respectively. This research focused on the application in communication and sensor technologies.

Nonlinear optics, optical solitons, optical Kerr effect, group velocity dispersion (GVD), and self-phase modulation (SPM) are discussed thoroughly. The derivations of the equations used are based on the nonlinear Schrödinger (NLS) equation, Kerr effect, and Z-transform method. Dark soliton pulse is introduced into the systems through the input port, E_{in}. The important aspects including the power input, ring resonator arrangements, ring radii, coupling coefficient, losses of the systems, fibre wavelength, and depth of the ring resonators will be optimized. A numerical method is developed based on Z-transform analysis and the results are simulated using MatLab R2010b software programming.

1.5 Significance of Research

Dynamical optical tweezers in form of potential well can be used in communication systems and frontier research for trapping and transporting dielectric particles. The research leads us to a better understanding and qualifying the physics of such systems that will give direct knowledge, especially in communication and biological technologies. The proposed models designed are able to predict accurately the dynamical behaviour of optical soliton interactions within the micro- and nanoring resonator systems.

Chapter 2
Literature Review

2.1 Introduction

This chapter begins with the historical perspectives of the optical solitons. The bright and dark solitons characteristics are studied. In addition, the historical backgrounds of the ring resonators, including micro- and nanoring resonators are also discussed in details. Finally, the potential applications related to this research work are reviewed.

2.2 Historical Background

A German astronomer, Johannes Kepler was first purposed the radiation pressure theory in 1619 (Chen et al. 2009). Radiation pressure is the pressure associated with the interaction of electromagnetic radiation on any given surface. He managed to explain physical phenomenon of comet tails which always pointing away from the sun because of the radiation pressure exert by sunlight (Svoboda and Block 1994).

In 1873, James Clerk Maxwell proposed the electromagnetism theory (Ashkin 1997) and described the existence of extremely small optical forces associated with electromagnetic fields. He managed to explain the electromagnetism theory precisely. However, the existence of this tiny optical force on absorbing gasses and microscopic objects was described by Russia physicist, Peter Lebedev in 1901 (Ashkin 2000). Since that time, this field has undergone a slow-moving development and innovation due to its feeble magnitude and insignificant impact on particles.

This field of study continues to grow tremendously after the invention of light amplification of stimulated emission of radiation in 1960s (Pralle et al. 2000) known as laser. Laser ensures the high intensities and collimated light which become very useful in enhancing radiation pressure. Advent of laser has enabled numerous of research and developments in this area.

S. Daud et al., *Simulation of Optical Soliton Control in Micro- and Nanoring Resonator Systems*, SpringerBriefs in Physics, DOI 10.1007/978-3-319-15485-5_2

2.3 Bright and Dark Solitons

Solitons are the localized excitations propagating in a system with constant velocity colliding with each other without change in their shape (Sarapat et al. 2009). Soliton can be divided into two, which are bright and dark solitons.

In the case of self-defocusing, the general form of the bright soliton is given as (Kivshar and Agrawal 2003):

$$u(z,x) = A\,\mathrm{sech}[A(x - vz)]\exp i[vz + (\varphi(z,x))] \tag{2.1}$$

where A is the amplitude of the soliton and v is its velocity.

In the self-defocusing Kerr medium, the continuous-wave plane-wave soliton is always stable against small modulation. The dark soliton can be stated as (Chen et al. 2012):

$$u(z,x) = u_o\{B\tanh[u_oB(x - Au_oz)] + iA\}\exp\left(-iu_o^2z\right) \tag{2.2}$$

where $A^2 + B^2 = 1$.

In the special case, (when $\phi = 0$) dark soliton doesn't move against the background and it is kept in stationary condition (Masi et al. 2010). In this case, (2.2) reduced to:

$$u(z,x) = u_o\tanh(u_ox)\exp\left(-iu_0^2z\right) \tag{2.3}$$

The characteristics of the bright soliton depend on the amplitude, A and the velocity, v while the speed of the dark soliton depends on its amplitude through the parameter ϕ.

2.4 Optical Trapping

The field of optical trapping was pioneered introduced by Arthur Ashkin in early 1970 (Ashkin 1997). The usage of intense laser beam has overcome the major problem of extremely small magnitudes of optical forces. Realization of the large magnitudes of optical forces allows this phenomenon to be studied well. His first experimental works are considered as an important breakthrough in this research area. By using forces of radiation pressure from a continuous wave visible laser source, he managed to observe the acceleration of freely suspended micron-size particles. This work have led to the first process of trapping particles in optical potential well which created by using two identical counter propagating laser beams. The stability of the potential well arises from the combination of radiation pressure and gradient force of the laser.

Arthur Ashkin following work is on the optical levitation process. In this work, he has experimentally demonstrated stable levitation of transparent glass sphere by using a laser in different types of medium. During experiment, light beam are directed to strikes a sphere with higher refractive index, n compared to the surrounding medium where it was suspended. This process has successfully proved the existence of another component of force which tends to push the trapped particles towards the center of the beam, which is the region where light intensity is highest. Discovery of the force provides a better understanding on possibilities to create a stable optical potential wells by using a single laser beam.

The potential shown by this technique is the main reason why this technique went into numbers of theoretical and experimental studies over the decades. Levitation of different particles in different medium such as in air and vacuum has been demonstrated in various kinds of research and studies. During those invention years, one of the most important studies has been carried out on optical levitation of liquid drops (Rafizadeh 1997). The study has discovered that not only solid particles can be trapped, but this technique also works on liquid particles. The journal also highlights on some important elements that need to be considered, such as trapping of multiple particle and its restriction.

This technique continues to evolve as time goes by. Finally in 1986, a major breakthrough on this technique has been recorded in history. Ashkin and his co-workers at Bell Labs went into successful discovery on new method to trap a particle by using only single laser beam. This technique is called "single-beam force trap" or commonly referred to as an optical tweezers (Ashkin 2000). Technically, the generation of optical tweezers involves process of focusing a laser beam upon a high numerical aperture microscope objective lens in water immersion. This step allows a strong convergent ray of light to be focused in a small area, which contains very strong electric field gradients compare to the one produced in previous experiment using a normal laser beam. During experiments, it turns out that particles are attracted along the gradient towards the center of the beam with high intensity observed. Geometry of the particle thus allows the forces to be stabilized in transverse direction.

In previous levitation process, axial gradient force is too small that just enough to balanced up with gravitational force to ensure the axial stability. They have shown that by using extremely focused laser beam, magnitude of the force produced is very large that it dominates the axial stability of the trap. By considering geometry of the particle, contributions from both components of forces are enough to ensure the capability of this optical tweezers to hold microscopic particle stable in 3 dimensions. They managed to extend the size regime of trapping for various applications covering macromolecules, colloids, aerosol particles and look into possibility in trapping of biological particles.

However, there are lots of arguments that have been considered on trapping biological specimens since there appear no experimental and theoretical works that have been done on this kind of sample. The main concern of this process was to ensure that the forces used to trap the sample might not cause "opticution", the term referred to cell damage by interaction with high flux of laser beam. This kind of

interaction leads to two major consequences that can cause harms in biological samples especially living cells. First, it will break the covalent bond between biological molecules and second, it will cause excessive heating associated with optical absorption of the samples. Researchers from all over the world continued to put some efforts on this subject and carried out numbers of experiments regarding to this technique. Finally, after years of invention, trapping of biological sample has been performed for the first time in 1987s. They have experimentally reported process of trapping and manipulation of viruses and bacteria by using optical tweezers (Dai et al. 1998). During experiments, single tobacco mosaic virus and *Escherichia coli* (*E. coli*) bacteria were trapped in aqueous chamber filled with water. Observation shows that both samples were successfully confined in the optical trap over period of time with no apparent physical damage detected on the sample. Since this remarkable initiation of optical tweezers in biophysical technique, it has opened up a major breakthrough in the new field which is known as single-molecular research.

Optical tweezers advancing to another level when Svoboda et al. demonstrated an experiment on trapping of metallic particles in 1994. This experiment was unique because they managed to prove that metallic particle was possible to be trapped by using optical tweezers technique. Before this significant finding, metallic object was viewed as poor candidates in optical trapping process due to its relatively large absorption and scattering forces. Magnitudes of these forces are directly proportional to the intensity of light and tend to destabilize the trap. However, in their experiment, they have clearly shown that gold nanoparticles with 36 nm in diameter are trapped with relatively 7 times more stable compared to non-metallic sphere of the same size. This surprising outcome was observed and analyzed. They found out that metallic samples possess a large polarizability, thus producing high magnitude of gradient forces to counterbalance the scattering forces components. This process allows metallic samples to be trapped stable in optical tweezers.

This technique continues to develop as it found its crucial applications in trapping and manipulating neutral particles. In 1997, Ashkin managed to design a new experimental method/set-up by using single laser beam that immediately provides a unique means to precisely control the dynamics of micro-size neutral particles. This achievement plays an important role in the revolutionary of physical and biological sciences. In addition, this research work leads to demonstration of cooling of a neutral atom in context of atomic physics (Ashkin 1997).

In early 2000, a great research work on three dimensional particle tracking for optical tweezers techniques has been carried out. This work successfully provided an insight on high-resolution position sensor for optical trapping process. In this work, lateral displacement and axial position of the trapped sphere are measured by estimating the ratio between the intensity of scattered light towards the total amount of light collected at the detector which is located at the back-focal plane of the microscope. A fluorescent latex bead with radius approximately 300 nm is used as the sample during process of trapping by Nd:YVO_4 laser with wavelength at 1.064 nm and 50 mW input power. An inverted microscope with numerical aperture $NA = 1.3$ is implemented in this experiment. This model was successfully used to

explain and describe the results obtained from Rayleigh-trapping experiments. Axial displacement of the trapped particle within the Rayleigh length which is calculated to be at $z = 150$ nm can be measured with percentage of precision less than 10 %. This work is considerably important as it provides a better means/manner to study the dynamics of single membrane molecules.

Advent in nano-manipulation technique manages to extend the use of optical tweezers down to nanometre scale. Frontier research works dealing with nanometre-sized biomolecule has been carried out in 2001 (Agrawal 2001). In this experiment, stiffness of a single actin filament is measured. Beads held by optical trap are attached to both ends of the actin filament. The sample is stretched and the relative displacement between the beads is measured. It is reported that the average displacement of 15–20 nm is recorded corresponding to the stiffness of 65 pNnm^{-1}. Basically, this research is considered as one of the pioneer work that operates by combining single molecule imaging with optical manipulation technique for the study of nanometre-scaled molecular motor. Moreover, the unitary processes of mechanical work and energy conversion have been successfully monitored by using this technique. This crucial development has given the opportunity for the other researchers to prolong their experimental research at the single molecular level.

In the following year, Dholakia et al. have reported the use of optical fields to arrange, guide or deflect particles in desired optical lattice geometries. Dholakia in his work entitled "Microfluidic Sorting in an Optical Lattice" managed to perform an optical sorter for micron-size particles that exploit the interaction of particles with dynamically reconfigurable 3-dimensional optical lattice. Sorting process categorized into two types which are sorted by size or refractive index. Efficiency of this sorting process has been calculated in the range of 96–100 %.

Optical trapping, manipulation and sorting techniques have been further improved by upgrading conventional optical trapping system implementing the use of diode laser bars. A single diode laser bar with dimension 100 μm × 1 μm operates at center wavelength of 980 nm and input power of 3 W is multiplexed by ten identical 0.25 NA objective lens along the entire width. This technique maneuvers vast arrays of independently controlled trapping channels which enables trapping of many particles simultaneously. It is reported that 1.8 μm polystyrene beads are trapped along the trapping zone which can be controlled in the range of 1–100 μm without any detectable damage on the sample. This technique directly enhanced the scaling limitation faced by previous laser traps.

The drive toward more sensitive nanoscale-manipulation of optical tweezers led to the development of optical trapping tools that capable to resolve the motion of biological system down to sub-nanometre level. In 2006, spatial resolution of optical tweezers has been successfully improved by using dual traps technique. This approach requires the subject to be held at both ends by using two different optical traps. A single 1.7 μm DNA is tethered between two equal size 860 nm polystyrene microspheres held in optical trap with stiffness of 0.13 pNnm^{-1}. Relative distance between polystyrene pair is recorded at the smallest spatial resolution of 2.3 Å (Chen 2006). This work allows the optical-trapping related studies to go beyond sub-nanometer scale with more promising results.

Through all those years, this technique was not only studied experimentally. Some researchers have comes out with modeling investigation on optical tweezers. For instance, Zakharian et al. in 2006 has developed numerical solutions for single-beam trapping of micro-beads in polarized light. In this work, electromagnetic fields distribution including the forces components acting around the spherical geometry of the trapped particle are successfully computed and modelled by using numerical solution of Lorentz law of forces. This model can be used to precisely calculate the stiffness of optical tweezers acting on a particle whether it is immersed in water or suspended in air.

In the following year, computational modelling on optical forces components and its torques has been successfully developed. In detail, a computational toolbox in a proper computer interface system is created to ease the optical tweezers modelling process. The model can be used to trap both spherical or non-spherical samples by using either Gaussian or any other types of trapping beam. For instance, simulation results of optical forces components plotted against relative displacement of the particles from equilibrium point has been demonstrated for the case of Gaussian and Laguerre-Gauss as the trapping beam. These kinds of modelling activity are very important in obtaining quantitative results, thus directly provides a bridge to link between theoretical work and experimental outcomes.

Within the past few years, scope of studies for this particular field is still growing positively either in theoretical and experimental parts. Different techniques and trapping apparatus for optical tweezers generation have been developed starting from a single lens system to a huge and complicated instrument consisting of multiple optical devices. This field evolves when the old lens-based optical tweezers techniques have been substituted by an all-fibre optical tweezers technique. Unlike the conventional tweezers system, this novel approach relies on the unique total internal reflection phenomenon that occurs within the circular core of fibre optics waveguide. This technique requires single-mode fibre probe with tapered hallow tip to produce an intense annular trapping beam as the output. Realization of this technique will greatly improve the design and instrumental part of optical tweezers technique with various potential applications in communication and biology.

However, a single optical fibre device can't form a stable 3-dimensional optical trap because of the weak intensity possessed by the trapping beam. This problem originates from the weak focusing ability possessed by the tapered fibre end which directly induced weak gradient force component that tends to destabilize the trap. This problem has been overcome by the usage of a single fibre probe with an annular light distribution. For this purpose, a tapered, chemically etched and hallow tipped metalized fibre probe are designed to produce the annular light beam. A solid glass bead with diameter of 2 μm surrounded in water has been successfully trapped by an annular light of 1.9 μm diameter produced from a single fibre probe with 20 μm tip. Laser source with input power of 10 mW and centered at $\lambda = 1.32$ μm is used. Scattering force component is recorded at roughly 6×10^{-12} N and the trapped bead is observed moving at the speed of 20 μm s^{-1}. Trapping by this technique can be explained by the balancing condition achieved between the electrostatic force which tends to attract the particle towards the fibre tips and the

scattering force component which push the particle in opposite direction. In the following years, a group of scientist from Fukuyama University led by Ikeda reported an interesting phenomenon of optical rotation on a micro-sized plastic bar by using a single-beam optical fibre tweezers system. Such object was observed rotated 360° in 4.8 s by using 20 mW output powers. In addition, they have successfully demonstrated clockwise and anti-clockwise rotation on a bar and cross-shaped plastic micron-size samples. During experiments, manipulation on the sample has been done by tuning the power of the output beam produced by all three tapered optical fibres. This technique is used to precisely control the rotational direction of any trapped particles.

A novel method of optical trapping by using only a single tapered fibre optics probe has been demonstrated in 2006. This unique fibre probe is originally made from a single-mode fibre with core diameter of 9 μm. Fabrication process including heating and drawing techniques are undergone by the waveguide in order to produce a parabola-like profile fibre tip. In this work, trapping of a yeast cell with diameter 6.5 μm immersed in water is performed at the room temperature. Maximum output power supplied by the laser source is 120 mW centered at $\lambda = 980$ nm. Trapping process takes place at the focal plane where the intensity of the laser beam emerged from the fibre tip is highest. This point is located at 1 μm from the fibre tip. Optical field distribution ejected from particular fibre tip is calculated and modelled. Both gradient and scattering forces components are simulated by FDTD method. Result shows that a stable three dimensional trap is plausible for this technique. This breakthrough is important as it makes optical tweezers technique become more convenient in dealing with micron-size particles.

Performance of the single-fibre optical tweezers is examined by Minzioni et al. in one of his paper published in 2008 (Minzioni et al. 2008). In this study, a comparison between all-fibre optical tweezers with conventional tweezers (single beam trap) has been made. Detail numerical computations are performed in Mie regime and performances of both tweezers are compared. A single-mode optical fibre probe with core diameter of 6.5 μm is fabricated. Yb-doped fibre laser at center wavelength of 1,070 nm is launched into the fibre probe with input power of 7 mW.

In the other case, a tightly focused Gaussian beam with the same input power and centered at 1,070 nm corresponding to numerical aperture of 1.25 is considered. Trapping of 5 μm polystyrene sphere immersed in water is performed by both systems and the minimum energy required to escape the traps ε_{esc} are calculated. Result suggests that single-fibre optical tweezers performance is relatively comparable to that obtained by a standard optical trap generated by a strongly focused Gaussian beam as shown in Fig. 2.1. Thus, both systems can be used to deal with micro-scale particle during optical manipulation process.

Recently, Yupapin and Jalil et al. have shown a new methodology to generates optical tweezers by using optical soliton pulse propagates within microring resonator system for several applications such as drug delivery, Alzheimer diagnostic, and blood cleaning (Aziz et al. 2012). Adoption of optical tweezers in microring resonator concept shows that there are still plenty of research and works that can be performed with rising number of new applications in various areas of studies.

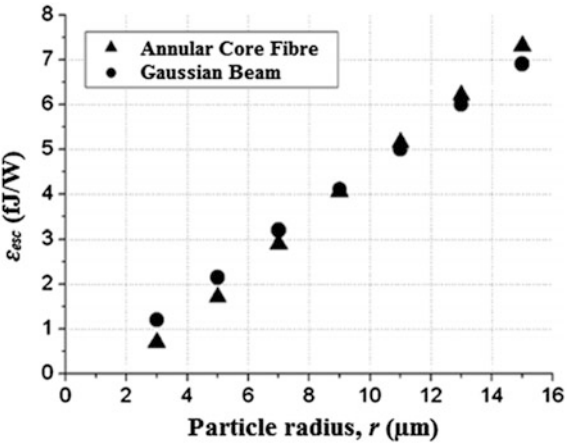

Fig. 2.1 Minimum energy for particle to escape the trap, ε_{esc} plotted against particle radius, r for single fibre optical tweezers and strongly focused Gaussian beam

2.5 Temporal Solitons

In the context of nonlinear optics, soliton can be classified as being temporal or spatial solitons (Wen et al. 2010), depending whether the confinement of light occurs in time or space during the wave propagation. Both types of solitons (temporal or spatial) evolve from a nonlinear change in refractive index of an optical material induced by the light intensity known as the optical Kerr effect (Ishii et al. 2001). The bright and dark spatial solitons form only when the nonlinear effects balanced the diffractive effect precisely. The spatial soliton can form in a self-defocusing nonlinear medium.

The existence of temporal soliton in optical fibre was discovered in 1973 and experimentally proved by the year of 1980 (Agrawal 2001). A balance between the group-velocity dispersion (GVD) and self-phase modulation (SPM) induced by the Kerr nonlinearity caused the formation of temporal soliton inside the optical fibre (Tian and Gao 2005). Temporal soliton represents the optical pulse that maintains its shape, while the spatial soliton is the self-guided beams that remains confined in the transverse direction orthogonal to the direction of propagation. The major nonlinear effects that are responsible for the formation of optical solitons are the spatial self-focusing or self-defocusing and the temporal self-phase modulation (SPM).

Temporal soliton defined as a pulse or wave packet that maintains its shape when propagate at constant speed without any distortion due to dispersion (Yupapin and Suchat 2007). The dispersion effect originates from the dependency of phase velocity towards its frequency and any medium that exhibits such properties is called dispersive media. Every wave packets built from a plane waves with several different frequencies. Due to the dispersive effect, all of these waves travel at different velocities, thus changing the pulse shape over the time. This effect is presented by group delay dispersion parameter, D. D is described as:

$$\Delta\tau \approx DL\Delta\lambda \tag{2.4}$$

where $\Delta\lambda$ is the bandwidth of the pulse in terms of wavelength.

The envelope of optical pulse widens for $\Delta\tau$ after travelling at distance L. On the other hand, the nonlinear Kerr effect induced variation in refractive index. This process directly modified the phase shift in the pulse that leads to a change in frequency spectrum of the pulse. This whole process is referred to SPM.

By considering that a Gaussian beam with intensity I depend on time t, hence:

$$I(t) = I_o \exp\left(\frac{-t^2}{\tau^2}\right) \tag{2.5}$$

where I_o is the peak intensity and τ is the pulse duration of the wave.

Optical Kerr effect produces variation in refractive index of $n(I) = n_o + n_2 I$. As the propagation continues, the intensity at any point of media is changed.

This process yields a time-varying refractive index as:

$$\frac{dn(I)}{dt} = \frac{-2t}{\tau^2} n_2 I_o \exp\left(\frac{-t^2}{\tau}\right) \tag{2.6}$$

The variation of refractive index values is responsible for instantaneous phase shift of the pulse, ϕ. ϕ is given by:

$$\phi(t) = \omega_o t - kx \tag{2.7}$$

$$\phi(t) = \omega_o t - \frac{2\pi}{\lambda_o} L \cdot n(I) \tag{2.8}$$

where ω_o and λ_o represents the frequency and wavelength of the pulse respectively, and L is the propagation distance.

These phase shifts induce the changes in frequency of the pulse and given by:

$$\omega(t) = \frac{d\phi(t)}{dt} \tag{2.9}$$

$$\omega(t) = \omega_o - \frac{(2\pi L)}{\lambda_o} \frac{dn(I)}{dt} \tag{2.10}$$

$$\omega(t) = \omega_o + \frac{4\pi L n_2 I_o}{\lambda_o \tau^2} \cdot t \cdot \exp\left(\frac{-t^2}{\tau}\right) \tag{2.11}$$

Equation (2.11) can be substituted by $\omega(t) = \omega_o + \alpha t$. The second term of the right hand side of this equation clearly states that there is an extra frequency component generated as it propagates in a medium.

This SPM effect broadens the frequency spectrum of the pulse and leading edge is said to be compressed and having a positive chirp. Such optical pulse is stable and propagates undistorted in the form of temporal soliton.

2.6 Microring Resonator System

Marcatili were first demonstrated the concept of light transmission in curved optical dielectric waveguide in 1969. From the experiments done by this group of researchers, different cross sectional diameters of the dielectric waveguides were examined. The bent of light wave within the guided waveguide materials was successfully proved. These findings had been the pioneer work for the development of the studies in the field of guided-wave optics from all over the world.

Weber and Ulrich (1971) reported the characteristics and operational of circulated laser, formed by a circular single mode light-guiding thin film. This system was initially known as ring resonator. This system consisted of a cylindrical glass rod with 5 mm diameter coated with Rhodamine 6G doped with polyurethane film ($n = 1.55$). The operational of laser pulse from the ring resonator device was successfully developed by this group (Ulrich and Weber 1972).

Haaristo and Pajer proposed and demonstrated the integration of ring waveguide and two tangential straight-channel waveguides on both sides of the ring in 1980 (Moffitt et al. 2006). Both two waveguides were geometrically and intentionally coupled. These straight bus waveguides were made of polymethyl methacrylate (PMMA) doped film on quartz substrate. The most interesting part about this work was that the device has a very small value of coupling loss (about 0.05 dBm/cm). The special properties of low loss and its polarization maintenance were the main reasons why this device was suitable enough for fibre optics interferometers.

In 1982, Stoke et al. successfully demonstrated the optical glass fibre ring resonator (Minzioni et al. 2008). This device consisted of a single-mode fibre and a dielectric coupler. This device was designed to operate at $A = 632.5$ nm. The work initiated numerous researchers on glass-based integrated ring resonator.

In early 1990s, a group of researchers have successfully demonstrated the construction of microring resonator from semiconductor based materials (Chu et al. 1993). Through this research, the researchers came out with optical pumped microdisk in both GaInAsP/InP and III-Nitrides materials with smallest disk circumference recorded at 15 μm (Dai et al. 1998). However, one of the weaknesses at this time was, the resonator designed without bus waveguide coupled to the ring geometry. In this configuration, the transmission of light from the resonator relied on the fibre. This draw back has been overcome by Rafizadeh (1997) with the fabrication of integrated microring resonator system where two lateral bus waveguides coupled on the circumference of the ring.

Several configuration of the ring resonator systems have been proposed based on GaAs/AlGaAs materials (Absil 2000). A racetrack-shaped ring resonator has been designed to enhance the coupling efficiency at the coupler region with cross

sectional area of 0.5 μm^2 and 400 μm bus waveguide length. The device can perform a wavelength conversion process with 14 % conversion efficiency, quite high percentage compared with other configuration systems. Such results were achieved by using relatively low input power of about 10 mW (Absil et al. 2000) and due to the low-loss and high nonlinear properties possessed by the particular device.

Rabus and Hamacher (2001) demonstrated various ring resonator configurations based on the GaAs/AlGaAs medium. The development of this research area led to a novel integration of a single resonator device made up of GaInAsP/InP material. By using suitable wavelength values, the value of free spectral range (FSR) of 50 GHz with the full width at half maximum (FWHM) of 24 pm were achieved. With integration of semiconductor optical amplifier (SOA), the quality factor, Q up to 65,000 was induced (Rabus et al. 2002a).

A desire output ring resonator transmission can be realized by using multiple-coupled ring resonator system. A new concept of lateral coupling between the ring and bus waveguide has been introduced into different loss-compensated ring resonator configurations to modify the output filter functions. For instance, single, double, and triple multistage optical filter devices were designed. It was reported that such configuration results of FSR with 12.5, 25.0, and 50.0 GHz respectively and on-off ratios greater than 20 dB (Rabus et al. 2002b).

Until this date, record shows that there is no active type ring resonator device that has been fabricated. The first active ring resonator device was constructed from all-active materials. This device was capable to alter the filtering performance. An active ring resonator device was fabricated from indium phosphate material. Such systems showed a relatively high FSR of 10.5 nm with Q of 5,700. Under resonance state, this device was operated at the center wavelength, $\lambda = 1.584$ μm and resulting the output signal transmission, T of 0.1 with finesse, $F = 40$ (Djordjev et al. 2002a). The models of ring resonator which vertically coupled to the bus waveguide have been used with small radius, up to 10 μm (Djordjev et al. 2002b). This successful work becomes a reference for numerous researchers and academicians in this field. In last few decades, this field have rapidly grown and realized in electro-optic polymer, silicon nitride, and silicon oxynitride based materials (Rabiei and Steier 2003; Tan 2004; Geuzebroek 2005).

A complete analysis expression describing the propagation within nonlinear dispersive microring resonator systems has been obtained using matrix approaches. The transfer matrix method can describe precisely a complicated system, such as multiple numbers of coupled ring resonator and others. This method can implement to any structures or geometries of microring resonators. It is also valid for any values of coupling parameters (Poon et al. 2004).

The theoretical analysis on optical microring becomes very important indeed. Details in calculation of loss element in ring resonator device are carried out successfully. The perturbation approach may compute the scattering and radiation losses of components for microring resonator with cylindrical waveguide. The losses in the system which is originated from the shape defect on the ring waveguide and the fluctuation of core refraction index are successfully discussed

(Rabiei 2005). Such analysis provides an insight for a better understanding on microring resonator as discrete loss component impose a serious limitation during fabrication process.

Mahdi (2013) proposed the analytical vernier effect for nanophotonics circuits by using ring resonator systems. It is shown a big contribution about the mathematical calculation especially in physics fields. Amiri (2013) proposed an idea of optical soliton based on communication technology by using microring resonator systems. He has shown that the integrated dark soliton is a useful concept for the communication technology. The dark-bright solitons conversions within add-drop system have been done by Muhammad Arif in 2013. He has shown that the dark-bright solitons can be converted in ring resonator within add-drop system. The research is focussed on the nanotechnology and biomedicine based studies. Muhammad Safwan (2013) proposed the tenability of the optical solitons in micro- and nanoring resonator systems. The electrooptics tenability of the optical solitons interaction within PANDA and double-PANDA system has been investigated.

Due to its potential applications, in the recent years, microring resonator becomes a rapidly developing research interest, especially in photonics devices. Recently, Jalil and Yupapin (2008, 2009, 2011, 2012) have reported a novel idea of PANDA ring resonator configurations which utilized in various applications, especially in communication and medical applications. The development on design and fabrication of microring resonator has been a subject of intense studies among researchers.

Chapter 3
Theory

3.1 Introduction

The fundamental principles of the ring resonators, including single ring resonator and the add-drop configuration systems are discussed in this chapter. Nonlinear response of the temporal solitons from nonlinear Kerr effect in optical fibre and the basic principles of self-phase modulation (SPM), signal flow graph (SFG) theory, and Z-transform method are explained accordingly.

3.2 Ring Resonator System

The first study on integrated ring resonator for a bandpass filter in microwave has been published by E.A. Marcatili in 1961 (Absil et al. 2000). The proposed layout of the channel dropping filter is as shown in Fig. 3.1. The transmission properties of the guide consist of a dielectric rod with a rectangular cross section, surrounded by several dielectrics of small refractive indices (Marcatili 1969).

Purely passive single ring resonator filter as shown in Fig. 3.1 have been realized materials of AlGaAs-GaAs (Hagness et al. 1997), Si-SiO_2 (Little et al. 1997), and Si_3N_4-SiO_2 (Parkin et al. 2006). In the form of racetrack, GaInAsP (Vanderhaegen et al. 1999) and AlGaAs-GaAs (Chin et al. 1999) material systems have been realized for passive ring resonator. The general architecture for an autoregressive planar waveguide optical filter was firstly demonstrated in 1996 by Madsen and Zhao (1996). The autoregressive lattice filters were designed and fabricated using Germanium-doped silica waveguide.

S. Daud et al., *Simulation of Optical Soliton Control in Micro- and Nanoring Resonator Systems*, SpringerBriefs in Physics, DOI 10.1007/978-3-319-15485-5_3

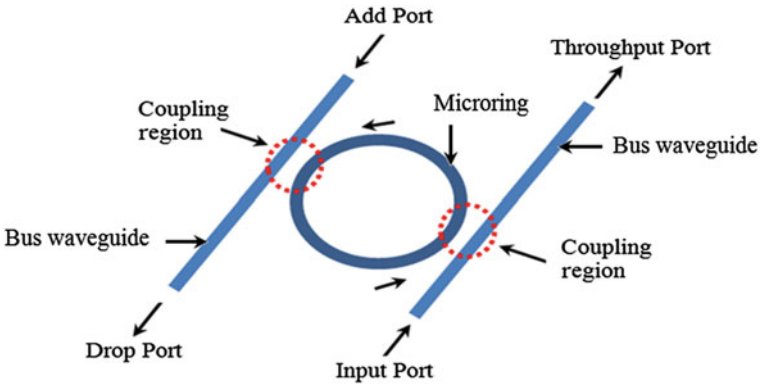

Fig. 3.1 Ring resonator channel dropping filter

3.2.1 Single Ring Resonator

Based on Yariv (2002), the basic ring resonator consists of unidirectional coupling between a ring resonator and a waveguide as shown in Fig. 3.2. E_{i1} and E_{t1} are the input and output port respectively, κ and t are the coupling coefficients of the coupler, κ^* and t^* are its conjugates respectively, and α is the loss coefficient of the ring.

When an input electric field, E_{i1} is coupled into the ring waveguide, positive feedback mechanism is induced and the field inside the ring resonator, E_{i2} starts to build-up. In such configuration, only certain wavelengths are allowed to resonate inside the ring waveguide. Only the waves that have the same wavelength with the waveguide are allowed to resonate within the waveguide while the rest will be reflected. Thus, the selective frequency is obtained (Yariv 2002; Rabus 2010).

The various kinds of losses occur along the propagation of light in the ring resonator filter. That interaction can be described by the matrix relation:

$$\begin{pmatrix} E_{t1} \\ E_{t2} \end{pmatrix} = \begin{pmatrix} t & \kappa \\ -\kappa^* & t^* \end{pmatrix} \begin{pmatrix} E_{i1} \\ E_{i2} \end{pmatrix} \tag{3.1}$$

The complex mode amplitudes, E are normalized so that their square magnitude corresponds to the modal power. The coupler parameters, κ and t depend on the specific coupling mechanism used while the * denotes the conjugated complex values of κ and t respectively.

It is considered that the networks are reciprocal. Thus, the matrix is symmetric (Yariv 2000). Therefore:

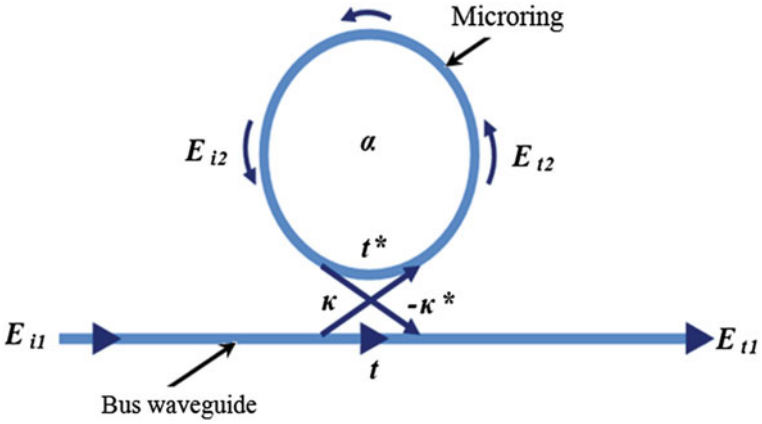

Fig. 3.2 Schematic diagram of single ring resonator waveguide

$$\left|\kappa^2\right| + \left|t^2\right| = 1 \tag{3.2}$$

and

$$E_{i1} = 1 \tag{3.3}$$

Then, the roundtrip of the ring is given by:

$$E_{i2} = \alpha \cdot e^{j\theta} E_{t2} \tag{3.4}$$

where α is the loss coefficient of the ring (zero loss: $\alpha = 1$), $\theta = \omega L/c$, $L = 2\pi r$ is the circumference of the ring, r is the radius of the ring, $c = c_o/n_{eff}$ is the phase velocity of the ring mode, $\omega = kc_o$ is the angular frequency, c_o is the speed of light in vacuum, and $k = 2\pi/\lambda$.

By using the vacuum wavenumber, the effective refractive index, n_{eff} can be introduced into the ring coupling relations by:

$$\beta = k \cdot n_{eff} = \frac{2\pi \cdot n_{eff}}{\lambda} \tag{3.5}$$

where β is the propagation constant.
As discussed earlier, $\theta = \frac{\omega L}{c}$, $c = \frac{c_o}{n_{eff}}$, $k = \frac{2\pi}{\lambda}$.
Simplified,

$$\theta = \frac{\omega L}{c}$$

$$\theta = 4\pi^2 n_{eff} \frac{r}{\lambda} \tag{3.6}$$

Thus the transmission power, P_{t1} in the output waveguide is given as (Timotijevic et al. 2006):

$$P_{t1} = |E_{t1}|^2 = \frac{\alpha^2 + |t|^2 - 2\alpha|t|\cos(\theta + \varphi_t)}{1 + \alpha^2|t|^2 - 2\alpha|t|\cos(\theta + \varphi_t)} \tag{3.7}$$

where $t = |t|\exp(j\varphi_t)$. $|t|$ are the coupling losses and φ_t is the phase of the coupler. The circulating power, P_{i2} in the ring then is given as:

$$P_{i2} = |E_{i2}|^2 = \frac{\alpha^2\left(1 - |t|^2\right)}{1 + \alpha^2|t|^2 - 2\alpha|t|\cos(\theta + \varphi_t)} \tag{3.8}$$

In case of resonance, $(\theta + \varphi_t) = 2\pi m$, where m is an integer. Thus, P_{t1} and P_{i2} are obtained as:

$$P_{t1} = |E_{t1}|^2 = \frac{(\alpha - |t|)^2}{(1 - \alpha|t|)^2} \tag{3.9}$$

and

$$P_{i2} = |E_{i2}|^2 = \frac{\alpha^2\left(1 - |t|^2\right)}{(1 - \alpha|t|)^2} \tag{3.10}$$

Once the internal losses are equal to the coupling losses, a special case will happen, where $\alpha = |t|$ in (3.9). Then, the transmitted power becomes zero. This is due to the destructive interface, which is known as critical coupling. By using the above equations, it is possible to get a good idea of the behaviour of a simplified basic ring resonator filter configuration consisting of only one waveguide and one ring.

3.2.2 Add-Drop Configuration

The basic ring resonator for add-drop configuration system is shown in Fig. 3.3. Add-drop configuration system consists of two bus waveguides and the ring resonator itself. The four ports of the ring resonator are referred as input port, add port, throughput port, and drop port depicted as E_{in}, E_{add}, E_t, and E_d respectively.

For simplification, input port, E_{in} is defined to be equal to 1, $E_{in} = 1$. The throughput mode amplitude in the first waveguide is given as (Heebner et al. 2008):

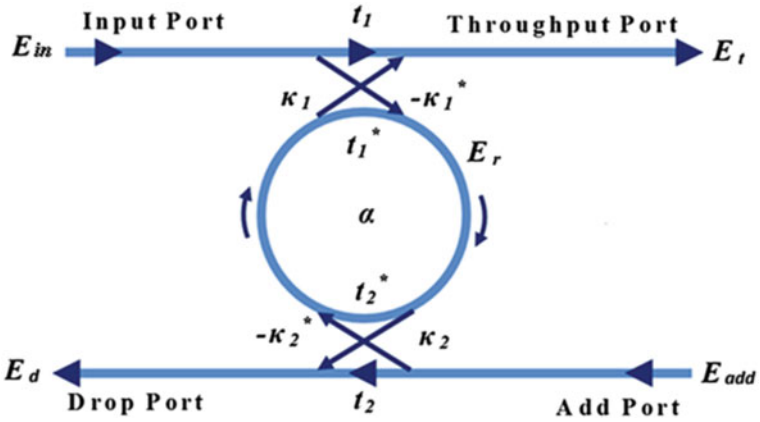

Fig. 3.3 Schematic diagram of add-drop configuration system

$$E_t = t_1 + \frac{-\kappa_1 \kappa_1^* t_2^* \alpha_{1/2}^2 e^{j\theta|t_1|^2+|\kappa_1|^2}}{1 - t_1^* t_2^* \alpha_{1/2}^2 e^{j\theta}}$$

$$E_t = \frac{t_1 - t_2^* \alpha_{1/2}^2 e^{j\theta}}{1 - t_1^* t_2^* \alpha_{1/2}^2 e^{j\theta}}$$

$$E_t = \frac{t_1 - t_2^* \alpha e^{j\theta}}{1 - t_1^* t_2^* \alpha e^{j\theta}} \tag{3.11}$$

where $\alpha = \alpha_{1/2}^2$ and $\theta = 2\theta_{1/2}$.

Now, the mode amplitude in the ring pass the second coupler. The dropped mode amplitude in the waveguide is given as (Heebner et al. 2008):

$$E_d = \frac{-\kappa_1^* \kappa_2 \alpha_{1/2} e^{j\theta_{1/2}}}{1 - t_1^* t_2^* \alpha e^{j\theta}} \tag{3.12}$$

At resonance, the output power from the drop port is given as (Heebner et al. 2008):

$$P_{d-Resonance} = |E_{d-Resonance}|^2$$

$$P_{d-Resonance} = \frac{\left(1 - |t_1|^2\right) \cdot \left(1 - |t_2|^2\right) \cdot \alpha}{(1 - \alpha|t_1 t_2|)^2} \tag{3.13}$$

At resonance, the throughput port mode amplitude, E_t becomes zero. For identical symmetrical coupler, $t_1 = t_2$ if $\alpha = 1$, which indicates that the wavelength on resonance is fully extracted by the resonator.

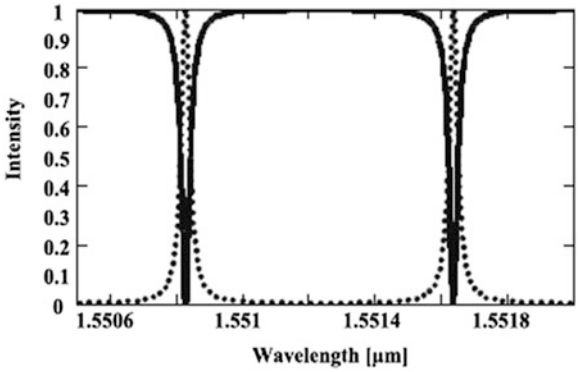

Fig. 3.4 Add-drop ring resonator filter characteristics

Hence,

$$\alpha = \left|\frac{t_1}{t_2}\right| \tag{3.14}$$

If the ring resonator is lossless ($\alpha = 1$), then the coupler have to be symmetric in order to achieve the minimum intensity. The transmission of a lossless ring resonator add-drop filter with radius, R = 148 μm is as shown in Fig. 3.4.

3.3 Fibre Nonlinearity

Optical fibre is a media which response nonlinearly when high intensity light passing through it (Singh and Singh 2007). Nonlinear effects in optical fibre are mainly contributed from nonlinear refraction caused by the third-harmonic generation and four-waves mixing are not efficient in optical fibre. This phenomenon refers to the intensity dependence of optical fibre medium on the refractive index.

Nonlinear medium is a medium in which the dielectric polarization, P response nonlinearly to the intense electromagnetic fields. The behaviour of light in nonlinear medium can be described by using the theory of nonlinear optics. In the fundamental level, the origin of nonlinear response is related to a harmonic motion of bound electrons under the influence of an applied field (Ashkin and Dziedzic 1987; Calander and Willander 2002; Chen 2006).

The total electric polarization induced is related to electric field, E and is given as (Bonessi et al. 2007):

$$P = \varepsilon_o\left(\chi^{(1)} : E + \chi^{(2)} : EE + \chi^{(3)} : EEE + \cdots\right) \tag{3.15}$$

where ε_o is the vacuum permittivity and $\chi^{(n)}$ is the nth order component of the electric susceptibility of the medium.

The linear susceptibility, $\chi^{(1)}$ represents the dominant contribution towards P. For linear medium, the polarization of the medium varies linearly with E and in this case only first term of this equation is considered (Dienerowitz et al. 2008). The second-order susceptibility, $\chi^{(2)}$ responsible for nonlinear effects such as sum frequency generation (SFG) and second harmonic generation (SHG). $\chi^{(2)}$ is a scalar quantity. In reality, $\chi^{(2)}$ is a tensor which depends on the combination of more than one frequencies. SFG process occurs when two input photons at angular frequencies ω_1 and ω_2 annihilate and one photon with frequency ω_3 is generated simultaneously during the parametric process. SHG can be considered as a special case of SFG (Harada and Asakura 1996; Liu and Zhao 2012).

The input photons must have the same angular frequencies. Hence, $\omega_1 = \omega_2 = \frac{1}{2}\omega_3$. During this process, the photons are effectively combined to form the new photons with twice energy and frequency, and half wavelength of the input photons. The lowest order nonlinear effects originate from the third-order susceptibility, $\chi^{(3)}$. It is also known as higher-order frequency mixing, which is responsible for the phenomenon such as third-harmonic generation, four-waves mixing, and nonlinear refraction (Stilgoe et al. 2008).

Assume that the nonlinearity of the fibre ring is the Kerr type effect (Ke and Gu 1999). When light propagates within nonlinear materials or mediums, there is a change in the refractive index of the medium in response to an applied electric field. The refractive index of the medium, n is given as:

$$n = n_o + n_o I = n_o + \frac{n_2}{A_{eff}} P \tag{3.16}$$

where n_o is the linear refractive index, n_2 is the nonlinear refractive index, I is the optical intensity, P is the optical power, and A_{eff} is the effective mode core area of the device (Fazal and Block 2011; Neuman and Block 2011).

This phenomenon leads to a number of interesting nonlinear effects such as cross-phase modulation (XPM) and self-phase modulation (SPM). XPM occurs when an optical field induced a nonlinear phase shift on another field that having a different wavelength. When two optical fields with different frequencies, ω_1 and ω_2 propagate simultaneously inside a fibre, the total electric field, E is given as (Van Mameren et al. 2011):

$$E = \frac{1}{2}\widehat{X}\left[E_1 \exp -i(\omega_1 t) + E_2 \exp -i(\omega_2 t)\right] \tag{3.17}$$

In the other case, an optical field propagates inside the optical fibre can experienced self-induced phase shift. This phenomenon is known as SPM.
The change in phase of the optical field is given as:

$$\varphi = \tilde{n}k_o L = \left(n + n_2|E|^2\right)k_o L \tag{3.18}$$

where $k_o = \frac{2\pi}{\lambda}$ and L is the length of the fibre. Spectral broadening of pulses and formation of optical solitons are due to SPM phenomenon (Qiu and Xu 2011).

3.4 Nonlinear Kerr Effect

Solitons induce enharmonic motion between bound electrons in the medium. These electrons emit secondary wave which is directly proportional to the induced polarization. Due to this phenomenon, the optical field has extra phase retardation. The whole process can be manifested as intensity-dependent change in refractive index of the medium. This process is called as optical Kerr effect (Butcher and Cotter 1990).

Hahn (2006) in his book entitles Light Scattering Theory states that the Kerr effect was firstly discovered by a Scottish physicist, John Kerr in 1875. Kerr effect is a change in refractive index, n of a material in response to applied electric fields (Melnichuk and Wood 2010). The induced refractive index change is directly proportional to the square of the electric field. Thus, the optical Kerr effect is the variation in refractive index which is proportional to the local irradiance of the light passing through the media. This unique phenomenon leads to numbers of interesting nonlinear effect such as self-phase modulation (SPM) and cross-phase modulation (XPM).

Intense light beam can provide the modulation electric field in the isotropic Kerr medium. The polarization vector, P in the direction of electric field, E is given as:

$$E = E_o \cos(\omega t + kz) \tag{3.19}$$

where E_o is the amplitude, ω is the frequency, and k is the wavenumber. The dielectric polarization, P is given as:

$$\begin{aligned} P = {} & \varepsilon_o \chi^{(1)} E_o \cos(\omega t - kz) + \varepsilon_o \chi^{(2)} E_o^2 \cos^2(\omega t - kz) \\ & + \varepsilon_o \chi^{(3)} E_o^3 \cos^3(\omega t - kz) + \cdots \end{aligned} \tag{3.20}$$

By using double and triple-angle formulas from trigonometry relation,

$$\cos 2x = 2\cos^2 x - 1 \tag{3.21}$$

and

$$\cos 3x = 4\cos^3 x - 3\cos x \tag{3.22}$$

Equation (3.20) can be rewritten as:

$$P = \frac{1}{2}\varepsilon_o \chi^{(2)} E_o^2 + \varepsilon_o \chi^{(1)} E_o \cos(\omega - kz) + \frac{1}{2}\varepsilon_o \chi^{(2)} E_o^2 \cos 2(\omega t - kz) + \frac{3}{4}\varepsilon_o \chi^{(3)} E_o^3 \cos(\omega - kz) + \frac{1}{4}\varepsilon_o \chi^{(3)} E_o^3 \cos 3(\omega t - kz) + \cdots \tag{3.23}$$

The first term on the right side in (3.23) is a term that gives a dc field across the media. The second term is assigned as the fundamental harmonic of polarization, which shows that the component oscillates at frequency ω. The second harmonic polarization can be seen in the third term which represents the oscillation with double fundamental frequency, 2ω. The term with frequency 3ω is called the third harmonic of polarization.

In the field of optical fibre, the component $\chi^{(2)}$ vanished and (3.23) can be transformed into:

$$P = \varepsilon_o \chi^{(1)} E_o \cos(\omega t - kz) + \frac{3}{4}\varepsilon_o \chi^{(3)} E_o^3 \cos(\omega t - kz) + \frac{1}{4}\varepsilon_0 \chi^{(3)} E_o^3 \cos 3(\omega - kz) \tag{3.24}$$

Because of variation in indexes of the fibre, there is phase lack between frequency ω and 3ω. Due to this mismatch phase, the third term in (3.24) can be neglected.

Hence, the polarization can be rewritten as:

$$P = \varepsilon_o \chi^{(1)} E_o \cos(\omega t - kz) + \frac{3}{4}\varepsilon_o \chi^{(3)} E_o^3 \cos(\omega t - kz) \tag{3.25}$$

Equation (3.25) can be decomposed into two components, which are linear polarization, P_L and nonlinear polarization, P_{NL}. P_L and P_{NL} are given as:

$$P_L = \varepsilon_o \chi^{(1)} E(r,t) \tag{3.26}$$

and

$$P_{NL} = \varepsilon_o \varepsilon_{NL} E(r,t) = \frac{3}{4}\varepsilon_o \chi^{(3)} |E(r,t)|^3 \tag{3.27}$$

For the plane wave, the intensity, I is given as:

$$I = \frac{1}{2} c \varepsilon_o n_o E_o^2 \tag{3.28}$$

where c is the speed of light in vacuum.

By substituting (3.28) into (3.25), P can be rewritten as:

$$P = \varepsilon_o \chi^{(1)} E(r,t) + \frac{3}{2} \frac{\chi^{(3)}}{c\varepsilon_o n_o} IE(r,t) \tag{3.29}$$

χ_{eff} defines as the effective susceptibility of the medium. χ_{eff} is given as:

$$\chi_{eff} = \frac{P}{\varepsilon_o E} \tag{3.30}$$

Therefore,

$$\chi_{eff} = \chi^{(1)} + \frac{3}{2} \frac{\chi^{(3)}}{c\varepsilon_o n_o} I \tag{3.31}$$

The effective refractive index, n_{eff} is given as (Heebner et al. 2004):

$$n_{eff}^2 = 1 + \chi_{eff} \tag{3.32}$$

Thus,

$$n_{eff} = \left(1 + \chi_{eff}\right)^{1/2} \tag{3.33}$$

$$n_{eff} = \left[1 + \chi^{(1)} + \frac{3}{2} \frac{\chi^{(3)}}{c\varepsilon_o n_o^2} I\right]^{1/2} \tag{3.34}$$

By using Taylor's expansion series, (3.34) can be rewritten as:

$$n_{eff} = n_o + \frac{3}{4} \frac{\chi^{(3)}}{c\varepsilon_o n_o^2} I - \frac{3}{16} \frac{\chi^{(3)}}{c\varepsilon_o n_o^2} I + \cdots \tag{3.35}$$

As compared with the first term, the third term in (3.35) have a very small value and can be neglected. Thus,

$$n_{eff} = n_o + \frac{3}{4} \frac{\chi^{(3)}}{c\varepsilon_o n_o^2} I \tag{3.36}$$

From (3.16), the linear refractive index can be represented as:

$$n_o = \frac{3}{4} \frac{\chi^{(3)}}{c\varepsilon_o n_2^2} \tag{3.37}$$

where n_o is the linear refractive index and n_2 is the nonlinear refractive index of the media. Equation (3.37) describes accurately the nonlinear response for any Kerr medium.

The change in refractive index, Δn is proportional to the intensity of light or square of the steady electric field (Melnichuk and Wood 2010). This process is a self-induced effect in which the phase velocity of the wave depends on its intensity. Such process assigned as the nonlinear refraction within Kerr media.

3.5 Resonance Characteristics

Resonance describes as the tendency of a system to oscillate with greater amplitude with particular frequency (Yupapin and Pornsuwanchareon 2008). The resonance frequency is a natural frequency of variation, determined by the physical parameters of the vibrating object. It occurs when a system is able to store and easily transfer energy between two or more different storage modes. Resonance system can be used to generate vibration of a specific frequency. The performance of each resonator can be measured in terms of resonance width, free spectrum range, finesse, and quality factor.

3.5.1 Bandwidth

The bandwidth of the resonator is given by the full width at half maximum (FWHM) of the ring intensity resonance or its 3-dB bandwidth. It is a measure of the sharpness of the resonance. The resonance bandwidth determines how fast the optical data can be processed by a ring resonator.
The FWHM of the single ring resonator is given as (Saeung and Yupapin 2008):

$$\delta\phi = \frac{2 \cdot (1 - x \cdot y)}{\sqrt{x \cdot y}} \tag{3.38}$$

where x and y are the x-component and y-component of the selected point respectively.

To understand how the bandwidth of the resonator is affected by the coupling coefficient κ, a critically coupled ring resonator is considered as an example. In such a case, (3.38) can be simplified as:

$$\delta\phi = \frac{2 \cdot \kappa}{\sqrt{1 - \kappa}} \tag{3.39}$$

Therefore, it may conclude that the lower the coupling coefficient, κ the smaller the resonance bandwidth.

3.5.2 Finesse

The finesse, F of the resonator is defined as the ratio of the free spectral range (FSR) and the full width at half maximum (FWHM) of a resonance (Yupapin and Pornsuwanchareon 2008). By considering the FSR in terms of phase is equal to 2π, thus the finesse of the resonator is given as:

$$F = \frac{2\pi}{\delta\phi} = \frac{\pi \cdot \sqrt{x \cdot y}}{(1 - x \cdot y)} \tag{3.40}$$

Simply,

$$Finesse, F = \frac{FSR}{FWHM} \tag{3.41}$$

The finesse gives the resolving power of the resonator when it is used as a transmission filter. The resonator finesse is independent on its dimensions or circulating light wavelength. It is only a function of the coupling coefficient and the internal loss.
The finesse of a critical coupling ($x = y$) is given as:

$$F|_{x=y} = \frac{\pi \cdot y}{1 - y^2} = \frac{\pi \cdot \sqrt{1 - \kappa}}{\kappa} \tag{3.42}$$

$$F|_{x=y} = \frac{\pi \cdot x}{1 - x^2} = \frac{\pi \cdot D \exp^{-\alpha L/2}}{1 - D^2 \exp^{-\alpha L}} \tag{3.43}$$

Figure 3.5 shows the relationship between the finesse, F with the coupling coefficient, κ of the resonator. It is shown that the finesse, F exponentially decrease with the increase of the value of coupling coefficient, κ. From the graph, it can be concluded that the finesse, F depends on the coupling coefficient, κ at the point of maximum on-off ratio.

3.5.3 Free Spectral Range

The free spectral range (FSR) is the frequency spacing between two resonance peaks of a signal (Yupapin and Pornsuwancharoen 2008). For calculation, simply the phase constant which corresponds to $\phi = 2 \cdot m\pi$ is defined as k and the phase constant which corresponds to $\phi = 2 \cdot (m + 1) \cdot \pi$ is defined as $k + \Delta k$, where m is an integer and Δk is the phase constant.

The frequency shift, Δf and the wavelength shift, $\Delta\lambda$ are related to the variation of the phase constant, Δk as:

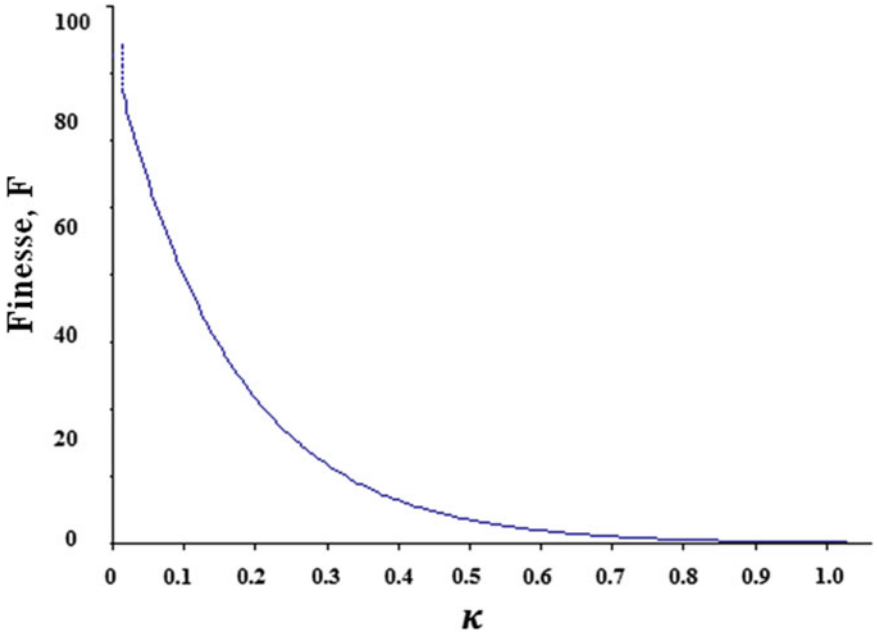

Fig. 3.5 Relationship between finesse, F with the coupling coefficient, κ at the point of maximum on-off ratio

$$\Delta f = \frac{c}{2\pi} \cdot \Delta k \tag{3.44}$$

and

$$\Delta \lambda = -\left(\frac{\lambda^2}{2\pi}\right) \cdot \Delta k \tag{3.45}$$

The resonance spacing in terms of frequency, f and wavelength, λ are given as:

$$\Delta f = \frac{c}{n_{gr} \cdot L} \tag{3.46}$$

and

$$\Delta \lambda = \left| -\frac{\lambda^2}{n_{gr} \cdot L} \right| \tag{3.47}$$

where n_{gr} is the group refraction index.

n_{gr} is defined as:

$$n_{gr} \equiv n_{eff} - \lambda \frac{dn_{eff}}{d\lambda} = \frac{\Delta k}{2\pi} \tag{3.48}$$

By using $\delta\phi = \delta(k_n \cdot L) = \frac{2\pi}{F}$ and the FWHM, $\delta\phi$ in terms of frequency, f and wavelength, λ at the resonance peaks are given as:

$$\delta f = \frac{c}{F \cdot n_{gr} \cdot L} \tag{3.49}$$

and

$$\delta\lambda = \frac{\lambda^2}{F \cdot n_{gr} \cdot L} \tag{3.50}$$

By using the FSR (Δf or $\Delta\lambda$) and the FWHM (δf or $\delta\lambda$), the finesse, F can also be calculated by using:

$$F = \frac{FSR}{FWHM} \tag{3.51}$$

In the frequency domain,

$$\frac{\Delta f}{\delta f} = \frac{\frac{c}{n_{gr}L}}{\frac{c}{F \cdot n_{gr} \cdot L}} = F \tag{3.52}$$

In the wavelength domain,

$$\frac{\Delta\lambda}{\delta\lambda} = \frac{\frac{\lambda^2}{n_{gr}L}}{\frac{\lambda^2}{F \cdot n_{gr} \cdot L}} = F \tag{3.53}$$

3.5.4 Quality Factor

The quality factor, Q or also known as the factor of resonator is a measure of the sharpness of the resonance (Yupapin and Pornsuwancharoen 2008). The Q factor of an optical waveguide is due to its energy stored and the power lost per optical cycle. Q factor is defined as:

$$Q = \omega \frac{Stored\ energy}{Power\ lost} \tag{3.54}$$

For the ring resonator, Q factor can be calculated as:

$$Q = \frac{f_o}{\delta f} = \frac{\lambda_o}{\delta \lambda} \tag{3.55}$$

In the frequency and wavelength domains, Q factor is the ratio of the absolute frequency, f_o or absolute wavelength, λ_o to the 3-dB bandwidth (δf or $\delta \lambda$). Q factor determines the shape and bandwidth of the response filter.

Finesse, F and quality factor, Q are important indeed, when one is interested in both FSR and 3-dB bandwidth. F and Q are related to each other by:

$$\frac{Q}{F} = \frac{f_o}{\Delta f} = \frac{\lambda_o}{\Delta \lambda} \tag{3.56}$$

The high cavities of Q factor are very important especially as the building block for optical signal processing application or for the laser application where high quality factors are required.

3.6 Optical Tweezers

Optical tweezers arise from the ability of light to exert the force on the matter (Neuman and Block 2004). This phenomenon originates from the basic principles of momentum (Guck et al. 2001; Wilson et al. 2005).

Newton's Second Law of Motion states that the rate of change of momentum is proportional to the imposed forced in the direction of the force (Rohrbach and Stelzer 2001).

The net force of the body is given as:

$$F = \frac{dp}{dt} = \frac{d(mv)}{dt} \tag{3.57}$$

$$F = m\frac{dv}{dt} = ma \tag{3.58}$$

where F is the net force applied, p is the momentum, m is the body's mass, v is the velocity, and a is the body's acceleration.

According to Snell's Law (Barton 1995; Summers 2009), the ray of light passing through an object is refracted.

Figure 3.6 shows the schematic diagram of the refraction of light at the interface between two media of difference refractive indices, where $n_2 > n_1$. In this phenomenon, the velocity at the second medium is lower than the velocity in the first medium ($u_2 < u_1$). The refraction angle, θ_2 is less than the incident angle, θ_2.The ray in the higher-index medium becomes closer to the normal line.

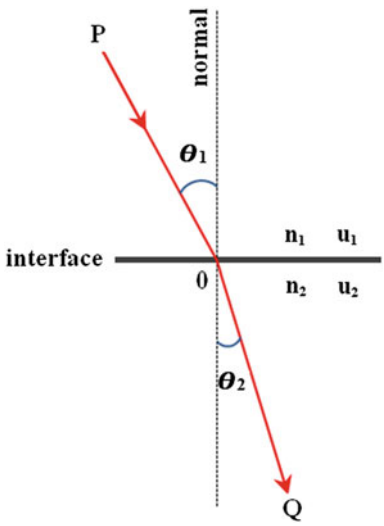

Fig. 3.6 Refraction of light between two media

Hence,

$$\frac{\sin\theta_1}{\sin\theta_2} = \frac{u_1}{u_2} = \frac{n_2}{n_1} \tag{3.59}$$

where θ_1 and θ_2 are the incident and refractive angles respectively, u_1 and u_2 are the inertial velocity and final velocity respectively, and n_1 and n_2 are the refractive indexes for the first and second mediums respectively.

As a result, the ray of light that exit the medium/molecule is slightly different in direction compared with its original angle. The angle of refracted ray is more close to the origin. The difference between the angles of incident and refraction rays shows that there is a momentum change during the process. The quantum of light possesses a momentum proportional to its energy and associated with its propagation.

The linear momentum of photon, p associate with laser beam at wavelength, λ is given as:

$$p = \frac{E}{c} \tag{3.60}$$

where E is the energy of light.
E is given as:

$$E = hf \tag{3.61}$$

where h is the Planck's constant (6.63×10^{-34} m^2 kg/s) and f is the frequency of light.

f is given as:

$$f = \frac{c}{\lambda} \tag{3.62}$$

where c is the speed of light.
From (3.60)–(3.62) the momentum of a single photon, p can be expressed as:

$$p = \frac{E}{c} = \frac{hf}{f\lambda} = \frac{h}{\lambda} \tag{3.63}$$

From (3.58), the net force, F is given as:

$$F = \frac{dp}{dt}$$

$$F = \sum_{i}^{N} \frac{\Delta p_i}{\Delta t} \tag{3.64}$$

where N is the number of photon and t is the time.

Equation (3.64) represents the region with high intensity of light (large N) and results in the greater force. This is due to the massive change in momentum compared to the region with the small values of N.

The sum of the optical force from all rays can be divided into two major components, known as scattering force, F_s and gradient force, F_g. F_s acts in the direction of the propagation light while F_g arising from the light intensity gradient and pointing toward the center of beam (Douglas et al. 2007).
F_s and F_g are related as:

$$F_{net} = F_s + F_g \tag{3.65}$$

where F_{net} is the net force.

For the normal light beam, the scattering force component dominates the particles and tends to push it away from its stable position. In order to create a stable 3-D trapping, the axial gradient force, F_g must overcome the destabilizing force, F_s. This can be realized with the existence of a very steep gradient in laser beam intensity profile. The domination of F_g ensures the stability of the optical trapping. F_g can be considered as the restoring force that pulls the particle into the center of the trap.

3.7 Self-phase Modulation

The intensity dependent refractive index (IDRI) of Kerr effect causes a series of interesting nonlinear behaviour. Self-phase modulation (SPM) and cross-phase modulation (XPM) are two major effects that been studied intensely.

SPM can be described as the self-induced phase shift experienced by ultrashort pulse of light once travelling in any nonlinear Kerr medium. The varying intensity of input optical signal results in time varying refractive index of the IDRI medium. This directly produced a varying phase change in the optical signal. The fluctuation of signal intensity causes the phase change of the signal itself as it propagates through the medium (Yang et al. 2006).

The phase change, ϕ of the optical field, E propagates over a distance L can be describes as:

$$\phi = nkL \tag{3.66}$$

$$\phi = \frac{2\pi}{\lambda} nL \tag{3.67}$$

where n and λ are the refractive index and wavelength of the propagating optical pulse respectively, and k is the wavenumber. The value of nL is known as an optical path length in nonlinear medium.

In optical fibre, n and L are replaced by the effective refractive index, n_{eff} and effective length, L_{eff} respectively. Hence,

$$\phi = \frac{2\pi}{\lambda} n_{eff} L_{eff} \tag{3.68}$$

and

$$\phi = \frac{2\pi}{\lambda} (n_o + n_2) L_{eff} \tag{3.69}$$

Equations (3.68) and (3.69) consist of two parts of phase constant which is assigned as linear and nonlinear portion respectively. Hence,

$$\phi_L = \frac{2\pi}{\lambda} n_o L_{eff} \tag{3.70}$$

$$\phi_{NL} = \frac{2\pi}{\lambda} n_2 I L_{eff} \tag{3.71}$$

Consider the intensity is time dependent, $I(t)$. The phase depends on the time change. The change in phase with time dependence induces the change in frequency spectrum.
Hence,

$$\omega = \frac{d\phi}{dt} \tag{3.72}$$

By considering a pulse with optical frequency of ω_o propagates in Kerr media, the new instantaneous frequency is given as:

$$\omega' = \omega_o + \frac{d\phi}{dt} \tag{3.73}$$

In the expression of phase $(\omega t - kz)$, the sign of SPM phase shift is negative. Thus, the phase equation can be rewritten as:

$$\phi = -\frac{2\pi}{\lambda}(n_o + n_2 I)L_{eff} \tag{3.74}$$

In an optical fibre with cross-sectional area of A_{eff}, the phase shift is induced by an optical beam of power P which is given as:

$$\phi_{SPM} = -\frac{2\pi}{\lambda}L_{eff}P\frac{n_2}{A_{eff}} \tag{3.75}$$

3.8 Photonics Signal Flow Graph Theory

Signal flow graph (SFG) theory has been introduced by Samuel Jafferson Mason in 1950s (Mason 1953). The SFG technique has been widely used in diverse fields of electronics, digital signal processing, and controlling systems. A signal flow graph is defined as a network of directed branches which connect at nodes (Tan 2004). Simply, it is a pictorial representation of the simultaneous algebraic equations describing a system and graphically displays the flow of signal through a system. The SFG method can be interpreted as a transformation of either the method of successive substitutions of simultaneous equations or the transfer matrix method to a topological approach. In general, the SFG theory can be applied to any linear time-invariant systems.

Generally, the SFG technique is used to solve a set of linear algebraic equation. It can be described as (Serpegüzel 1999):

$$x_j = \sum_{i=1}^{n} t_{ij}x_i, \qquad j = 2, 3, \ldots, n \tag{3.76}$$

where x_i is the only driving force in the system with independent variable, $x_2, x_3, \ldots, x_n$ are the dependent variables, and t_{ij} is the transmittance.

There are many advantages of using SFG technique over conventional methods. It yields a pictorial representation of the flow of signal through the system, which enhance the understanding of the operation of the systems. For the graphical simulation system using computer program, SFG can provide an easy and systematic way of manipulating the variables of interest. It also enables the solutions of any circuit problems to be obtained easily by direct inspection of the simple system.

The physical behaviour and topological properties of a simple system can be easily identified by using the SFG theory.

Transmission rule, addition rule, and product rule are the three basics rules that frequently used in photonics signal flow graph theory. The theoretical descriptions of the rules will be discussed in details at this section.

3.8.1 Transmission Rule

Transmission rule states that the value of the variable denoted by a node is transmitted on every branch leaving that node (Fig. 3.7). The expression of the transmission rule is given by:

$$x_j = t_{ij} x_i \tag{3.77}$$

where $j = 1, 2, 3, \ldots, n-1, n$.

3.8.2 Addition Rule

Addition rule states that the value of the variable denoted by a node is equal to the sum of all signals entered that node (Fig. 3.8). Mathematically, addition rule can be describes as:

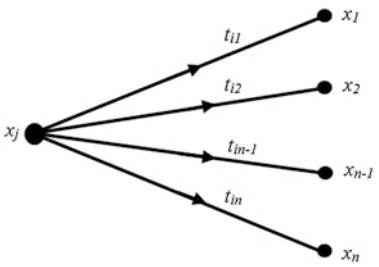

Fig. 3.7 Schematic diagram of the transmission rule

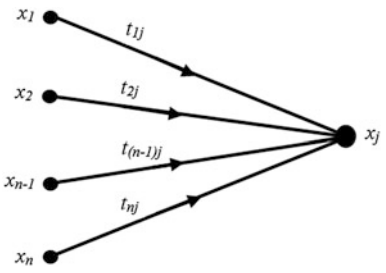

Fig. 3.8 Schematic diagram of the addition rule

Fig. 3.9 Schematic diagram of the product rule

$$x_j = \sum_{i=1}^{n} t_{ij} x_i \tag{3.78}$$

where $i = 1, 2, 3, \ldots, n-1, n$.

3.8.3 Product Rule

Product rule states that the effective transmittance of a branch is equal to the product of the transmittances of all branches in cascade (Fig. 3.9). The expression for additional rule is given as:

$$x_n = (t_{12} t_{23} \cdots t_{n-1}) x_1 \tag{3.79}$$

3.9 Z-Transform Method

The filter function arises from the interference of two or more waves. The incoming signal is split into multiple paths by division of the wavefront or its amplitude (Mario 2007). Different gratings are an example of the wavefront division while the partial reflectors are the example of the amplitude division.

As travelling along the different paths, the optical waves combine and interfere. In this case, the waves must have the same polarization, same frequency, and temporally coherent over the longest delay length. When the signals are recombined, their relative phases determine whether they interface constructively or destructively.

The phase path, ϕ is given as:

$$\phi = \beta L \tag{3.80}$$

where β is the propagation constant and L is the distance travel along the path.

The individual optical path lengths are typically integer multiples of the different smallest path length. The refractive index, n is assumed to be wavelength dependent.

The unit delay, T is defined as:

$$T = L_u \frac{n}{c} \tag{3.81}$$

where L_u is the smallest path length or the unit delay length. Each delay is an integer multiple of a unit delay length, L_u.
The phase for each path is then expressed as a multiple of βL_u. Hence,

$$\phi_P = P\beta L_u \tag{3.82}$$

where P is an integer.
The total transverse electric field, E_{out} for N path is given as:

$$E_{out} = E_o e^{-j\phi_o} + E_1 e^{-j\phi_1} + E_2 e^{-j\phi_2} + \cdots + E_{N-1} e^{-j\phi_{N-1}} \tag{3.83}$$

To obtain a Z-transform of E_{out}, the phase can be expressed as a multiple of the unit delay, T. By using the expression of $\Omega = 2\pi v$ and $c = v\lambda$,

$$\beta L_u = \frac{2\pi n L_u}{\lambda}$$

$$\beta L_u = \frac{2\pi v n L_u}{c}$$

$$\beta L_u = \frac{\Omega L_u n}{c}$$

$$\beta L_u = \Omega T \tag{3.84}$$

Equation (3.84) brings to:

$$\phi_P = P\beta L_u = P\Omega T \tag{3.85}$$

Therefore, (3.83) becomes:

$$E_{out} = E_o e^{-j0} + E_1 e^{-j\Omega T} + E_2 e^{-j2\Omega T} + \cdots + E_{N-1} e^{-j(N-1)\Omega T} \tag{3.86}$$

For dispersion-less line, unit delay, T is a constant. By using $z = e^{j\Omega T}$, (3.86) becomes:

$$E_{out} = E_o + E_1 z^{-1} + E_2 z^{-2} + \cdots + E_{N-1} z^{-(N-1)} \tag{3.87}$$

Because of the multiples of unit delay, the frequency response is periodic. One period is defined as the free spectral range, FSR which is given as:

$$FSR = \frac{1}{T} \tag{3.88}$$

From $f = \frac{\omega}{2\pi}$, the optical frequency can be rewritten as:

$$f = (v - v_c)T \tag{3.89}$$

or

$$f = \frac{\Omega - \Omega_c}{2\pi} T \tag{3.90}$$

where v_c is the center frequency.
v_c is given as:

$$v_c = \frac{c}{\lambda_c} \tag{3.91}$$

The propagation loss of a delay line is counted by multiplying $z - 1$ by $e^{-\frac{\alpha L}{2}}$, where α is the average loss per unit length and L is the delay path length.
From (3.88), FSR is then given as:

$$FSR = \frac{c}{n_g L_U} \tag{3.92}$$

Hence,

$$T = \frac{n_g L_u}{c} \tag{3.93}$$

where n_g is the group refractive index evaluated at either center frequency, f_o or center wavelength, λ_o.
n_g in terms of f_o and λ_o are given as:

$$n_g = n_{eff} + f_o \left(\frac{dn_{eff}}{df} \right)_{f_o} \tag{3.94}$$

or

$$n_g = n_{eff} + \lambda_o \left(\frac{dn_{eff}}{d\lambda} \right)_{\lambda_o} \tag{3.95}$$

The optical circuit can be analysed with Z-transform method using waveguide delay and directional coupler. It is used for splitting and combining more than one

signal. Two waveguides are brought close together so that their evanescent fields overlap each other. The circuits are assumed to be linear and invariant. A power coupling ratio, κ is associated with each directional input power. The coupling ratio determines by the length of the region where the waveguides are coupled. It is assumed that the wavelength is independent. This brings the matrix elements to be constant.
The through and cross ports transmission beam are given as (Mitatha et al. 2011):

$$c = \cos\theta = \sqrt{(1-\gamma)(1-\kappa)} \tag{3.96}$$

and

$$-js = -j\sin\theta = -j\sqrt{(1-\gamma)\kappa} \tag{3.97}$$

where γ is the coupling loss.

Chapter 4
Research Methodology

4.1 Introduction

This chapter describes the methodologies used for the simulation process of this research. Every system, either add-drop or PANDA ring resonator systems consists of a series of microring resonator, connected with two bus waveguides at the top and bottom of the center microring. The mathematical formulation and modelling description of proposed systems are described in details. The transfer functions for each model operating systems are derived based on actual practical device values. The whole process starting from the generation of input signals until the end of the process is expressed in the flow charts. All the simulation analysis are done by using MatLab programming software.

4.2 Add-Drop Configuration System

The add-drop configuration system consists of unidirectional coupling between a ring resonator and fibre waveguides as shown in Fig. 4.1. The system consists of one microring resonator which is connecting with two bus waveguides at the top and bottom of the ring. The waveguides are coupled into the ring resonator by the coupling coefficients κ_1 and κ_2 respectively. When an input electric field is coupled into the ring waveguide through an external bus waveguide, a positive feedback is induced and the field inside the ring resonator starts to build-up.
The circumference of the ring, L is given as:

$$L = 2\pi R \tag{4.1}$$

where R is the radius of the ring measured from the center of the ring to the center of the waveguide.

S. Daud et al., *Simulation of Optical Soliton Control in Micro- and Nanoring Resonator Systems*, SpringerBriefs in Physics, DOI 10.1007/978-3-319-15485-5_4

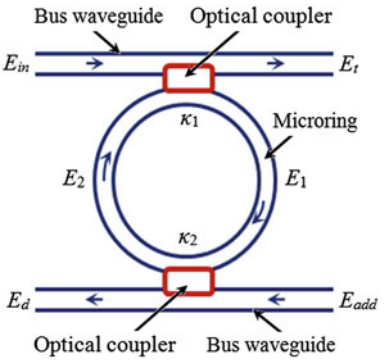

Fig. 4.1 Add-drop configuration system

For an input in one port, the power coupled to the system is t times the input power for through-path transmission and κ times the input power for cross-path transmission. t and κ are the coupling parameters, where κ is the cross-coupling coefficient and t is the self-coupling coefficient of the waveguide. κ is associated with each transmission field that pass through the coupler and γ is a coupling intensity loss for the field amplitude. γ is equal to zero for the lossless coupling. t and κ are related as (Yupapin et al. 2008):

$$\left|\kappa^2\right| + \left|t^2\right| = 1 \tag{4.2}$$

The transmission for one complete roundtrip is represented as:

$$\exp\left(\frac{-\alpha L}{2} - jk_n L\right) \tag{4.3}$$

Then, the Z-transform parameter is given as (Absil 2000):

$$z^{-1} = \exp^{-jk_n L} \tag{4.4}$$

where $k_n = \frac{2\pi}{\lambda} n_{eff}$ is the propagation constant, λ is the wavelength, and n_{eff} is the effective refractive index of the waveguide.
The roundtrip loss inside ring is given as:

$$\exp\left(\frac{-\alpha L}{2}\right) \tag{4.5}$$

where α is referred to intensity attenuation coefficient, including the propagation loss.

The losses are resulted from the transitions in the curvature of the ring and bending losses. The value of α depends on the properties of the material and waveguide used.

It is assumed that the coupling is lossless ($\gamma = 0$). There are no power or intensity losses in the coupling region. It is also assumed that there is no phase change for the field that passes through the coupling region ($\Delta\phi = 0$). There is no significance value of the coupling distance because the coupling takes place on a point between the tangential circular arc of the ring and input waveguide.

The transmitted and throughput output field at the output waveguide are given as:

$$a = \exp\left(\frac{-\alpha L}{2}\right) \tag{4.6}$$

From input E_{in}, the transmission optical field E_t at throughput port is given as (Yupapin et al. 2008):

$$E_t = \left[t_1 + (-\kappa_1)^2(t_2)\left(z^{-1}\right)(a) \cdot \left\{1 + \left(t_1 t_2 a z^{-1}\right) + \left(t_1 t_2 a z^{-1}\right)^2 + \cdots \left(t_1 t_2 a z^{-1}\right)^n\right\}\right] \tag{4.7}$$

By using Taylor's expansion series, (4.7) can be simplified as:

$$E_t = \left[t_1 - \frac{a z^{-1} t_2 \kappa_1^2}{1 - \left(t_1 t_2 a z^{-1}\right)}\right] \cdot E_{in} \tag{4.8}$$

$$E_t = \left[\frac{t_1 - t_2 a z^{-1}\left(t_1^2 + \kappa_1^2\right)}{1 - \left(t_1 t_2 a z^{-1}\right)}\right] \cdot E_{in} \tag{4.9}$$

From (4.2),

$$E_t = \left[\frac{t_1 - t_2 a z^{-1}}{1 - t_1 t_2 a z^{-1}}\right] \cdot E_{in} \tag{4.10}$$

Hence, the transfer function, H_{11} can be written as:

$$H_{11} = \frac{E_t}{E_{in}} \tag{4.11}$$

$$H_{11} = \left[\frac{t_1 - t_2 a z^{-1}}{1 - t_1 t_2 a z^{-1}}\right] \tag{4.12}$$

The transmission power, P_t is then given as (Yupapin et al. 2008):

$$P_t = E_t \cdot E_t^* \tag{4.13}$$

$$P_t = \left[\frac{t_1 - t_2 a e^{-jk_n L}}{1 - \left(t_1 t_2 a e^{-jk_n L}\right)}\right] \cdot \left[\frac{t_1 - t_2 a e^{+jk_n L}}{1 - \left(t_1 t_2 a e^{+jk_n L}\right)}\right] \cdot E_{in}^2 \tag{4.14}$$

$$P_t = \frac{t_1^2 - t_1 t_2 a e^{-jk_n L} - t_1 t_2 a e^{jk_n L} + a^2 t_2^2}{1 - a t_1 t_2 e^{-jk_n L} - a t_1 t_2 e^{jk_n L} + a^2 t_1^2 t_2^2} \cdot E_{in}^2 \tag{4.15}$$

$$P_t = \frac{t_1^2 + a^2 t_2^2 - a t_1 t_2 \left(e^{-jk_n L} + e^{jk_n L}\right)}{1 + a^2 t_1^2 t_2^2 - a t_1 t_2 (e^{-jk_n L} + e^{jk_n L})} \cdot E_{in}^2 \tag{4.16}$$

By using

$$e^{jx} = \cos(x) + j\sin(x) \text{ and } e^{-jx} = \cos(x) - j\sin(x), \tag{4.17}$$

becomes:

$$P_t = \frac{t_1^2 + a^2 t_2^2 - 2a t_1 t_2 \cos(k_n L)}{1 + a^2 t_1^2 t_2^2 - 2a t_1 t_2 \cos(k_n L)} \cdot E_{in}^2 \tag{4.18}$$

The transmission optical field, E_d at drop port, from input E_{in} is given as:

$$E_d = \left[-\kappa_1 \kappa_2 \sqrt{a}\sqrt{z^{-1}} \cdot \left\{1 + \left(t_1 t_2 a z^{-1}\right) + \left(t_1 t_2 a z^{-1}\right)^2 + \cdots + \left(t_1 t_2 a z^{-1}\right)^n\right\}\right] \cdot E_{in} \tag{4.19}$$

$$E_d = \left[\frac{-\kappa_1 \kappa_2 \sqrt{a z^{-1}}}{1 - t_1 t_2 a z^{-1}}\right] \cdot E_{in} \tag{4.20}$$

Similarly, the transfer function, H_{12} can be written as:

$$H_{12} = \frac{E_d}{E_{in}} \tag{4.21}$$

$$H_{12} = \left[\frac{-\kappa_1 \kappa_2 \sqrt{a z^{-1}}}{1 - t_1 t_2 a z^{-1}}\right] \tag{4.22}$$

The transmission power, P_d is given as:

$$P_d = E_d \cdot E_d^* \tag{4.23}$$

$$P_d = \left[\frac{-\kappa_1 \kappa_2 \sqrt{a} e^{-jk_n L/2}}{1 - t_1 t_2 a e^{-jk_n L}}\right] \cdot \left[\frac{-\kappa_1 \kappa_2 \sqrt{a} e^{jk_n L/2}}{1 - t_1 t_2 a e^{jk_n L}}\right] \cdot E_{in}^2 \tag{4.24}$$

$$P_d = \frac{a\left(1 - t_1^2\right)\left(1 - t_2^2\right)}{1 + a^2 t_1^2 t_2^2 - 2a t_1 t_2 \cos(k_n L)} \cdot E_{in}^2 \tag{4.25}$$

The transmission optical field, E_t at throughput port, from input E_{in} is given as:

$$E_t = \left[-\kappa_1\kappa_2\sqrt{a}\sqrt{z^{-1}} \cdot \left\{1 + \left(t_1t_2az^{-1}\right) + \left(t_1t_2az^{-1}\right)^2 + \cdots + \left(t_1t_2az^{-1}\right)^n\right\}\right] \cdot E_{add} \tag{4.26}$$

$$E_t = \left[\frac{-\kappa_1\kappa_2\sqrt{az^{-1}}}{1 - t_1t_2az^{-1}}\right] \cdot E_{add} \tag{4.27}$$

Hence, the transfer function, H_{21} can be expressed as:

$$H_{21} = \frac{E_t}{E_{add}} \tag{4.28}$$

$$H_{21} = \left[\frac{-\kappa_1\kappa_2\sqrt{az^{-1}}}{1 - t_1t_2az^{-1}}\right] \tag{4.29}$$

The transmission power, P_t is given as:

$$P_t = E_t \cdot E_t^* \tag{4.30}$$

$$P_t = \left[\frac{-\kappa_1\kappa_2\sqrt{a}e^{-jk_nL/2}}{1 - t_1t_2ae^{-jk_nL}}\right] \cdot \left[\frac{-\kappa_1\kappa_2\sqrt{a}e^{jk_nL/2}}{1 - t_1t_2ae^{jk_nL}}\right] \cdot E_{add}^2 \tag{4.31}$$

$$P_t = \frac{a\left(1 - t_1^2\right)\left(1 - t_2^2\right)}{1 + a^2t_1^2t_2^2 - 2at_1t_2\cos(k_nL)} \cdot E_{add}^2 \tag{4.32}$$

The transmission optical field E_d at drop port from input E_{add} is given as:

$$E_d = \left[t_2 + (-\kappa_2)^2(t_1)\left(z^{-1}\right)(a) \cdot \left\{1 + \left(t_1t_2az^{-1}\right) + \left(t_1t_2az^{-1}\right)^2 + \cdots + \left(t_1t_2az^{-1}\right)^n\right\}\right] \cdot E_{add} \tag{4.33}$$

$$E_d = \left[t_2 - \frac{az^{-1}t_1\kappa_2^2}{1 - t_1t_2az^{-1}}\right] \cdot E_{add} \tag{4.34}$$

$$E_d = \left[\frac{t_2 - t_1az^{-1}}{1 - t_1t_2az^{-1}}\right] \cdot E_{add} \tag{4.35}$$

Hence, the transfer function H_{22} can be expressed as:

$$H_{22} = \frac{E_d}{E_{add}} \tag{4.36}$$

$$H_{22} = \left[\frac{t_2 - t_1 a z^{-1}}{1 - t_1 t_2 a z^{-1}}\right] \tag{4.37}$$

The transmission power, P_d is given as:

$$P_d = E_d \cdot E_d^* \tag{4.38}$$

$$P_d = \left[\frac{t_2 - t_1 a e^{-jk_n L}}{1 - t_1 t_2 a e^{-jk_n L}}\right] \cdot \left[\frac{t_2 - t_1 a e^{jk_n L}}{1 - t_1 t_2 a e^{jk_n L}}\right] \cdot E_{add}^2 \tag{4.39}$$

$$P_d = \frac{t_2^2 + a^2 t_1^2 - 2a t_1 t_2 \cos(k_n L)}{1 + a^2 t_1^2 t_2^2 - 2a t_1 t_2 \cos(k_n L)} \cdot E_{add}^2 \tag{4.40}$$

Finally, the transfer functions for the resonator system are defined as follows:

$$H_{11} = \left[\frac{t_1 - t_2 a z^{-1}}{1 - t_1 t_2 a z^{-1}}\right] \tag{4.41}$$

$$H_{12} = \left[\frac{-\kappa_1 \kappa_2 \sqrt{a z^{-1}}}{1 - t_1 t_2 a z^{-1}}\right] \tag{4.42}$$

$$H_{21} = \left[\frac{-\kappa_1 \kappa_2 \sqrt{a z^{-1}}}{1 - t_1 t_2 a z^{-1}}\right] \tag{4.43}$$

$$H_{22} = \left[\frac{t_2 - t_1 a z^{-1}}{1 - t_1 t_2 a z^{-1}}\right] \tag{4.44}$$

The scattering matrix method is used to obtain the total optical transmission field at throughput and drop ports, which is given as:

$$\begin{bmatrix} E_t \\ E_d \end{bmatrix} = S_R \begin{bmatrix} E_{in} \\ E_{add} \end{bmatrix} \tag{4.45}$$

where S_R is the abbreviations of the ring system.
S_R is given as:

$$S_R = \begin{bmatrix} H_{11} & H_{12} \\ H_{21} & H_{22} \end{bmatrix} \tag{4.46}$$

$$S_R = \begin{bmatrix} \left[\frac{t_1 - t_2 a z^{-1}}{1 - t_1 t_2 a z^{-1}}\right] & \left[\frac{-\kappa_1 \kappa_2 2\sqrt{a z^{-1}}}{1 - t_1 t_2 a z^{-1}}\right] \\ \left[\frac{-\kappa_1 \kappa_2 \sqrt{a z^{-1}}}{1 - t_1 t_2 a z^{-1}}\right] & \left[\frac{t_2 - t_1 a z^{-1}}{1 - t_1 t_2 a z^{-1}}\right] \end{bmatrix} \tag{4.47}$$

Hence,

$$\begin{bmatrix} E_t \\ E_d \end{bmatrix} = \begin{bmatrix} \left[\frac{t_1 - t_2 a z^{-1}}{1 - t_1 t_2 a z^{-1}}\right] & \left[\frac{-\kappa_1 \kappa_2 2\sqrt{a z^{-1}}}{1 - t_1 t_2 a z^{-1}}\right] \\ \left[\frac{-\kappa_1 \kappa_2 \sqrt{a z^{-1}}}{1 - t_1 t_2 a z^{-1}}\right] & \left[\frac{t_2 - t_1 a z^{-1}}{1 - t_1 t_2 a z^{-1}}\right] \end{bmatrix} \begin{bmatrix} E_{in} \\ E_{add} \end{bmatrix} \tag{4.48}$$

By solving the matrix, (4.48) becomes:

$$E_t = E_{throughput} = \left[\frac{t_1 - t_2 a z^{-1}}{1 - t_1 t_2 a z^{-1}}\right] \cdot E_{i1} + \left[\frac{-\kappa_1 \kappa_2 2\sqrt{a z^{-1}}}{1 - t_1 t_2 a z^{-1}}\right] \cdot E_{add} \tag{4.49}$$

and

$$E_d = E_{drop} = \left[\frac{-\kappa_1 \kappa_2 \sqrt{a z^{-1}}}{1 - t_1 t_2 a z^{-1}}\right] \cdot E_{i1} + \left[\frac{t_2 - t_1 a z^{-1}}{1 - t_1 t_2 a z^{-1}}\right] \cdot E_{add} \tag{4.50}$$

The interaction between the input optical field, E_{in} and control signal, E_{add} occurs inside the ring resonator waveguide. The circulated optical fields, E_1 and E_2 inside the system can be written as follows.
Circulated field E_{11}, from input field E_{in} is given as:

$$E_{11} = \left[-\kappa_1 \sqrt{a z^{-1}} \cdot \left\{1 + \left(t_1 t_2 a z^{-1}\right) + \left(t_1 t_2 a z^{-1}\right)^2 + \cdots + \left(t_1 t_2 a z^{-1}\right)^n\right\}\right] \cdot E_{in} \tag{4.51}$$

$$E_{11} = \left[\frac{-\kappa_1 \sqrt{a z^{-1}}}{1 - t_1 t_2 a z^{-1}}\right] \cdot E_{in} \tag{4.52}$$

Similarly, circulated field E_{12} from input field E_{add} can be expressed as:

$$E_{12} = \left[-t_1 \kappa_2 a z^{-1} \cdot \left\{1 + \left(t_1 t_2 a z^{-1}\right) + \left(t_1 t_2 a z^{-1}\right)^2 + \cdots + \left(t_1 t_2 a z^{-1}\right)^n\right\}\right] \cdot E_{add} \tag{4.53}$$

$$E_{12} = \left[\frac{-t_1 \kappa_2 a z^{-1}}{1 - t_1 t_2 a z^{-1}}\right] \cdot E_{add} \tag{4.54}$$

Total circulated optical field, E_1 is then given as:

$$E_1 = E_{11} + E_{12} \tag{4.55}$$

$$E_1 = \left[\frac{-\kappa_1 \sqrt{a z^{-1}}}{1 - t_1 t_2 a z^{-1}}\right] \cdot E_{in} + \left[\frac{-t_1 \kappa_2 a z^{-1}}{1 - t_1 t_2 a z^{-1}}\right] \cdot E_{add} \tag{4.56}$$

Circulated field E_{21} from input field E_{in} can be expressed as:

$$E_{21} = \left[-t_2\kappa_1 az^{-1} \cdot \left\{1 + \left(t_1t_2az^{-1}\right) + \left(t_1t_2az^{-1}\right)^2 + \cdots + \left(t_1t_2az^{-1}\right)^n\right\}\right]E_{in} \tag{4.57}$$

$$E_{21} = \left[\frac{-t_2\kappa_1 az^{-1}}{1 - t_1t_2az^{-1}}\right] \cdot E_{in} \tag{4.58}$$

Similarly, circulated field E_{22} from input field E_{add} is given as:

$$E_{22} = \left[-\kappa_2\sqrt{az^{-1}}\left\{1 + \left(t_1t_2az^{-1}\right) + \left(t_1t_2az^{-1}\right)^2 + \cdots + \left(t_1t_2az^{-1}\right)^n\right\}\right] \cdot E_{add} \tag{4.59}$$

$$E_{22} = \left[\frac{-\kappa_2\sqrt{az^{-1}}}{1 - t_1t_2az^{-1}}\right] \cdot E_{add} \tag{4.60}$$

Total circulated optical field, E_2 is given as:

$$E_2 = \left[\frac{-t_2\kappa_1 az^{-1}}{1 - t_1t_2az^{-1}}\right] \cdot E_{in} + \left[\frac{-\kappa_2\sqrt{az^{-1}}}{1 - t_1t_2az^{-1}}\right] \cdot E_{add} \tag{4.61}$$

Hence, the transmission fields at E_1 and E_2 are given as:

$$E_1 = \left[\frac{-\kappa_1\sqrt{az^{-1}}}{1 - t_1t_2az^{-1}}\right] \cdot E_{in} + \left[\frac{-t_1\kappa_2 az^{-1}}{1 - t_1t_2az^{-1}}\right] \cdot E_{add} \tag{4.62}$$

and

$$E_2 = \left[\frac{-t_2\kappa_1 az^{-1}}{1 - t_1t_2az^{-1}}\right] \cdot E_{in} + \left[\frac{-\kappa_2\sqrt{az^{-1}}}{1 - t_1t_2az^{-1}}\right] \cdot E_{add} \tag{4.63}$$

Finally, the output fields at throughput and drop ports are given as:

$$E_t = \left[\frac{t_1 - t_2az^{-1}}{1 - t_1t_2az^{-1}}\right] \cdot E_{in} + \left[\frac{-\kappa_1\kappa_2 2\sqrt{az^{-1}}}{1 - t_1t_2az^{-1}}\right] \cdot E_{add} \tag{4.64}$$

and

$$E_d = \left[\frac{-\kappa_1\kappa_2\sqrt{az^{-1}}}{1 - t_1t_2az^{-1}}\right] \cdot E_{in} + \left[\frac{t_2 - t_1az^{-1}}{1 - t_1t_2az^{-1}}\right] \cdot E_{add} \tag{4.65}$$

4.3 PANDA Ring Resonator System

PANDA ring resonator system consists of an add-drop interferometer system and two nanoring resonators. Two bus waveguides are coupled on top and bottom of the center microring while two nanorings are coupled on the right and left-hand sides of the center microring respectively. The microring resonator is connected to the bus waveguides and two nanorings by the coupling coefficient depicted as κ_1, κ_2, κ_3, and κ_4 respectively. The system represents a new technique of combination and integration of micro- and nanoring resonators which can be widely used to improve the secured communication and the high capacity of optical signal proceeding especially in communication network. The schematic diagram of PANDA ring resonator system is as shown in Fig. 4.2.

There are four main ports in this system, which are input, add, throughput, and drop ports respectively. The input optical signals are launched into the input and add ports of the system while the corresponding signals ejected from the system through the throughput and drop ports respectively. All the characteristics of the output signals will be examined and discussed in details in the next chapter.

As depicted in Fig. 4.2, E_{in}, E_{add}, E_t, and E_d are the abbreviations of input port, add port, throughput port, and drop port respectively. E_1, E_2, E_3, and E_4 are the circulating optical fields associated with the center microring, R. κ_1 and κ_2 are assigned as the coupling parameters for the waveguides while κ_3 and κ_4 are the coupling parameters for the coupling between the center microring and both right and left nanorings respectively.

By assuming,

$$x_1 = \sqrt{1-\gamma_1} \quad x_2 = \sqrt{1-\gamma_2}$$

$$x_3 = \sqrt{1-\gamma_3} \quad x_4 = \sqrt{1-\gamma_4}$$

and

$$y_1 = \sqrt{1-\kappa_1} \quad y_2 = \sqrt{1-\kappa_2}$$

$$y_3 = \sqrt{1-\kappa_3} \quad y_4 = \sqrt{1-\kappa_4}$$

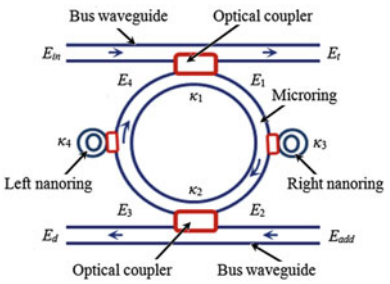

Fig. 4.2 PANDA ring resonator configuration system

The expression for output fields at throughput port, E_t and drop port, E_d are given as:

$$E_t = x_1 y_1 E_{in} + j x_1 \sqrt{\kappa_1} E_4 \tag{4.66}$$

and

$$E_d = x_2 y_2 E_{add} + j x_2 \sqrt{\kappa_2} E_2 \tag{4.67}$$

where γ_1, γ_2, γ_3, and γ_4 are the intensity insertion loss coefficient of different coupler in the system and κ_1, κ_2, κ_3, and κ_4 are the coupling coefficients of the system.
By assuming,

$$\phi = -\frac{\alpha L}{2} - j k_n L \tag{4.68}$$

Hence,

$$\phi_R = -\frac{\alpha L_R}{2} - j k_n L_R \tag{4.69}$$

and

$$\phi_L = -\frac{\alpha L_L}{2} - j k_n L_L \tag{4.70}$$

where L, L_R, and L_L are the circumferences of center, right and left rings respectively.

4.3.1 Right Nanoring of PANDA Ring Resonator System

The circulating fields on the right nanoring are given as (Aziz 2013):

$$E_{R1} = j x_3 \sqrt{\kappa_3} E_1 \exp\left(\frac{\phi}{4}\right) + x_3 y_3 E_{R2} \tag{4.71}$$

$$E_{R2} = E_{R1} \exp(\phi_R) \tag{4.72}$$

By substituting (4.71) into (4.72), E_{R2} can be simplified to be:

$$E_{R2} = \frac{j x_3 \sqrt{\kappa_3} E_1 \exp\left(\phi_R + \frac{\phi}{4}\right)}{1 - x_3 y_3 \exp(\phi_R)} \tag{4.73}$$

Hence,

$$E_R = x_3 y_3 E_1 \exp\left(\frac{\phi}{4}\right) + jx_3\sqrt{\kappa_3}E_{R2} \tag{4.74}$$

By substituting (4.73) into (4.74), the expression for E_R in terms of E_1 can be rewritten as:

$$E_R = x_3 y_3 E_1 \exp\left(\frac{\phi}{4}\right) + jx_3\sqrt{\kappa_3}\left[\frac{jx_3\sqrt{\kappa_3}E_1 \exp\left(\phi_R + \frac{\phi}{4}\right)}{1 - x_3 y_3 \exp(\phi_R)}\right] \tag{4.75}$$

$$E_R = E_1 \exp\left(\frac{\phi}{4}\right)\left[\frac{x_3 y_3 - x_3^2 \exp(\phi_R)}{1 - x_3 y_3 \exp(\phi_R)}\right] \tag{4.76}$$

4.3.2 Left Nanoring of PANDA Ring Resonator System

Similarly, the circulating fields on the left nanoring are given as (Aziz 2013):

$$E_{L1} = jx_4\sqrt{\kappa_4}E_3 \exp\left(\frac{\phi}{4}\right) + x_4 y_4 E_{L2} \tag{4.77}$$

$$E_{L2} = E_{L1} \exp(\phi_L) \tag{4.78}$$

By substituting (4.77) into (4.78), E_{L2} can be simplified as:

$$E_{L2} = \frac{jx_4\sqrt{\kappa_4}E_3 \exp\left(\phi_L + \frac{\phi}{4}\right)}{1 - x_4 y_4 \exp(\phi_L)} \tag{4.79}$$

Hence,

$$E_L = x_4 y_4 E_3 \exp\left(\frac{\phi}{4}\right) + jx_4\sqrt{\kappa_4}E_{L2} \tag{4.80}$$

By substituting (4.79) into (4.80), the expression for E_L in terms of E_3 can be rewritten as:

$$E_L = x_4 y_4 E_3 \exp\left(\frac{\phi}{4}\right) + jx_4\sqrt{\kappa_4}\left[\frac{jx_4\sqrt{\kappa_4}E_3 \exp\left(\phi_L + \frac{\phi}{4}\right)}{1 - x_4 y_4 \exp(\phi_L)}\right] \tag{4.81}$$

$$E_L = E_3 \exp\left(\frac{\phi}{4}\right)\left[\frac{x_4 y_4 - x_4^2 \exp(\phi_L)}{1 - x_4 y_4 \exp(\phi_L)}\right] \tag{4.82}$$

Therefore, the expressions for circulating fields at four different points in the center ring resonator are given as:

$$E_1 = jx_1\sqrt{\kappa_1}E_{in} + x_1 y_1 E_4 \tag{4.83}$$

$$E_2 = E_1 E_R \exp\left(\frac{\phi}{2}\right) \tag{4.84}$$

$$E_3 = jx_2\sqrt{\kappa_2}E_{add} + x_2 y_2 E_2 \tag{4.85}$$

$$E_4 = E_3 E_L \exp\left(\frac{\phi}{2}\right) \tag{4.86}$$

By using the expressions in (4.82), (4.85), and (4.86), the expression for E_4 can be rewritten as:

$$E_4 = \frac{jx_2\sqrt{\kappa_2}E_L E_{add}\exp\left(\frac{\phi}{2}\right) + jx_1 x_2 y_2\sqrt{\kappa_1}E_R E_L E_{in}\exp(\phi)}{1 - x_1 x_2 y_1 y_2 E_R E_L \exp(\phi)} \tag{4.87}$$

By substituting (4.87) into (4.83), E_1 becomes:

$$E_1 = \frac{jx_1\sqrt{\kappa_1}E_{in} + jx_1 x_2 y_1\sqrt{\kappa_2}E_L E_{add}\exp\left(\frac{\phi}{2}\right)}{1 - x_1 x_2 y_1 y_2 E_R E_L \exp(\phi)} \tag{4.88}$$

Equations (4.87) and (4.88) describe the relation between the circulating fields E_1 and E_4 in terms of input and control signals.
Similarly, E_2 and E_3 can be rewritten as:

$$E_2 = \frac{jx_1\sqrt{\kappa_1}E_R E_{in}\exp\left(\frac{\phi}{2}\right) + jx_1 x_2 y_1\sqrt{\kappa_2}E_R E_L E_{add}\exp(\phi)}{1 - x_1 x_2 y_1 y_2 E_R E_L \exp(\phi)} \tag{4.89}$$

$$E_3 = \frac{jx_2\sqrt{\kappa_2}E_{add} + jx_1 x_2 y_2\sqrt{\kappa_1}E_R E_{in}\exp\left(\frac{\phi}{2}\right)}{1 - x_1 x_2 y_1 y_2 E_R E_L \exp(\phi)} \tag{4.90}$$

Finally, the output signals ejected from the system at throughput and drop ports are given as:

$$E_t = \frac{x_1 y_1 E_{in} - x_1 x_2 \sqrt{\kappa_1}\sqrt{\kappa_2} E_L E_{add} \exp\left(\frac{\phi}{2}\right) - x_1^2 x_2 y_2 E_R E_L E_{in} \exp(\phi)}{1 - x_1 x_2 y_1 y_2 E_R E_L \exp(\phi)} \quad (4.91)$$

and

$$E_d = \frac{x_2 y_2 E_{add} - x_1 x_2 \sqrt{\kappa_1}\sqrt{\kappa_2} E_R E_{in} \exp\left(\frac{\phi}{2}\right) - x_1 x_2^2 y_1 E_R E_L E_{add} \exp(\phi)}{1 - x_1 x_2 y_1 y_2 E_R E_L \exp(\phi)} \quad (4.92)$$

4.4 Modelling Consideration

This section will discuss on the dynamical simulation and calculation of the electromagnetic fields propagating within nonlinear fibre ring resonator. The analytical expression and formulation of the fibre optic ring resonator systems are derived previously. The optical transfer function of the operating systems obtained based on the light transmission theory by taking into account the refractive index deformation due to the nonlinear Kerr effect. The numerical method used in simulation and calculation process of the output signals are discussed in details.

Based on the suitability in engineering and numeric scientific computation, MatLab programming software is chosen as the programming device. This program may process any types of data in complex and matrix form which is constructed from a rectangular array at either real or complex elements. This program provides user with powerful graphic facilities for two and three-dimensional plotting (Attaway 2011). Such program also offers precise numeric computations, data acquisition, algorithm development, prototyping, modelling, and simulation.

In comparison with C and Python languages, MatLab programming runs in shorter execute speed, which provides clear and intuitive system and allows better algorithm solution for the centre complex problems (Fangohr 2004). In this research, the analysis and simulation processes are done by using MatLab programming software version R2010b.

4.4.1 Add-Drop Configuration System Modelling

The schematic diagram of an add-drop configuration system is depicted earlier in Fig. 4.1. The circulating fields of add-drop system are assigned at two different points, marked with E_1 and E_2 respectively.

The expressions for these circulating fields are given as:

$$E_1 = \left[\frac{-\kappa_1\sqrt{az^{-1}}}{1 - t_1 t_2 az^{-1}}\right] \cdot E_{in} + \left[\frac{-t_1\kappa_2 az^{-1}}{1 - t_1 t_2 az^{-1}}\right] \cdot E_{add} \tag{4.93}$$

and

$$E_2 = \left[\frac{-t_2\kappa_1 az^{-1}}{1 - t_1 t_2 az^{-1}}\right] E_{in} + \left[\frac{-\kappa_2\sqrt{az^{-1}}}{1 - t_1 t_2 az^{-1}}\right] \cdot E_{add} \tag{4.94}$$

From (4.93) to (4.94), the output signals ejected from the system at throughput and drop ports are given as:

$$E_t = \left[\frac{t_1 - t_2 az^{-1}}{1 - t_1 t_2 az^{-1}}\right] \cdot E_{in} + \left[\frac{-\kappa_1\kappa_2 2\sqrt{az^{-1}}}{1 - t_1 t_2 az^{-1}}\right] \cdot E_{add} \tag{4.95}$$

and

$$E_d = \left[\frac{-\kappa_1\kappa_2\sqrt{az^{-1}}}{1 - t_1 t_2 az^{-1}}\right] \cdot E_{in} + \left[\frac{t_2 - t_1 az^{-1}}{1 - t_1 t_2 az^{-1}}\right] \cdot E_{add} \tag{4.96}$$

During the simulation process, dark soliton is chosen as the input signal, E_{in} and Gaussian beam as the control signal, E_{add}. Dark soliton is chosen as the input signal because of the high security of the signal which is very important for the communication purposes. It is not easily can be detected by using normal photodetector. Meanwhile, the Gaussian beam is chosen as the control signal due to the characteristics of this laser type which is useful indeed for the fibre resonator technology. The expression for E_{in} and E_{add} are given as (Jalil et al. 2011):

$$E_{in} = A \tanh\left[\frac{T}{T_o}\right] \exp\left[\left(\frac{z}{2L_D}\right) - i\omega_o t\right] \tag{4.97}$$

and

$$E_{add} = E_o \exp\left[\left(\frac{z}{2L_D}\right) - i\omega_o t\right] \tag{4.98}$$

where A and z are the optical field amplitude and propagation distance respectively. T is the time of soliton pulse propagating in a moving frame, where $T = t - \beta_1 z$. $L_D = T_o^2/|\beta_2|$ is the dispersion length of the soliton pulse, where β_1 and β_2 are the coefficients of the linear and second-order terms of Taylor expansion of the propagation constant. T_o be the soliton pulse propagating time at initial input or soliton pulse shift time and ω_o is the frequency shift of the soliton.

This solution describes a pulse that kept its temporal width invariance as it propagates. Once soliton peak intensity, $\left|\beta_2/\Gamma T_o^2\right|$ is given, the values of T_o can be determined. In a microring device, a balance between the dispersion length, L_D and the nonlinear length, L_{NL} should be achieved. Dispersion length, L_D is the length travel by the light that cause the significance of the dispersion while the nonlinear length, L_{NL} is the length travel by light in nonlinear medium that cause significance value in dispersion.
The nonlinear length, L_{NL} is given as:

$$L_{NL} = \frac{1}{\Gamma \phi_{NL}} \tag{4.99}$$

where $\Gamma = n_2 k$ is the length scale over which dispersive or nonlinear effects make the beam wider or narrower. Here, n_2 is the nonlinear refractive index and k is the wavenumber.

For a soliton pulse, there is a balance between dispersion and nonlinear lengths. Hence,

$$L_D = L_{ND} \tag{4.100}$$

In this research, the circulating and output fields, E_1, E_2, E_t, and E_d are simulated based on the (4.95)–(4.98) derived earlier. All parameters used on the system are strongly effected the characteristics of these fields region. Thus, some key parameters are varied and the output signals are recorded and analyzed.

During the simulation process, certain key parameters are controlled and varied in order to optimized the output signals, either at throughput or drop ports of the system. By simulating the expressions in (4.95)–(4.98), the generated signals at E_1, E_2, E_t, and E_d are graphically depicted and analyzed. For this reason, the input signal of 5 W dark soliton is launched into the system at the input port, E_{in}. Gaussian beam with 2 W input power is then injected towards the system through the add port, E_{add}. 30 μm ring radius of the microring resonator is used for the simulation purpose. In order to optimizing the output signal, the radii of the ring are simulated in range of 20–40 μm respectively.

The coupling coefficient of resonators is a dimensionless value which characterizes the interaction of two resonators. Coupling coefficients are used in resonator filter theory. The resonators may be either electromagnetic or acoustic, or both electromagnetic and acoustic. In this research, the values of coupling coefficients, κ_1 and κ_2 vary from 0 to 1 respectively. At the point where $\kappa = 0$, there is no light entering the system, while 100 % of light from the source entering the system at the point where $\kappa = 1$ (Figs. 4.3 and 4.4).

Based on the practical device values, the value of refractive index, n_o of the optical fibre is set to be $n_o = 3.34$, while the effective cross sectional area, A_{eff} is set at $A_{eff} = 0.5\ \mu m^2$. The 1550 nm single-mode fibre waveguide is used. The waveguide wave coefficient, α and the insertion loss coefficients, γ are set to be

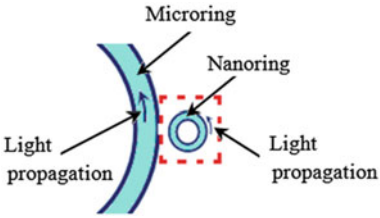

Fig. 4.3 Right nanoring

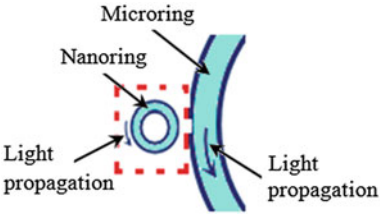

Fig. 4.4 Left nanoring

$\alpha = 0.05$ dBkm^{-1} and $\gamma = 0.1$ respectively. All these parameter values are imported to the MatLab programming software and simulated based on the expressions in (4.95)–(4.98) respectively. All the simulated results are analyzed and discussed in details.

Figure 4.5 shows the flow chat of the simulation and modelling process for the add-drop configuration system. The expression of input signal, control signal, circulating field E_1, circulating field E_2, output signal at throughput port, E_t and drop port, E_d are computed to the MatLab programming software. All the parameters used in the add-drop system are input to the programming software. For this configuration system, a few parameters are varies, that are the ring radius, R and the coupling coefficients, κ_1 and κ_2. All the characteristics of the signals output from the system will be discussed in details.

4.4.2 PANDA Ring Resonator System Modelling

The schematic diagram of PANDA ring resonator system is depicted in Fig. 4.2. The circulating fields are assigned at four different points, marked with E_1, E_2, E_3, and E_4 respectively.
The expressions for all circulating fields are given as:

$$E_1 = \frac{jx_1\sqrt{\kappa_1}E_{in} + jx_1x_2y_1\sqrt{\kappa_2}E_L E_{add}\exp\left(\frac{\phi}{2}\right)}{1 - x_1x_2y_1y_2E_L E_R\exp(\phi)} \tag{4.101}$$

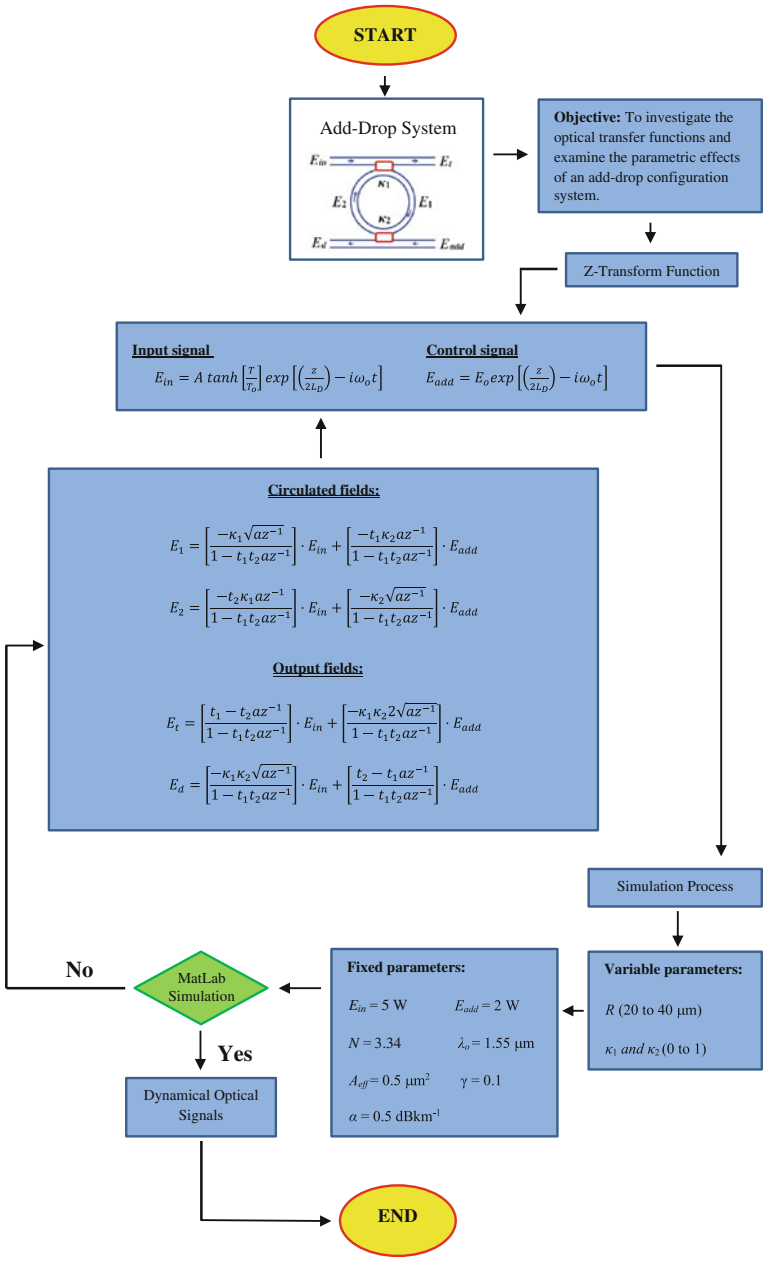

Fig. 4.5 Flow chart of simulation/modelling process for add-drop configuration system

$$E_2 = \frac{jx_1\sqrt{\kappa_1}E_R E_{in}\exp\left(\frac{\phi}{2}\right) + jx_1x_2y_1\sqrt{\kappa_2}E_L E_R E_{add}\exp(\phi)}{1 - x_1x_2y_1y_2E_L E_R\exp(\phi)} \tag{4.102}$$

$$E_3 = \frac{jx_2\sqrt{\kappa_2}E_{add} + jx_1x_2y_2\sqrt{\kappa_1}E_R E_{in}\exp\left(\frac{\phi}{2}\right)}{1 - x_1x_2y_1y_2E_L E_R\exp(\phi)} \tag{4.103}$$

$$E_4 = \frac{jx_2\sqrt{\kappa_2}E_L E_{add}\exp\left(\frac{\phi}{2}\right) + jx_1x_2y_2\sqrt{\kappa_1}E_L E_R E_{in}\exp(\phi)}{1 - x_1x_2y_1y_2E_L E_R\exp(\phi)} \tag{4.104}$$

From (4.101) to (4.104), the output signals at throughput and drop ports are given as:

$$E_t = \frac{x_1y_1E_{in} - x_1x_2\sqrt{\kappa_1}\sqrt{\kappa_2}E_L E_{add}\exp\left(\frac{\phi}{2}\right) - x_1^2x_2y_2E_L E_R E_{in}\exp(\phi)}{1 - x_1x_2y_1y_2E_L E_R\exp(\phi)} \tag{4.105}$$

and

$$E_d = \frac{x_2y_2E_{add} - x_1x_2\sqrt{\kappa_1}\sqrt{\kappa_2}E_R E_{in}\exp\left(\frac{\phi}{2}\right) - x_1x_2^2y_1E_L E_R E_{add}\exp(\phi)}{1 - x_1x_2y_1y_2E_L E_R\exp(\phi)} \tag{4.106}$$

As discussed previously, the input and control signals magnitudes influence the characteristics of the output signals. During the simulation process for this part, dark soliton is chosen as the input signal, E_{in} and Gaussian beam as the control signal, E_{add}.

In this research, the circulating fields, E_1, E_2, E_3, E_4 and both throughput and drop ports, E_t and E_d are simulated based on the (4.101)–(4.106) that have been derived earlier. Some key parameters are varied and output signals are recorded and analyzed. During the simulation process, numbers of key parameters are optimized in order to achieve the best output signals from the system, either at throughput or drop ports.

The input and control signals launched into the system are similar to the signals obtained for the add-drop system. For the purpose, 5 W dark soliton input signal is launched at the input port, E_{in} and controlled by 2 W Gaussian beam is injected through the add port, E_{add}. The radius of main ring, R is set at 30 μm while the radii of the right and left nanorings, R_R and R_L are varied from 40 to 90 nm respectively. The best values of R, R_R, and R_L are determined and discussed. All the values of coupling coefficients, κ_1, κ_2, κ_3, and κ_4 are set to vary from 0 to 1 respectively.

Based on the practical device values, the value of refractive index, n of the optical fibre is set to be $n = 3.34$, while the effective cross sectional area, A_{eff} is set at $A_{eff} = 0.5\ \mu m^2$. The 1550 nm fibre waveguide is used. The waveguide wave coefficient, α and the insertion loss coefficient, γ are set to be $\alpha = 0.05\ dBkm^{-1}$ and

$\gamma = 0.1$ respectively. All these parameter values are imported to the MatLab programming software and simulated based on the expression in (4.101)–(4.106) respectively. All the simulated results are analyzed and discussed in details.

Figure 4.6 shows the flow chat of the simulation and modelling process for the PANDA ring resonator system. The expression of input signal, control signal, circulating field E_1, circulating field E_2, circulating field E_3, circulating field E_4, output signal at throughput port, E_t and drop port, E_d are computed to the MatLab programming software. All the parameters used in the add-drop system are input to the programming software. For this configuration system, a few parameters are varies, that are the ring radii (R, R_R, and R_L) and the coupling coefficients (κ_1, κ_2, κ_3, and κ_4). The effect of the input power towards the performance of the PANDA system is also investigated. All the characteristics of the signals output from the system will be discussed in details.

4.5 Applications of the PANDA System for Photodetector Technology

To increase the device performance, the used of trapping and accelerating particles with optical tweezers is recommended. The performance of the device can be increased and controlled using the PANDA microring resonator system. In manipulation, PANDA system may generate the optical tweezers for trapping electrons/atoms to the terminal contact. By this technique, electrons/atoms can be driven to the contacts without regarding to generate defects. Moreover, the use of PANDA system also found in many applications such as photonics microdevice (Sumetsky et al. 2002), hybrid transistor (Suwanpayak 2011), therapeutic (Aziz et al. 2012), and telecommunication network (Yupapin 2010). The trapping tools generator is reviewed and the new design for the particle accelerator is described. The simulation results using MatLab programming software are demonstrated.

By using dark-bright solitons pulse propagating within PANDA ring resonator system, the trapping tools can be formed and used to trap the molecules/atoms from the system. In this study, the multiplexed signals with slightly difference wavelengths of the dark soliton are controlled and amplified within the system. The dynamical behaviour of dark-bright solitons interaction are also analyzed and described accordingly.

Generally, the photodetector performance depends on the number of electrons that can move from the diode depletion layer to the contacts under the drift velocity, which cannot be controlled. In this study, the generated optical tweezers can be controlled by using PANDA ring resonator system. The optical tweezers can be designed and generated for electron trapping in the device. The required electrons can be trapped and injected to the contact without loss, and the transport time to the contacts can also be controlled. The optical tweezers sizes can be varied and

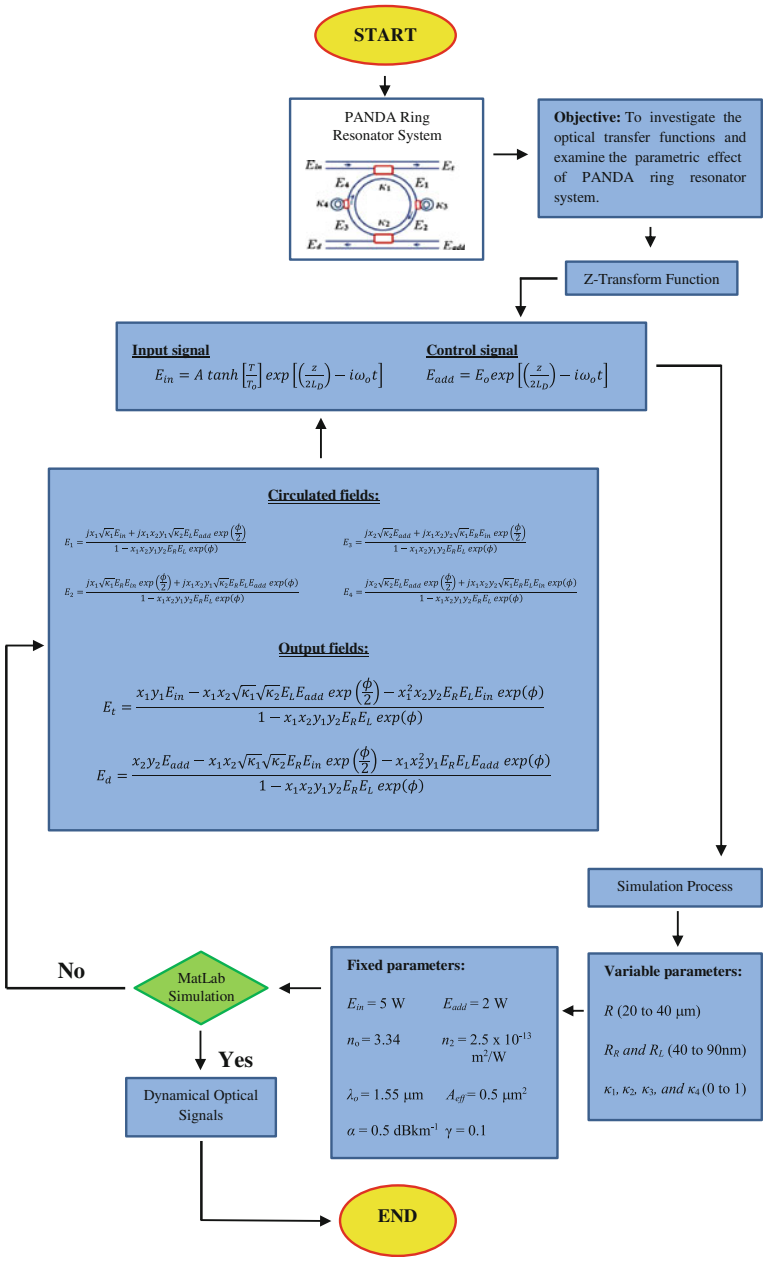

Fig. 4.6 Flow chart of simulation/modelling process for PANDA ring resonator system

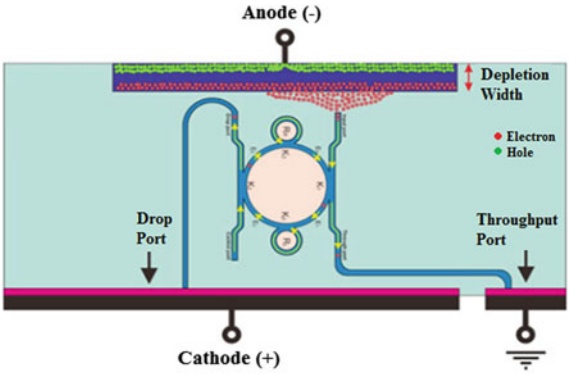

Fig. 4.7 Optical tweezers model for electron trapping

selected for suitable electron trapping by controlling the PANDA ring resonator input signals. Figure 4.7 shows the optical tweezers model for electron trapping, in which the trap size can be adjusted and tuned.

By using the proposed system designed, the optical waveguide can be used to trap the electrons/atoms. The photodetector device can be constructed incorporating with the optical tweezers assembly. The trapped electrons can transfer from anode to cathode contacts via the optical waveguide. In the simulation process, the input signals choose are dark soliton and Gaussian beam at the peak power of 100 mW respectively. The ring radii are set at $R = 20$ μm and $R_R = R_L = 5$ μm. The coupling coefficients of the PANDA ring resonator are set to be $\kappa_1 = \kappa_2 = \kappa_3 = \kappa_4 = 0.5$. The effective core area, A_{eff} is set at $A_{eff} = 300$ μm^2. The waveguide loss coefficient, α and coupling loss, γ are set at $\alpha = 0.1$ dBkm^{-1} and $\gamma = 0.01$ respectively. The dimensions of the optical tweezers are controlled by various tweezers size, ranging from 100 to 250 μm respectively.

Chapter 5
Results and Discussion

5.1 Introduction

In this chapter, the simulation results of the add-drop and PANDA ring configuration systems are discussed in details. The contributions of both linear and nonlinear effect towards the systems are explained accordingly. The profile results generation using dark soliton input pulse and Gaussian beam control signal are demonstrated. The ring radii and the coupling coefficient parameters are optimized for the purposes. The relationship between the input and output power at throughput and drop ports are studied. All the numerical solution and simulation processes are performed using MatLab programming software.

5.2 Add-Drop Configuration System

Add-drop configuration system consists of a microring resonator and two bus waveguides connected at the top and bottom sides of the ring as depicted in Fig. 4.1 in Chap. 4. The add-drop system is very important especially for filtering and cancelling the chaotic signals, which is very important and useful especially for the communication and security technologies. In this study, the behaviour of the output signals of the system are examined based on the actual practical device parameter values. The proposed system is simulated and the output signals at both throughput and drop ports of the system are investigated.

For the add-drop configuration system set-up, dark soliton with 5 W input power is launched into the system through the input port, E_{in}. At the same time, Gaussian beam with 2 W input power is injected into the system through the add port, E_{add}. The simulation results for circulating fields, E_1 and E_2 and the output fields at throughput and drop ports, E_t and E_d are examined. The characteristics of the output signals of the system are discussed in details.

S. Daud et al., *Simulation of Optical Soliton Control in Micro- and Nanoring Resonator Systems*, SpringerBriefs in Physics, DOI 10.1007/978-3-319-15485-5_5

In operation, 30 μm ring resonator radius is used for the purposed configuration. The effective cross sectional area, A_{eff} is set at $A_{eff} = 0.5\ \mu m^2$. By using InGaAsP/InP fibre waveguide, the refractive index of the fibre is set at $n_o = 3.34$. The waveguide wave coefficient, α and the intensity insertion loss coefficient, γ of the coupler are set as $\alpha = 0.05\ \text{dB km}^{-1}$ and $\gamma = 0.1$ respectively. As per depicted in the schematic diagram shown in Fig. 4.1, there are two fibre couplers connected at the top and bottom of the ring resonator, marked with κ_1 and κ_2 respectively. These couplers are used as the device to control the percentage of light entering the system from E_{in} and E_{add}. The coupling coefficients, κ_1 and κ_2 are set at $\kappa_1 = 0.55$ and $\kappa_2 = 0.35$ respectively.

The results of the interaction between dark soliton and Gaussian beam within the add-drop configuration system are shown in Fig. 5.1. Figure 5.1a–d are the optical signals generated at E_1, E_2, E_t, and E_d respectively. At the circulating points E_1 and E_2, the signals are tuned in the ring resonator due to resonance. The circulating process within the ring result the output signals of the system. A single signal is displayed at the output system, either at throughput or drop ports. The signals filtering and cancelling process of the add-drop system results the single signal as the outputs.

Those input and control signals are continuous to propagate into the system and cause the optical collision between both signals within ring waveguides. Results show that they are different in amplitudes numbers for the power output at the regions E_1 and E_2. For the output signals at E_t and E_d, the highest point are recorded at 2.448 and 1.678 W respectively.

5.3 Ring Radius of Add-Drop System

Ring radius is one of the important parameter that needs to be considered in this research. By using the suitable value of ring radius, the output signals can be optimized accordingly. As the wave propagate within the system acquires phase shift as it travels along the radius of curvature of the ring, the relative phase of the travelling wave determines whether the light interfere constructively or destructively with the input signals. This phenomenon directly influenced the output signal of the system.

During simulation process, 5 W input dark soliton and 2 W Gaussian beam are fed into the system through the input and add ports respectively. The coupling coefficients of the system are set at $\kappa_1 = 0.55$ and $\kappa_2 = 0.35$ respectively. To examine the most suitable values of ring radius, all the other parameters are fixed at constant values. The ring radius of the system is varied from 30 to 36 μm. The impact of the ring radius towards the system are presented in Fig. 5.2, where figures (a–d) show the circulating fields E_1 and E_2, throughput, and drop ports respectively.

Figure 5.2 illustrates the output signals of the add-drop system with different size of the ring radius. The green, black, blue, and red colours represent the ring radius

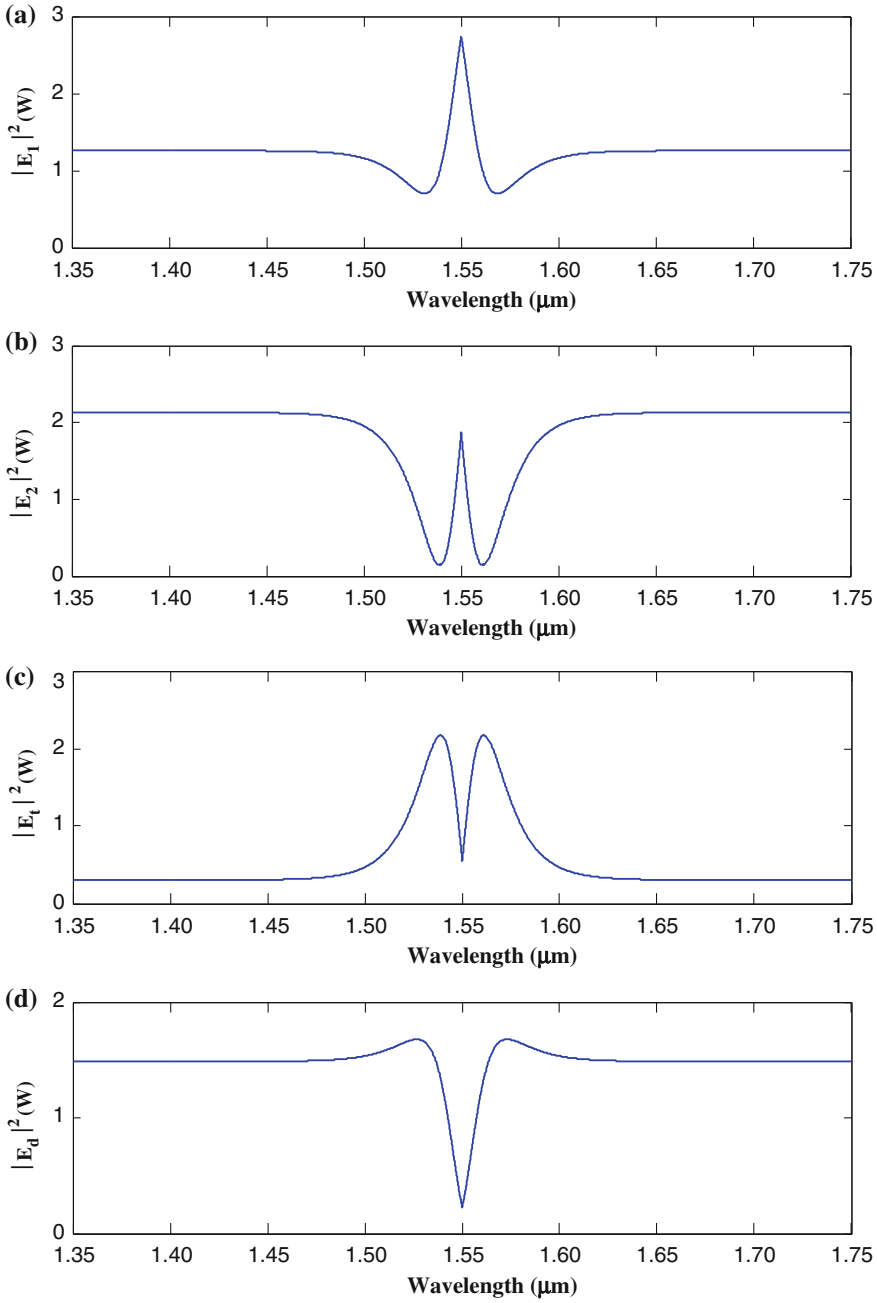

Fig. 5.1 Simulation results of the add-drop configuration system at **a** circulating field E_1, **b** circulating field E_2, **c** throughput port, and **d** drop port

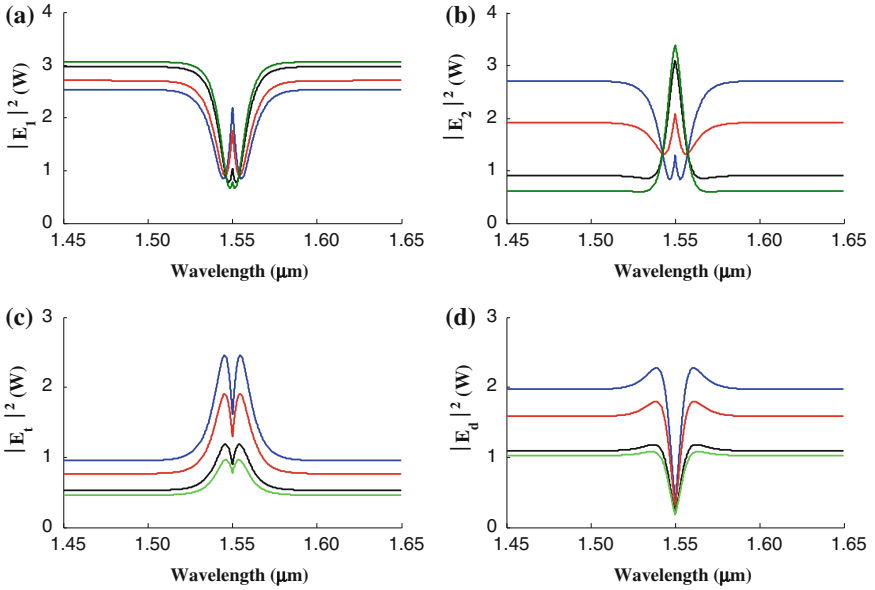

Fig. 5.2 Output signals of the add-drop system for different ring radii at **a** E_1, **b** E_2, **c** throughput port, and **d** drop port

of 30, 32, 34, and 36 μm respectively. From Fig. 5.2, the values of E_t and E_d increases with increase in R size at $R = 30$, 32, and 34 μm respectively. At the point where $R = 36$ μm, the values of E_t and E_d are decreased. Based on the simulation results obtained, the highest peak power of E_t and E_d are recorded at 2.454 and 2.168 W respectively, corresponding to the operating system with ring radius, $R = 34$ μm. For the other values of ring radii, the output powers are significantly dropped. From the obtained data, it can be conclude that the best value for the ring radius of the system is at $R = 34$ μm.

5.4 Coupling Coefficient of Add-Drop System

As discussed in previous section, the suitable value of ring radius, R is very important for optimizing the output signals of the system. The rate of light emits the system and resonance within the ring also contributes towards the generated output signals. The rate of light entering the system is controlled by the coupling coefficient, κ. For add-drop system, there are two coupling coefficients attached on it, one at the top and another one at the bottom of the microring. These coupling coefficients are marked with κ_1 and κ_2 respectively, as depicted in schematic diagram shown in Fig. 4.1.

5.4.1 Variation of κ_1 Towards Add-Drop System

In simulation, fibre waveguide with the cross sectional area, $A_{eff} = 0.5\ \mu m^2$ is used. The optical light source of 5 W dark soliton and 2 W control Gaussian beam are injected towards the system through the input and add ports respectively. InGaAsP/InP fibre with $n_o = 3.34$ is used as waveguide. The attenuation coefficient, α and intensity insertion loss coefficient of the coupler, γ are set at $\alpha = 0.05\,\text{dB km}^{-1}$ and $\gamma = 0.1$ respectively.

For this configuration system, the values of κ_1 are varied from 0.45 to 0.65, while the value of κ_2 is kept constant at $\kappa_2 = 0.35$. Figure 5.3a–d show the output signals at E_1, E_2, throughput, and drop ports respectively. The blue, red, and green signals represent the values of κ_1 for $\kappa_1 = 0.45$, 0.55, and 0.65 respectively. From the signals generated as depicted in Fig. 5.3, the values of E_t and E_d are increases with increase in κ_1 values.

Higher value of the first coupling coefficient, κ_1 results the higher output power of the system, either at throughput or drop ports. This shows the agreement with the roles of coupling coefficient, κ. The higher value of κ_1 indicates that the big portion of light entering the system from E_{in}. Means, more collision between the input and control signals happened within the system.

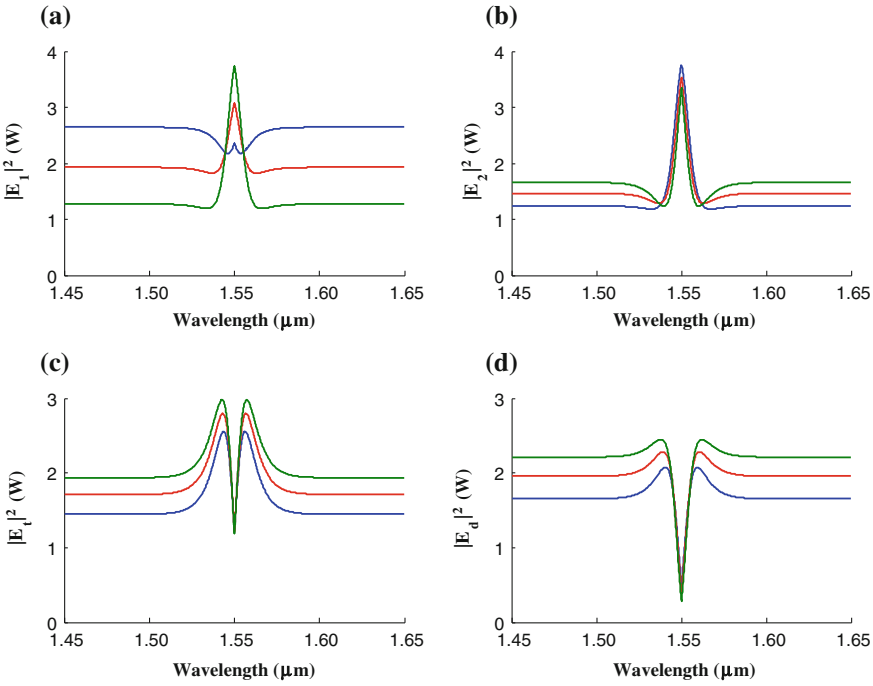

Fig. 5.3 Output signals of the add-drop system with vary of κ_1 values at **a** E_1, **b** E_2, **c** throughput port, and **d** drop port

Table 5.1 Values of output power for the add-drop system with varying of κ_1

κ_1	κ_2	Output power (±0.001 W)	
		Throughput port, E_t	Drop port, E_d
0.10	0.35	2.443	1.382
0.20	0.35	2.596	1.487
0.30	0.35	2.768	1.582
0.40	0.35	2.922	1.674
0.50	0.35	3.072	1.791
0.60	0.35	3.229	1.884
0.70	0.35	3.371	1.976
0.80	0.35	3.503	2.073
0.90	0.35	3.647	2.164
1.00	0.35	3.786	2.279

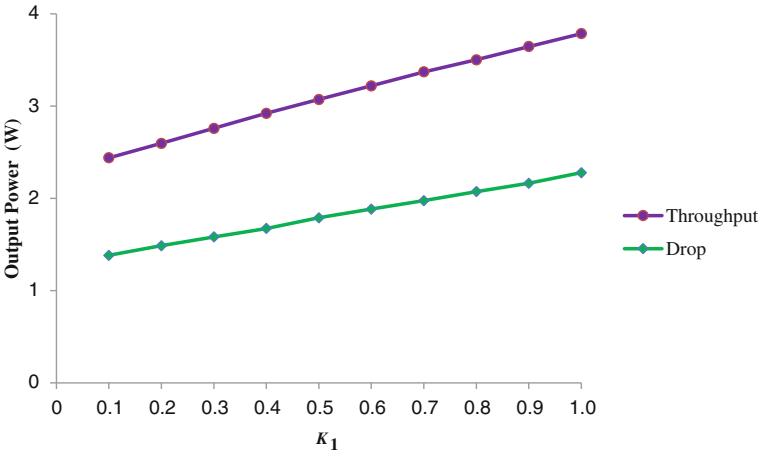

Fig. 5.4 Relationship between the coupling coefficient κ_1 with output power at throughput and drop ports

Table 5.1 shows the values of output power for the add-drop system with varying of κ_1. The value of κ_2 is kept at $\kappa_2 = 0.35$ while the values of κ_1 increase from $\kappa_1 = 0.10$ to 1.00. From the data input in Table 5.1, it is shows that the value of output power at throughput and drop ports are increases significantly with increase of the values of κ_1.

Figure 5.4 shows the graph of κ_1 plotted against output power at throughput and drop ports with the constant value of κ_2. From the graph plotted, it is observed that the output power of the system is directly proportional to the values of κ_1. The gradient of the graph is measured to be 1.58 W for the throughput port and 1.02 W for the drop port respectively. As for conclusion, for the higher value of κ_1, higher output power is generated at the throughput and drop ports of the add-drop system.

5.4.2 Variation of κ_2 Towards Add-Drop System

The values of coupling coefficients are very important for optimization of the performance of the system. From the results simulated in previous section, the values of output power increases with increase of κ_1. For this section, all the parameter values are kept as same as in the previous section, except for the values of κ_1 and κ_2. During simulation, the value of κ_1 is fix at $\kappa_1 = 0.75$ while the values of κ_2 are varies from 0.65 to 0.85.

Figure 5.5 shows the simulation results of the add-drop system with varying of κ_2 values. The blue, red, and green colours of the signals represents the values of κ_2 for $\kappa_2 = 0.65$, 0.75, and 0.85 respectively. All the signals at the circulating fields E_1, E_2, throughput, and drop ports are shown in Fig. 5.5a–d respectively.

From the signals generated as shown in Fig. 5.5, it is observed that the amplitudes of output power at throughput and drop ports increase with the increases in κ_2. The higher value of κ_2 indicates that the big portion of light entering the system from E_{add}. When the light entering the system at add port increase, more collision between the input and control signals happened within the system. This led to the increasing of the output power of the system.

Table 5.2 shows the values of output power for the add-drop system with varying of κ_2. The value of κ_1 is kept at $\kappa_1 = 0.75$ while the values of κ_2 increase

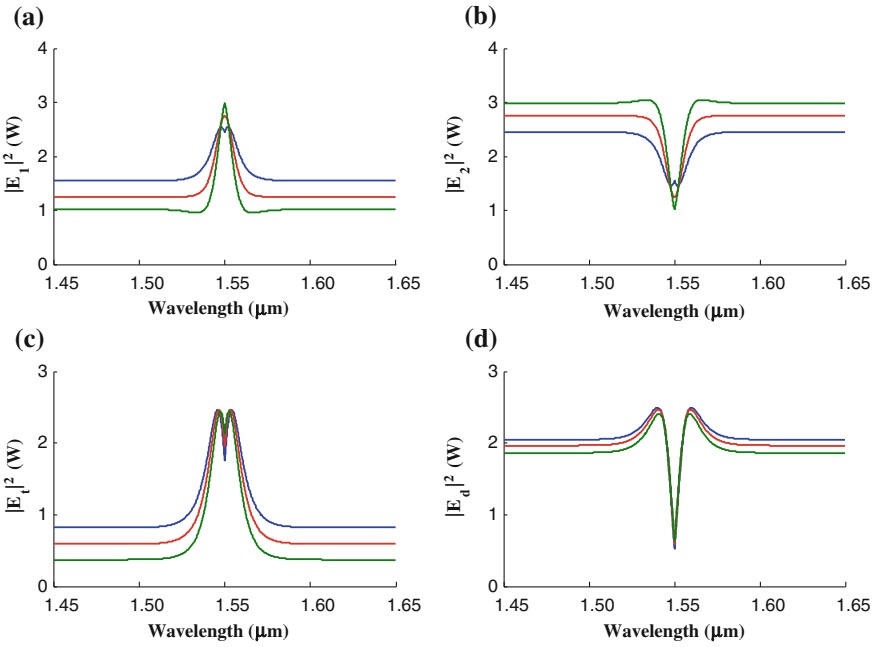

Fig. 5.5 Output signals of the add-drop system with vary of κ_2 values at **a** E_1, **b** E_2, **c** throughput port, and **d** drop port

Table 5.2 Values of output power for the add-drop system with varying of κ_2

κ_1	κ_2	Output power (±0.001 W)	
		Throughput port, E_t	Drop port, E_d
0.75	0.10	2.448	2.265
0.75	0.20	2.633	2.453
0.75	0.30	2.827	2.641
0.75	0.40	3.021	2.821
0.75	0.50	3.204	2.985
0.75	0.60	3.362	3.121
0.75	0.70	3.479	3.216
0.75	0.80	3.533	3.250
0.75	0.90	3.482	3.182
0.75	1.00	3.166	2.707

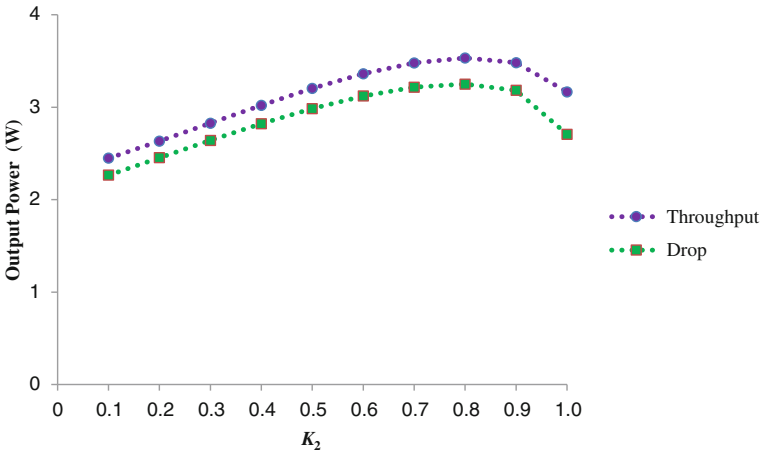

Fig. 5.6 Relationship between coupling coefficient κ_2 with output power at throughput and drop ports

from $\kappa_2 = 0.10$ to 1.00. Table 5.2 shows the data taken from the simulation process. It is shown that the value of output power at throughput and drop ports are increase with increases of the values of κ_2 until the point where $\kappa_2 = 0.80$. At the point where $\kappa_2 = 0.80$ and higher, it is shows the decreasing of the output power.

From the data computed in Table 5.2, Fig. 5.6 is plotted. Graph plotted in Fig. 5.6 shows the relationship between the coupling coefficient κ_2 with the output power at throughput and drop ports respectively. From the graph plotted, it is seen that the values of output power increase with increase in κ_2 until the point where $\kappa_2 = 0.80$. At the point where κ_2 is higher than 0.80, the power output of the system is significantly dropped as shown in the graph plotted in Fig. 5.6. This shows that the system is achieved the maximum resonance with the input light and the control signal beam at the point where $\kappa_2 = 0.80$.

The maximum resonance can be achieved when the phase is in multiple of 2π as discussed in Sect. 3.5.3 in Chap. 3. The system is said to achieved the maximum resonance at the point where $\kappa_1 = 0.75$ and $\kappa_2 = 0.80$ respectively.

5.5 Optimization of Add-Drop Configuration System

The dynamical behaviour of the optical signals of add-drop configuration system is demonstrated and discussed. The tunability of such signals can be obtained by varying and controlling the key parameters on the system. For convenience analysis, the circulated fields within the ring are presented by E_1 and E_2 while the output fields at throughput and drop ports of the system are depicted by E_t and E_d respectively. The key parameters are tuned and vary in order to optimize the output signals generated from the system.

For the purpose, 5 W input dark soliton with 50 ns pulse width is launched into the system through the input port, E_{in} and 2 W Gaussian beam is injected towards the system via the add port, E_{add}. The fibre waveguide at center wavelength, $\lambda_o = 1550$ nm is used for the purposed. The effective core area of the system is fixed at $A_{eff} = 0.5\ \mu m^2$. The attenuation coefficient, α is fixed at $\alpha = 0.05\ dB\ km^{-1}$ and the intensity insertion loss coefficient of the coupler, γ is set at $\gamma = 0.1$ respectively. For instance, the center ring radius is chosen at $R = 34\ \mu m$. The coupling coefficient values are set at $\kappa_1 = 0.75$ and $\kappa_2 = 0.80$. Figure 5.7a–f represent the input dark soliton, Gaussian beam, E_1 field, E_2 field, throughput port, and drop port respectively. The values of throughput and drop ports for the optimized system are calculated at $E_t = 3.784$ W and $E_d = 2.893$ W as shown in Fig. 5.7.

5.6 PANDA Ring Resonator System

PANDA ring resonator system as depicted in Fig. 4.2 in Chap. 4 is proposed and simulated using MatLab R2010b programming software. The system is constructed by a series of nonlinear micro- and nanoring resonators integrated with two bus waveguides to form a beneficial system especially in physics and biological technologies. The ring resonator waveguide system is assumed to exhibit Kerr nonlinearity.

The refractive index of the waveguide is given by $n = n_0 + n_2 I$ where n_o and n_2 are the linear and nonlinear refractive indexes of the fibre respectively. The behaviour of the optical signals passing through the system is simulated and analyzed accordingly. Both signals generated at throughput and drop ports of the system are analyzed and discussed in details. The behaviour of the simulated signals at E_1, E_2, E_3, and E_4 are also presented.

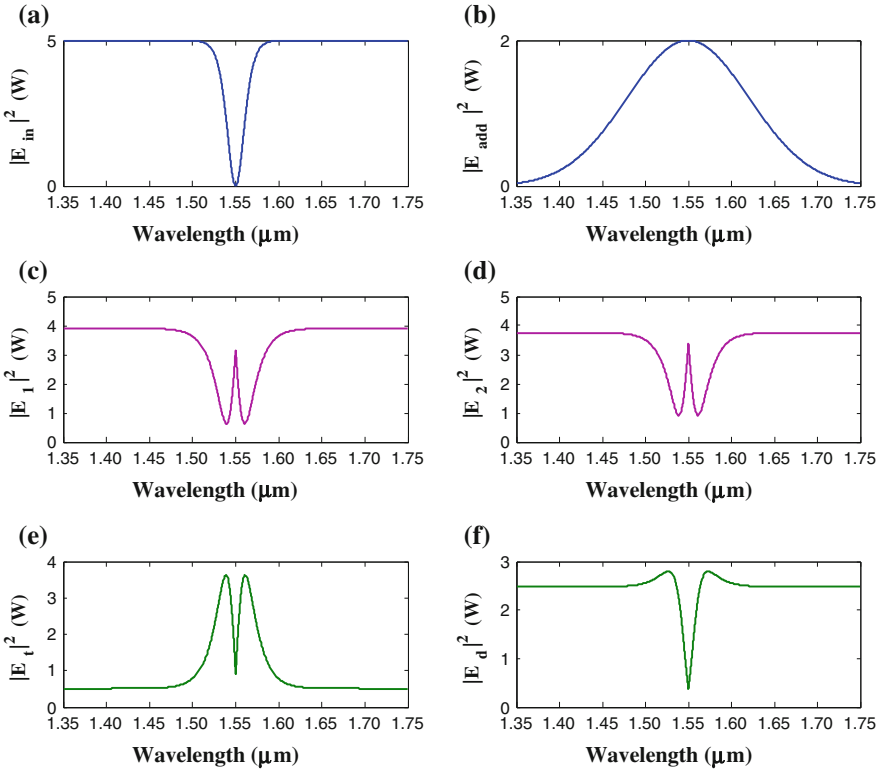

Fig. 5.7 Optimized signals for add-drop configuration system where **a** dark soliton, **b** Gaussian beam, **c** and **d** circulating fields E_1 and E_2, **e** throughput port, and **f** drop port

In order to associate the system with the practical device, the parameter values are selected to have the values as per real devices. The fibre waveguide of InGaAsP/InP with center wavelength, $\lambda_0 = 1550$ nm is selected. The linear and nonlinear refractive indexes of InGaAsP/InP fibre waveguide are $n_o = 3.34$ and $n_2 = 2.5 \times 10^{-13}$ m^2 W^{-1} respectively. The effective cross sectional area, A_{eff} of the waveguide used are in the range of 0.2 nm^2–0.5 μm^2 respectively. The waveguide wave coefficient, α is fixed at $\alpha = 0.05$ dB km^{-1} and the intensity insertion loss coefficient of the coupler, γ is set at $\gamma = 0.1$.

For simulation process of the PANDA system, dark soliton with 5 W input power and 50 ns pulse width is launched into the system through the input port, E_{in}. As for control signal, the Gaussian beam with 2 W input power is injected through the add port, E_{add}. For operation, the center ring, R is chosen to be $R = 30$ μm, while the right and left nanoring are set at $R_R = R_L = 40$ nm. The coupling coefficients between the center ring to the bus waveguides at κ_1 and κ_2 are set at $\kappa_1 = 0.65$ and $\kappa_2 = 0.40$ respectively. Both the coupling coefficients within the center microring to the right and left nanorings, κ_3 and κ_4 are set at $\kappa_3 = \kappa_4 = 0.20$.

Figure 5.8 shows the simulation results of the interaction between input dark soliton with the Gaussian beam as the control signal. Both input and control signals with centre wavelength of $\lambda_o = 1550$ nm are injected into the system through input port, E_{in} and add port, E_{add} respectively. Figure 5.8a–d shows the dynamical interaction between the input signals at four different circulation fields in the system, namely as E_1, E_2, E_3, and E_4 respectively. These signals are the results of the optical collision between input and control signals within the ring waveguide.

From the generated signals as shown in Fig. 5.8a–d, it is observed that the interactions are generated at different amplitudes level. The destruction happens at E_2 and leads to the decrement of peak power in circulating signals. The output signals at throughput and drop ports of the system are generated in forms of optical potential well. The highest output signal generated at throughput port, E_t is measured at 20.42 and 10.97 W at the drop port, E_d as shown in Fig. 5.8e, f respectively. It is shown that the potential well is formed at the gap between two intensities, which provides the trapping force in the system. The system produces the output fields in forms of chaotic signals.

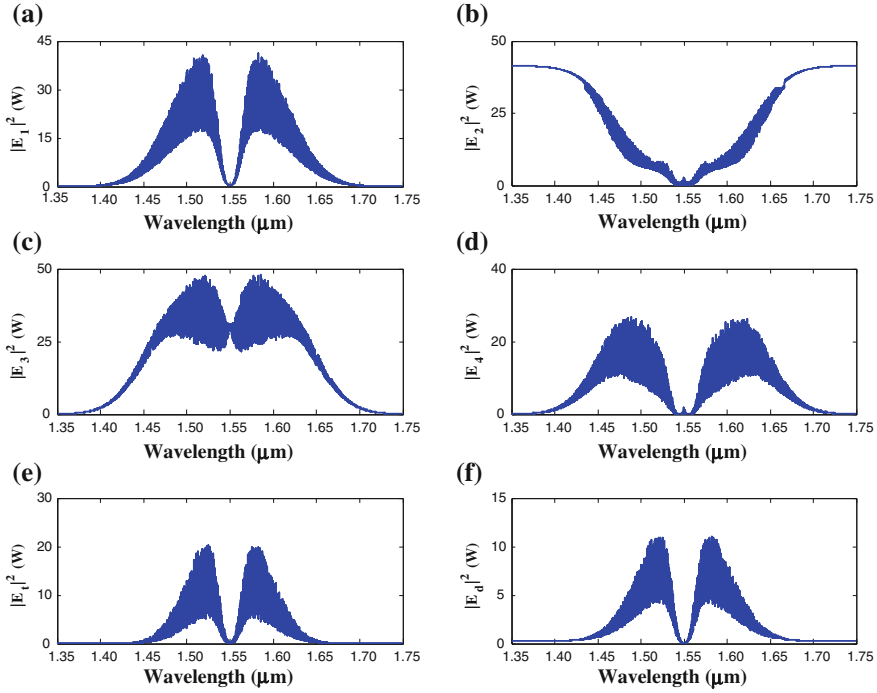

Fig. 5.8 Optical signals generated by PANDA ring resonator system where **a–d** are circulated fields at E_1, E_2, E_3, and E_4, **e** throughput port, and **f** drop port

5.7 Ring Radii of PANDA System

The size or radius of the ring greatly affects the characteristics of the circulating fields as well as the output signals of the system due to phase shift in propagating wave within the resonator along the curvature of the system. To determine the light interferes constructively or destructively with the input signals, the combination of the signals injected toward the system can be seen at certain points. This process directly influences the output signals at throughput and drop ports of the system. In this study, the Kerr nonlinearity is considered. The contributions from linear and nonlinear phase shift are taken into the account.

5.7.1 Center Ring Radius

Dark soliton with 5 W input power is fed into the system through the input port, E_{in}. At the same time, 2 W Gaussian beam is injected into the system through the add port, E_{add}. The coupling coefficient values of the system are set at $\kappa_1 = 0.65$, $\kappa_2 = 0.40$, and $\kappa_3 = \kappa_4 = 0.20$ respectively. The InGaAsP/InP fibre with $\lambda_o =$ 1550 nm is used as the waveguide. The linear and nonlinear refractive indexes of the fibre are set at $n_o = 3.34$ and $n_2 = 2.5 \times 10^{-13}$ $\mathrm{m^2\,W^{-1}}$ respectively. The effective core area of the ring is fixed at $A_{eff} = 0.5$ $\mu\mathrm{m}^2$. The attenuation coefficient, α is fixed at $\alpha = 0.05\,\mathrm{dB\,km^{-1}}$ and the intensity insertion loss coefficient of the coupler, γ is set at $\gamma = 0.1$. The radii of both right and left nanorings are set at $R_R = R_L = 40$ nm respectively. Based on the practical device values, the radius of the center microring, R is varied in range of 28–36 μm. The simulation results obtained from PANDA system at throughput and drop ports are presented in Fig. 5.9a, b respectively.

Figure 5.9a, b illustrates the output signals generated at throughput and drop ports of the system respectively. The radii of the center ring of PANDA system are set at 28, 30, 32, 34, and 36 μm. As shown in the Fig. 5.9, the shape and peak power of the generated signals are different for each ring size used. The highest pick power at E_t and E_d were recorded at 31.36 and 16.87 W respectively. These maximum values are recorded at the point where $R = 34$ μm. For other values of R, the output power are recorded with the lower values as compared to the value obtained at $R = 34$ μm for both throughput or drop ports.

The highest transmission of the output signals can be described by the resonance states from the interaction between the lights entering the system and the ring itself. The ring resonator which is under resonance condition has the highest ratio between the circulating power to the input power which can possibly achieved in the practical device system.

In nonlinear Kerr medium, the relative phase shift experienced by the travelling wave at certain points on the system depends on a few parameters such as input power, nonlinear refractive index, effective core area, circumference length of the

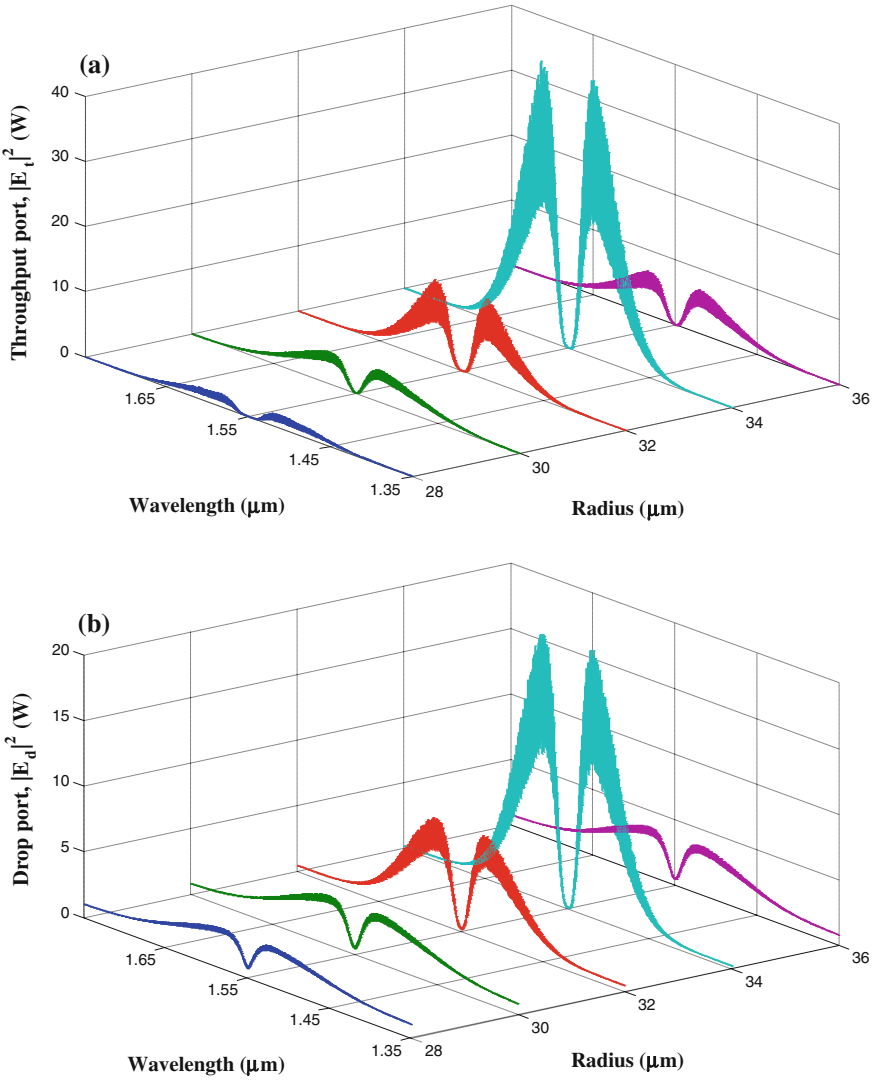

Fig. 5.9 Optical signals generated at **a** throughput port and **b** drop port where center radius, R varied from 28 to 36 μm

ring, waveguide loss coefficient, and the insertion loss coefficient of the system. In this case, the ring radius is chosen to satisfy the integral multiple of 2π phase shift while the other parameters are kept constant. During the process, the travelling waves in the ring waveguide interfere constructively with the input signal. The propagating wave interferes constructively within the system when the interactive light acquires phase shift multiple of 2π as it completes one full roundtrip.

The phase shift of one complete roundtrip of the PANDA system is given as:

$$\phi = \phi_o + \phi_{NL} + \frac{\pi}{2} \tag{5.1}$$

where ϕ_o and ϕ_{NL} are the linear and nonlinear phase shift respectively. ϕ_o and ϕ_{NL} are given as:

$$\phi_o = kLn_o \tag{5.2}$$

and

$$\phi_{NL} = kLn_2I \tag{5.3}$$

In (5.2) and (5.3), k is constant, L is the length of the roundtrip, n_o is the linear refractive index of the fibre, n_2 is the nonlinear refractive index of the fibre, and I is the intensity. The term $\frac{\pi}{2}$ represents the phase shift experienced by the input light signal passing through the coupler.

If the interacting fields with the wavelength is not in resonance condition ($\phi \neq 2\pi$), the circulated fields interferes destructively with the input fields. This lead to the low transmission and drop in output power. The incident light achieve the resonance condition with the ring when $\phi = 2\pi m$, where m is the integer mode number. In this research, the highest output power is achieved at the point where $R = 34$ μm. Hence, it can be concluded that the incident light achieved the maximum resonance with the ring at this point.

5.7.2 Right and Left Nanorings

The radii of right and left nanorings, are important indeed in order to optimize the system performance. By using the same input and control signal values as discussed in Sect. 5.7.1, the variations of R_R and R_L towards the performance of the system are measured and analyzed precisely. The center ring radius is set at $R = 34$ μm. The values of coupling coefficients of the system are kept as per previous section where $\kappa_1 = 0.65$, $\kappa_2 = 0.40$, and $\kappa_3 = \kappa_4 = 0.20$ respectively.

Figure 5.10 shows the output signals generated at throughput and drop ports of the system for the different values of R_R and R_L. For this simulation process, the center ring radius, R is fixed at $R = 34$ μm while the right and left nanorings are varied from 40 to 80 nm. As shown in Fig. 5.10, the variation in R_R and R_L values changed the amplitude signals of the output power, at both throughput, E_t and drop, E_d ports.

The values of output power increases with increase in the nanorings radii until the point where $R_R = R_L = 70$ nm, which shows the higher values of the output power. On the other side, the output power starts to decrease at the point where

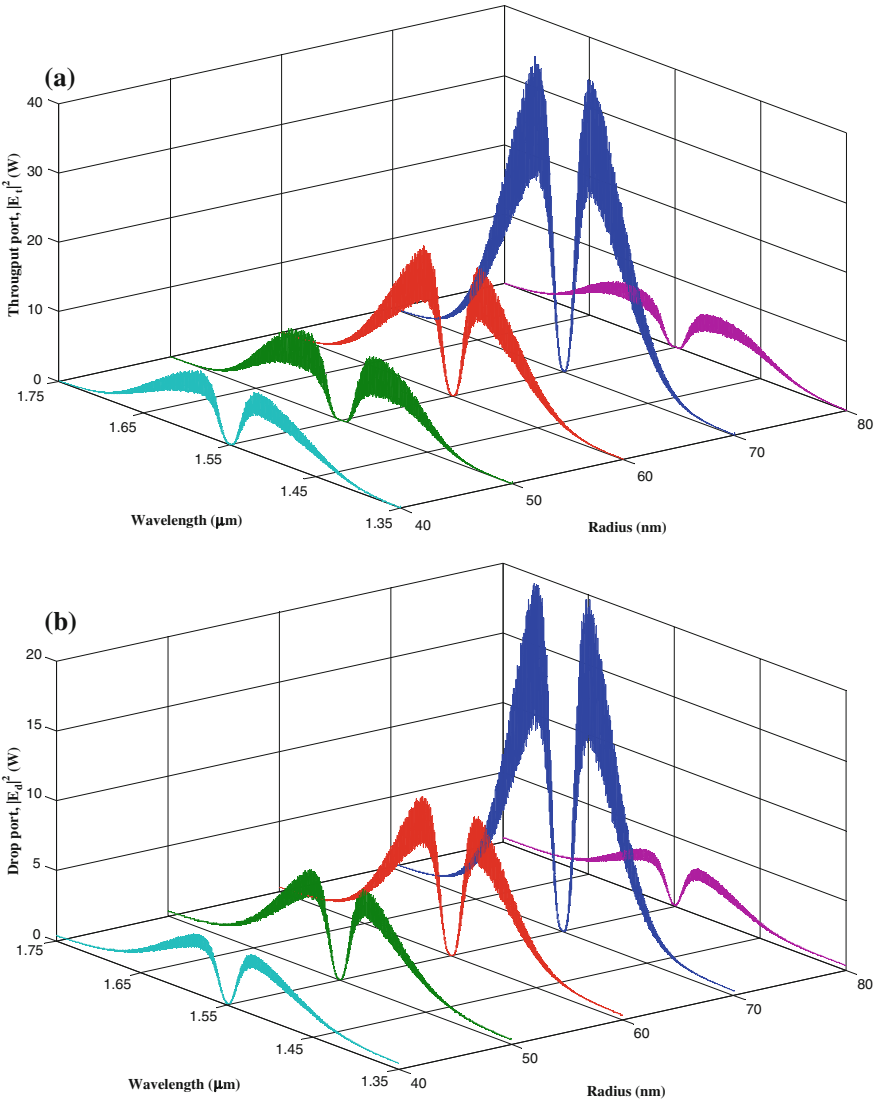

Fig. 5.10 Optical signals generated for different values of R_R and R_L at **a** throughput port and **b** drop port of PANDA system

$(R_R = R_L) > 70$ nm. The highest peak power obtained at throughput and drop ports of the system are recorded at 33.76 and 18.38 W respectively, which corresponds to the values of $R_R = R_L = 70$ nm. Based on Fig. 5.10, the output signal is slightly decreased for other values of R. Thus, the system is said to achieve the maximum resonance at the nano rings radii values of 70 nm.

5.8 Coupling Coefficient of PANDA System

Some important parameters are varied to investigate the dynamical behaviours of the generated optical signals from the PANDA system. As discussed in previous section, the ring radii (R, R_R, and R_L) plays an important role in order to optimizing the system performance. The coupling coefficients (κ_1, κ_2, κ_3, and κ_4) also contribute toward the performance of the system. The coupling parameters for the coupler between the center microring with the bus waveguides (κ_1 and κ_2) and the coupler between the center microring with the right and left nanorings (κ_3 and κ_4) are varied in order to examine the effect coupling coefficients toward the output signals.

5.8.1 Variation of κ_1 and κ_2

In operation, fibre waveguide with the cross sectional area, $A_{eff} = 0.5\ \mu m^2$ at the center microring and $A_{eff} = 0.2\ nm^2$ at right and left nanorings are used. The optical fields of 5 W dark soliton and 2 W control Gaussian beam are injected into the system through the input and add ports respectively. The InGaAsP/InP fibre waveguide with $n_o = 3.34$ and $n_2 = 2.5 \times 10^{-13}\ m^2\ W^{-1}$ is used for the purposed. The attenuation coefficient, α is set at $\alpha = 0.05\ dB\ km^{-1}$ and the intensity insertion loss coefficient of the coupler, γ is set at $\gamma = 0.1$.

The radii of the center microring, right nanoring, and left nanoring are set at $R = 34\ \mu m$, and $R_R = R_L = 70$ nm respectively. The values of coupling coefficients κ_1 and κ_2 are varied in range of 0.1–1. During this simulation process, the values of coupling coefficients κ_3 and κ_4 are kept constant where $\kappa_3 = \kappa_4 = 0.20$. This is done to examine the contribution of coupling coefficients κ_1 and κ_2 toward the system. Dynamical behaviours of the interacting fields of the system are investigated and analyzed accordingly.

Figure 5.11 shows the simulation results of PANDA ring resonator system where κ_1 varies from 0.65 to 0.95 and κ_2 is fixed at $\kappa_2 = 0.40$. Figure 5.11a–d shows the simulated results of the circulated fields at E_1, E_2, E_3, and E_4 respectively. This is corresponds to four different points on the ring waveguide as depicted in Fig. 4.2 in Chap. 4. The output signals at throughput and drop ports of the system are shown in Fig. 5.11e, f respectively.

As the values of κ_1 increase, the output power at throughput port, E_t also increases, while the output power at drop port, E_d decreases. Based on the light transmission theory, when the values of coupling coefficient increase, the portion of input light coupled within the ring also increases. The majority of input fields are coupled into the ring resonator system. Thus, only minor component of input light is transmitted through the first coupler and vice versa. With the constant value of κ_2, the throughput port is at high transmission region and it leads to the increasing pattern of the output power at throughput port, E_t.

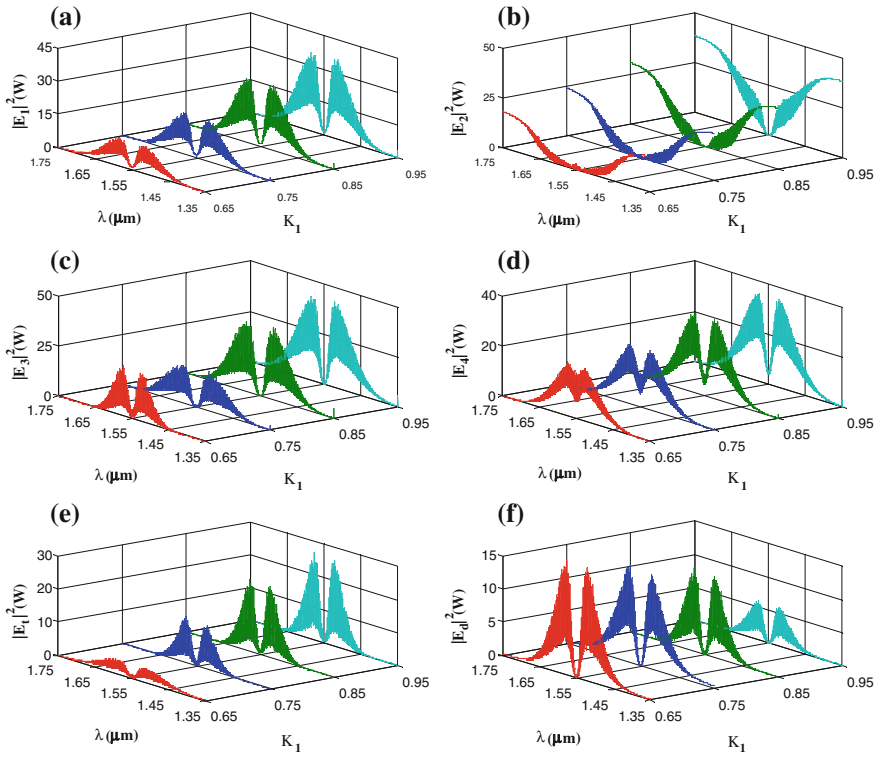

Fig. 5.11 Output signals generated at **a**–**d** circulating fields, **e** throughput port, and **f** drop port of the PANDA system with variable values of κ_1

The same parameters as per previous section are repeated with the constant value of κ_1 and κ_2 is varied. In this case, the value of κ_1 is fixed at $\kappa_1 = 0.85$ and the values of κ_2 are varies from 0.15 to 0.45 respectively. Figure 5.12e, f show the output signals generated at throughput and drop ports of the system for different values of κ_2. As shown in Fig. 5.12, the output power at drop port, E_d increases with increase in κ_2 while the output power at throughput port, E_t decreases with increase in κ_2. This caused a significant enhancement in circulated power within the ring as more fraction of light being coupled into the waveguides. With the increases values of κ_2, the drop port is at high transmission region and it leads to the increasing pattern of the output power at this region.

The relationship between κ_1 and κ_2 with E_t and E_d are presented in 3-dimensional (3-D) graph as shown in Figs. 5.13 and 5.14 respectively. During simulation process, the output power of 5 W dark soliton and 2 W control Gaussian beam are injected toward the system through E_{in} and E_{add} ports respectively. The coupling coefficients, κ_1 and κ_2 are varied from 0 to 1. The value of coupling coefficient, κ determine the rate of light entering the system. Maximum light entering the system when $\kappa = 1$ while no light emit to the system when $\kappa = 0$.

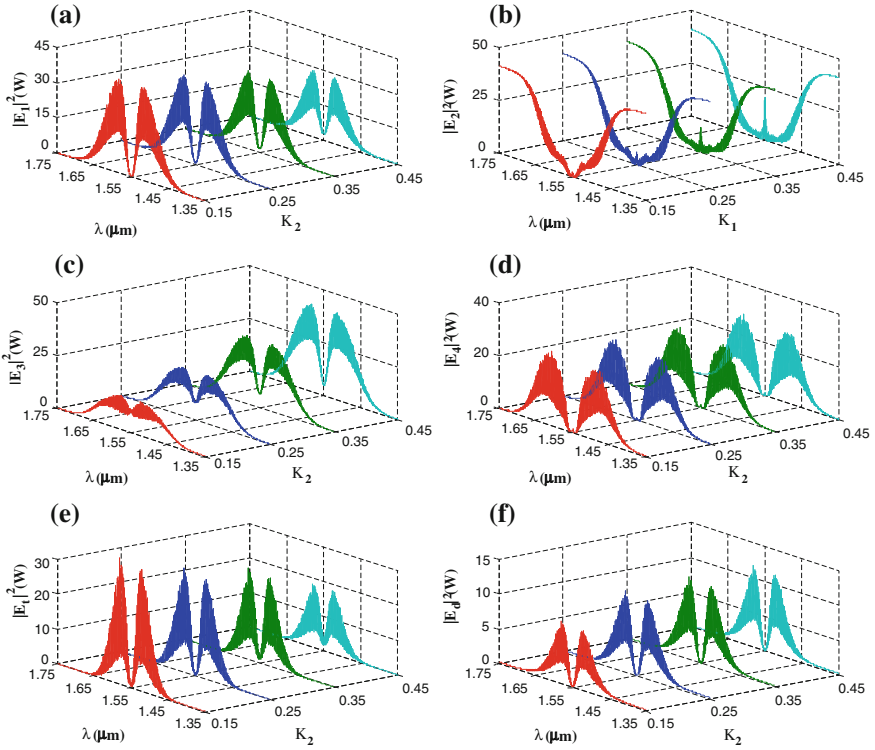

Fig. 5.12 Output signals generated at **a**–**d** circulating fields, **e** throughput port, and **f** drop port of the PANDA system with variable values of κ_2

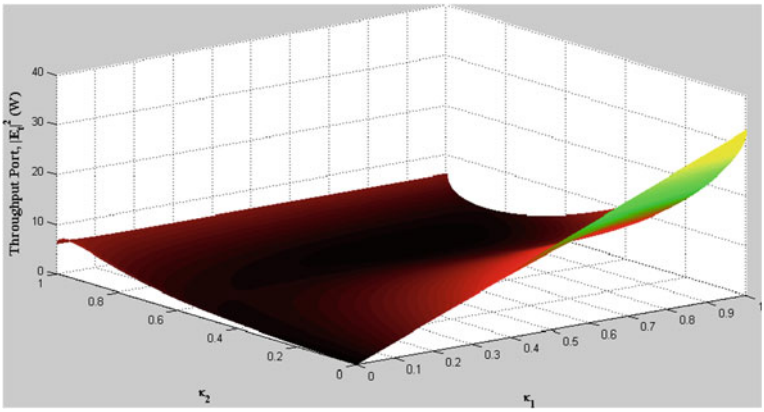

Fig. 5.13 Output power at throughput port plotted against κ_1 and κ_2

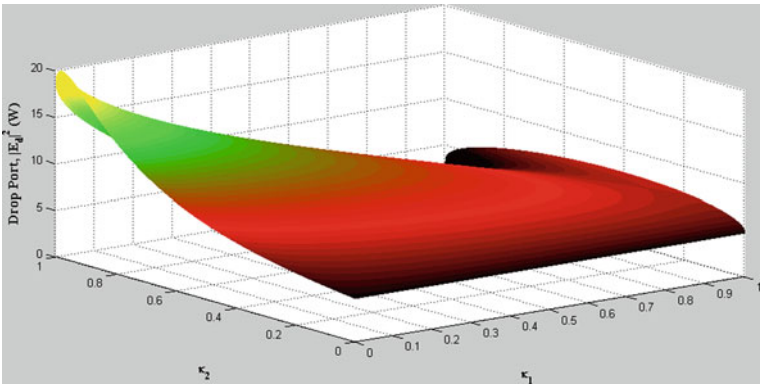

Fig. 5.14 Output power at drop port plotted against κ_1 and κ_2

Figure 5.13 shows the simulation results at throughput port, E_t with varying of κ_1 and κ_2. As shown in Fig. 5.13, E_t reaches to the highest value at the point where κ_1 is equal to one ($\kappa_1 = 1$) and κ_2 is zero ($\kappa_2 = 0$). Based on the theory discussed, none fraction of input light coupled into the ring at drop port for increasing the values of κ_1. Due to the intensity build-up factor, the output power of the system is induced and increased. Zero value of κ_2 means that there is no fraction of light is injected into the system through the second coupler. The highest output power measured at the throughput port, E_t is 34.94 W. The circulated fields within the ring are injected through the first coupler, κ_1 which directly increased the output power at throughput port.

Figure 5.14 shows the 3-D simulation signals ejected at drop port, E_d plotted against κ_1 and κ_2. All the parameters in this case are set as per previous section where the values of κ_1 and κ_2 varies from 0 to 1, and $\kappa_3 = \kappa_4 = 0.2$. The maximum power is achieved at the point where $\kappa_1 = 0$ and $\kappa_2 = 1$. The highest output power recorded is 19.96 W. From Fig. 5.14, the output power does not change for any values of κ_1 where κ_2 is zero. This means that there are no fraction of light coupled into the resonator system for $\kappa_2 = 0$.

5.8.2 Variation of κ_3 and κ_4

The effect of the values of the coupling between microring and two bus waveguides, κ_1 and κ_2 towards the PANDA system are discussed in previous section. In this section, the effect of coupling coefficients between microring and right and left nanorings, κ_3 and κ_4 towards the system are examined.

During the simulation process, dark soliton with $\lambda_o = 1550$ nm and 5 W input power is injected into the system through the input port, E_{in}. The Gaussian beam with 2 W input power is chosen as the control signal and is launched into the system

through the add port, E_{add}. The center microring radius is set at $R = 34$ μm and both right and left nanorings are fixed at $R_R = R_L = 70$ nm respectively. The values of coupling coefficients connected within the center microring and the bus waveguides, κ_1 and κ_2 are kept constant at $\kappa_1 = 0.65$ and $\kappa_2 = 0.40$. As per practical device values, the effective core areas of micro- and nanorings are set at 0.5 μm^2 and 0.2 nm^2 respectively. The waveguide coefficient of the ring, α is set at $\alpha = 0.05$ dB km^{-1} and the fractional coupler intensity loss, γ is set at $\gamma = 0.1$. The obtained output signals generated at throughput and drop ports are analyzed precisely.

The values of κ_3 and κ_4 are varies for 0.1, 0.2, 0.3, 0.4, and 0.5. The output signals at throughput and drop ports of the system are as shown in Fig. 5.15a, b respectively. The values of E_t and E_d shows the increasing pattern with the increase of κ_3 and κ_4. The highest peak powers recorded are 35.26 and 18.71 W for E_t and E_d which corresponds to the values of $\kappa_3 = \kappa_4 = 0.5$ respectively.

As the propagating field from the center microring are entered to the right and left nanorings, the fields resonate in the loop of R_R and R_L. The travelling waves within the waveguide interfere constructively with the input waves. Thus, the intensity in the ring resonator is much higher than its initial input pulse. This shows that the intensity within the ring starts to build-up. The values of coupling coefficients, κ_3 and κ_4 plays an important role in the system performance. As the values of κ_3 and κ_4 increase, the propagating light coupled into the device is increased which increases the power of the circulating fields within the ring and directly induced the amplitude of build-up factor.

The build-up factor, B is the factor by which the total value of the quality being assessed at the point of interest exceeds the value associated with only primary radiation.

The build-up factor, B is given as (Ashkin 1997):

$$B = \left|\frac{E_{r2}}{E_i}\right|^2 = \left|\frac{ix\sqrt{\kappa}ae^{-j\phi^2}}{1 - xyae^{-j\phi}}\right|^2 \tag{5.4}$$

From (5.4), as the values of κ_3 or κ_4 increase, the magnitude of B also increases. Then, the rate of the circulated fields toward the input fields become higher and the intensity within the ring starts to build-up. Due to the dynamical configuration of the PANDA system, any increasing of the coupling coefficient values for the coupler at either sides of the ring results the large amplification of the travelling optical signals. This is due to the intensity build-up process within the right and left nanorings.

The components of light coupled into the ring increases as the values of coupling coefficient, κ increase. As the value of the coupling coefficient decrease to zero ($\kappa = 0$), there is no component of light is coupled into both right and left nanorings. This is because the light passing through the coupler κ_3 and κ_4 are not circulate within either right or left nanorings. As for conclusion, greater values of coupling coefficients, κ are required to produce the higher peak power of the output signals.

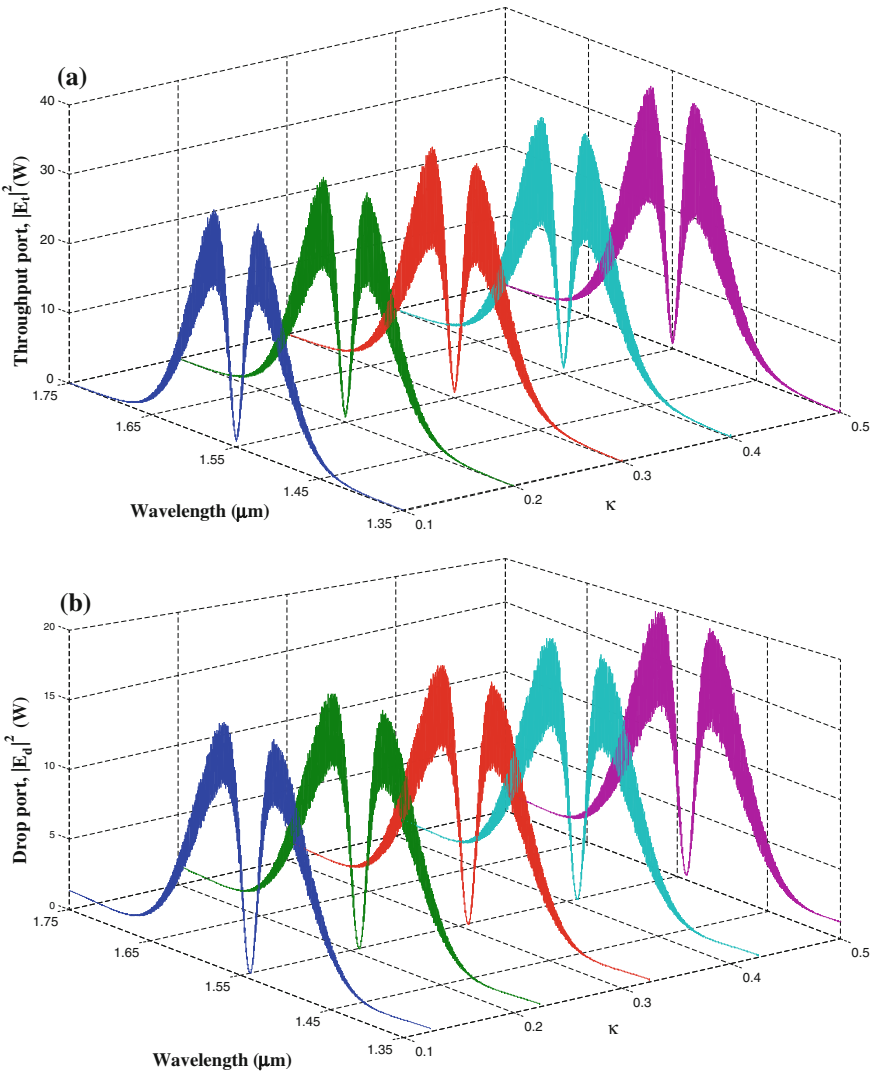

Fig. 5.15 Output signals generated at **a** throughput port and **b** drop port of PANDA system with κ_3 and κ_4 varies for 0.1, 0.2, 0.3, 0.4 and 0.5

5.9 Input Power of PANDA System

Input power is one of very important parameter since it will give big effects towards the system performance. PANDA ring resonator system consists of an input port and an add port, where these two parameters influence the performance of the system at the circulating fields as well as output fields characteristics.

Table 5.3 Values of input and output power of the PANDA system

Input power, E_{in} (W)	Output power (±0.01 W)	
	Throughput port, E_t	Drop port, E_d
5	22.62	10.39
10	38.24	17.48
15	57.86	26.37
20	81.25	37.08
25	108.65	49.62
30	139.94	63.95
35	175.05	80.15
40	214.05	98.16
45	256.97	117.83
50	299.15	139.35

For the purposed, the InGaAsP/InP fibre waveguide with cross sectional area, $A_{eff} = 0.5\ \mu m^2$ is used. The center ring radius is set at $R = 34\ \mu m$ and the right and left nanorings are set at $R_R = R_L = 70$ nm. The linear and nonlinear refractive indexes of the fibre are set at $n_o = 3.34$ and $n_2 = 2.5 \times 10^{-13}\ m^2\ W^{-1}$. The waveguide coefficient is fixed at $\alpha = 0.05\ dB\ km^{-1}$ and the intensity insertion loss coefficient is set at $\gamma = 0.1$. In order to examine the effect of the input power, E_{in} towards the system, the values of input power varies from 5 to 50 W respectively. The input power of the control signal is maintained at $E_{add} = 2$ W.

Table 5.3 shows the values of simulation results obtained at the throughput and drop ports of respectively. From the data collected, it is shown that the values of output power increases with increase of the input power, E_{in}. The relationship between the input power and the output power for both throughput and drop ports are presented in Fig. 5.16.

From the graph plotted in Fig. 5.16, it can be seen that the output power of the system increases exponentially with the increase in the values of input power, E_{in}. This is significantly related from the theoretical calculation where:

$$E = Ae^{i(kz-\omega t)} \tag{5.5}$$

$$E^2 = A^2 e^{2i(kz-\omega t)} \tag{5.6}$$

Hence,

$$P \propto E^2. \tag{5.7}$$

Equation (5.7) proved that the values of output power (E_t and E_d) are exponentially increase with increases of the values of input power, E_{in}.

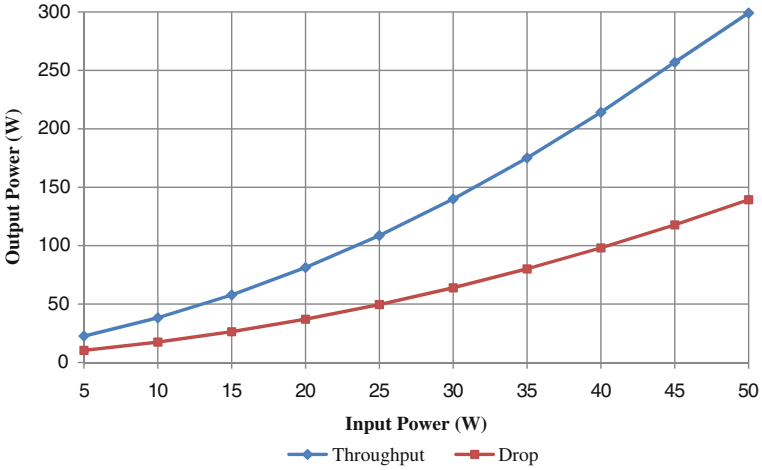

Fig. 5.16 Relationship between input and output power at throughput and drop ports of the PANDA system

5.10 Optimization of PANDA Ring Resonator System

The dynamical behaviour of the optical signals generated from PANDA ring resonator system is demonstrated and discussed. The tunability of such signals can be obtained by varying and controlling the important parameters of the system. For convenience analysis, the circulated fields within the ring are represented by E_1, E_2, E_3, and E_4 while the output fields at throughput and drop ports of the system are depicted as E_t and E_d respectively. The key parameters are tuned and varied in order to optimize the output signals generated. For instance, the center ring radius, R is chosen at $R = 34$ μm and the radii of the right and left nanorings are chosen at $R_R = R_L = 70$ nm respectively. The coupling coefficient values are set at $\kappa_1 = 0.85$, $\kappa_2 = 0.80$, and $\kappa_3 = \kappa_4 = 0.50$. The effective core area of the microring is fixed at $A_{eff} = 0.5$ μm^2 and $A_{eff} = 0.2$ nm^2 for the right and left nanorings. The attenuation coefficient, α is fixed at $\alpha = 0.05$ dB km^{-1} and the intensity insertion loss coefficient of the coupler, γ is set at $\gamma = 0.1$.

5 W input dark soliton with 50 ns pulse width is launched into the system through the input port, E_{in} and the Gaussian beam with 2 W input power is injected into the system via add port, E_{add}. The optical signals are generated at center wavelength, $\lambda_o = 1550$ nm as shown in Fig. 5.17. Figure 5.17a–h represent the input dark soliton, Gaussian beam, E_1 field, E_2 field, E_3 field, E_4 field, throughput port, and drop port respectively. The values of throughput and drop ports for the optimized system are calculated at $E_t = 37.93$W and $E_d = 24.28$ W as shown in Fig. 5.7.

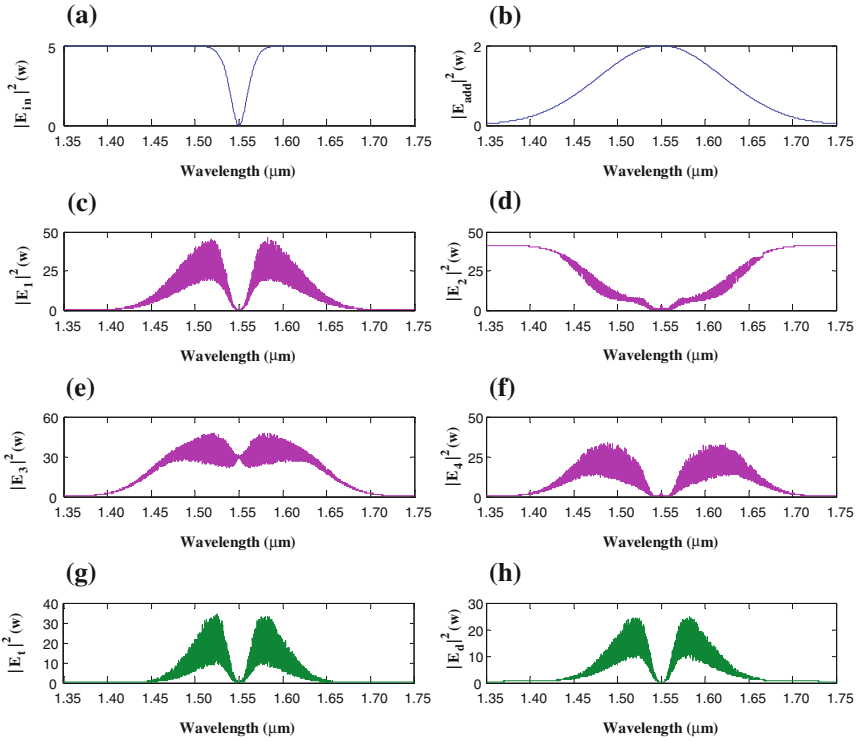

Fig. 5.17 Optimized signals for PANDA configuration system where **a** dark soliton, **b** Gaussian beam, **c–f** circulating fields E_1, E_2, E_3, and E_4, **g** throughput port, and **h** drop port

5.11 Optical Tweezers for Photodetector Performance Improvement

By using the proposed system designed, the optical waveguide can be used to trap the electrons/atoms. The photodetector device can be constructed incorporating with the optical tweezers assembly. The trapped electron can be transferred from anode to cathode contacts via the optical waveguide. In the simulation process, the input signals are dark soliton and Gaussian beam with peak power of 100 mW. The ring radii of the system are set at $R = 20$ μm and $R_R = R_L = 5$ μm respectively.

The coupling coefficients of the PANDA ring resonator are set to be $\kappa_1 = \kappa_2 = \kappa_3 = \kappa_4 = 0.5$. The effective core area, A_{eff} of the fibre is set at $A_{eff} = 300\ \mu m^2$. The waveguide loss coefficient, α and the coupling loss of the fibre, γ are set at $\alpha = 0.3\ dB\ km^{-1}$ and $\gamma = 0.1$ respectively. The dimensions of the optical tweezers are controlled by using various tweezers size, ranging from 100 to 250 μm.

Figure 5.18 shows the results of different center wavelengths. The wavelength of the tweezers are 1.45, 1.50, 1.55, and 1.65 μm for the red, green, blue, and black colours respectively. The shapes of the fields are different for each center wavelength plotted. The highest peak signal of optical tweezers is obtained for the wavelength of 1.55 μm.

Figure 5.19 shows the comparison of the highest peak output at throughput and drop ports respectively. The optical tweezers generated at throughput and drop ports of the system can trap electrons and deliver to the contacts. The tweezers generated at throughput port is more suitable than drop port. The optical tweezers of drop port may not be strong enough, in which the trapped electrons can escape during the transportation process. The dimension of optical tweezers can be adjusted to form the various tweezers sizes, which are required to fit the electrons sizes. Therefore, the design optical tweezers sizes are important for each trapping electrons. When the optical tweezers are too large, then the electrons can escape from the trap.

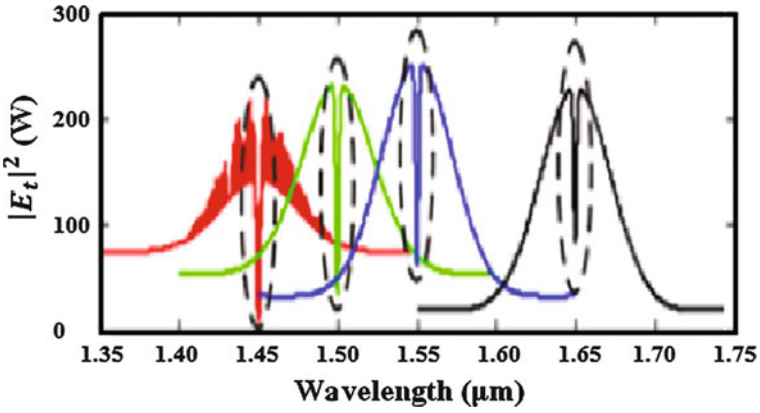

Fig. 5.18 Signals generation at different center wavelength

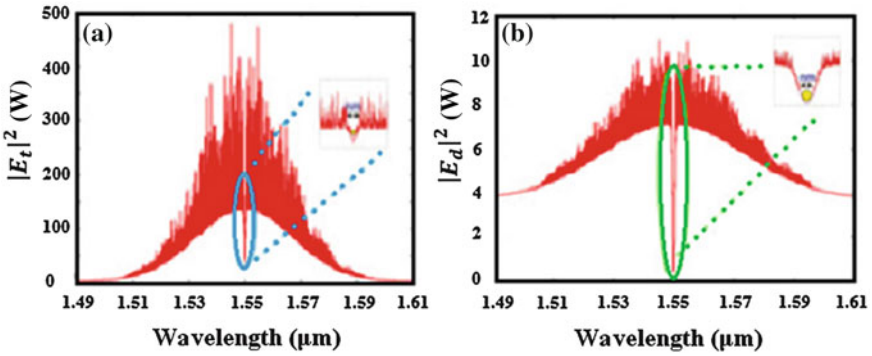

Fig. 5.19 Comparison of output power where **a** throughput, **b** drop ports

The optical tweezers cannot be used to trap electrons when the tweezers size is too small.

In application, the different sizes of traps can be generated as shown in Fig. 5.20. In practice, the optical tweezers can propagate within the optical waveguide. This means that the trapped electrons can transport to the required destinations by using the optical fibre or waveguide. By using the proposed model system designed, electrons can be trapped via the suitable waveguide and transported to the required

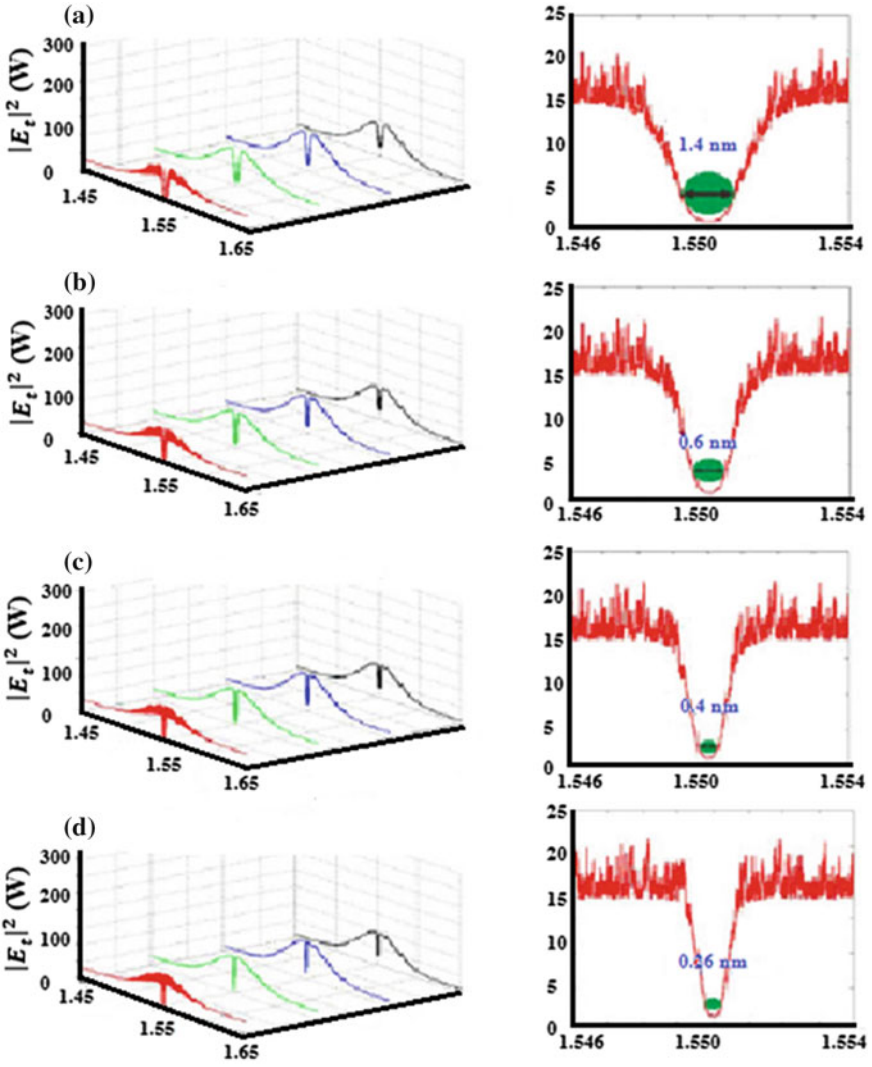

Fig. 5.20 Different trapping sizes

targets or destinations. It is found that the photodetector speed can be increased to more than the normal photodetector speed for about 3×10^5 times.

From the results obtained, the photodetector performance improvement can be achieved and seen. It is found that the trapped electrons from the depletion region can transport and reach to the cathode contact with the speed increasing up to 3×10^5 times from the normal condition. Furthermore, this technique can also be used to improve the device performances such as molecular accelerator, capacitor, solar cells, and other semiconductor devices.

The calculation is carried out by using the simple relationships where:

$$s = v \cdot t \tag{5.8}$$

$$s = \left(\frac{c}{n}\right) \cdot t \tag{5.9}$$

and

$$2\pi r = \frac{c}{n} \cdot t \tag{5.10}$$

Here, s is an electron traveling distance, c is the speed of light in vacuum, n is the device reflective index, t is the traveling time, and r is the ring radius.

A solar cell embedded with particle accelerator using an optical tweezers for photodetector performance improvement is proposed. The optical tweezers are generated using dark soliton as carrier signal, while the Gaussian beam is used as the control signal within the device. By using an optical tweezers, it is shown that the electron particles can be trapped and formed the electrical carriers to the device contacts via an optical waveguide. In this case, the optical tweezers are generated and controlled within a PANDA ring resonator system, where finally the photodetector speed can be increased by the accelerated electrons.

Chapter 6
Conclusion

This research explained and described in details the formation of ring resonator systems and output signals as generated by dark soliton input pulse propagated within micro- and nanoring resonator systems controlled by Gaussian beam. There were two different systems being considered, namely as add-drop configuration system and PANDA ring resonator system. The characteristics of the output signals for both systems were observed and discussed in details.

The research has designed, demonstrated, and analyzed the optical soliton control within optical micro- and nanoring resonator systems. The characteristics of the add-drop configuration system and PANDA ring resonator system have been investigated. The analytical formulation and derivation of the transfer function have been developed and the parametric effect of each model designed been examined accordingly. The dynamical behaviour of the circulating fields and output signals generated within micro- and nanoring resonator systems have been investigated and analyzed in details. At the end, the ring resonator system parameters have been optimized.

The dynamical behaviour of such signals has been investigated for the microring radius in range of 20–40 μm and nanorings radii range from 40 to 90 nm respectively. The coupling coefficient values have been investigated for the range of 0–1. In this research, the input power, E_{in} and control signal, E_{add} were set at 5 and 2 W respectively. For instance, certain parameters were fixed, such as $n_o = 3.34$, $n_2 = 2.5 \times 10^{-13}$ m^2 W^{-1}, $A_{eff} = 0.5\,\mu m^2$, $\alpha = 0.5$ dB km^{-1}, and $\gamma = 0.1$ respectedly.

For add-drop configuration system, with $R = 34$ μm, $\kappa_1 = 0.75$, $\kappa_2 = 0.80$, and center wavelength, $\lambda_0 = 1550$ nm, the highest peak power was obtained at throughput, E_t and drop, E_d ports were recorded at 3.84 and 2.91 W respectively. For PANDA ring resonator system, the highest output power generated at E_t and E_d were recorded at 37.93 and 24.28 W respectively. This results obtained by the operating system where $R = 34$ μm, $R_R = R_L = 70$ nm, $\kappa_1 = 0.85$, $\kappa_2 = 0.80$, and $\kappa_3 = \kappa_4 = 0.20$.

S. Daud et al., *Simulation of Optical Soliton Control in Micro- and Nanoring Resonator Systems*, SpringerBriefs in Physics, DOI 10.1007/978-3-319-15485-5_6

Results obtained shows that the output power generated increased with increase in the input power, E_{in}. By comparing both systems studied, the output power of add-drop system was less, due to the losses of the system waveguides itself. But, it's FWHM and FSR number remained constant. This was very useful for the large system link which is very important in communication technology. With the additional right and left nanorings in PANDA system, only small input signals with less power amplitudes was required to produce reasonable trapping system to generate the optical trapping fields and tweezers.

References

Abdullaev, F. K., Darmanyan, S., & Khaibibulaev, P. (1993). *Optical soliton*. Berlin: Springer.

Ablowitz, M. J., & Clarkson, P. A. (1991). *Soliton, nonlinear evolution equations, and inverse scattering*. New York: Cambridge University Press.

Absil, P. P. (2000). *Microring resonators for wavelength division multiplexing and integrated photonics applications*. College Park: University of Maryland.

Absil, P. P., Hryniewicz, J. V., Little, B. E., Wilson, R. A., Joneckis, L. G., & Ho, P. T. (2000). Compact microring notch filters. *IEEE Photonics Technology Letters, 12*(4), 398–400.

Agrawal, G. P. (2001). *Applications of nonlinear fiber optics*. San Diego, CA: Academic Press.

Amiri, I. S. (2013). *Optical soliton based communication using micro ring resonator*. Doctor of Philosophy. Skudai: Universiti Teknologi Malaysia.

Ashkin, A. (1997). Optical trapping and manipulation of neutral particles using lasers. *Proceedings of the National Academy of Science, 94*(10), 4853–4860.

Ashkin, A. (2000). History of optical trapping and manipulation of small-neutral particle, atoms, and molecules. *IEEE Journal on Selected Topics in Quantum Electronics, 6*(6), 841–856.

Ashkin, A., & Dziedzic, J. M. (1987). Optical trapping and manipulation of virusses and bacteria. *Journal of Science, 235*(4795), 1517–1520.

Attaway, S. (2011). *Matlab: A practical introduction to programming and problem solving* (2nd ed.). Waltham: Elsevier.

Aziz, M. S. (2013). *Optical tweezers induced in microring resonator*. Doctor of Philosophy. Skudai: Universiti Teknologi Malaysia.

Aziz, M. S., Suwanpayak, N., Jalil, M. A., Jomtarak, R., Saktioto, T., Ali, J., & Yupapin, P. P. (2012). Gold nanoparticle trapping and delivery for therapeutic applications. *International Journal of Nanomedicine, 7*, 11–17.

Bahadoran, M. (2013). *Analytical vernier effect for nanophotonics circuits using ring resonator*. Doctor of Philosophy. Skudai: Universiti Teknologi Malaysia.

Barton, J. P. (1995). Internal and near-surface electromagnetic fields for a spheroidal particle with arbitrary illumination. *Apply Optics, 34*(24), 5542–5551.

Bonessi, D., Bonin, K., & Walker, T. (2007). Optical forces on particles of arbitrary shape and size. *Journal of Optics A: Pure and Applied Optics, 9*(8), S228–S234.

Boyd, R. W. (2001). *Nonlinear optics*. San Diego, CA: Academic Press.

Butcher, P. N., & Cotter, D. (1990). *The elements of nonlinear optics*. Cambridge: Cambridge University Press.

Calander, N., & Willander, M. (2002). Optical trapping of single fluorescent molecules at the detection spots of nanoprobes. *Physical Review Letters*, *89*(14), 143603/1–143603/4.

Chen, C. L. (2006). *Foundations for guided-wave optics*. New York: Wiley.

Chen, S. L., Huang, S. W., Ling, T., Ashkenazi, S., & Guo, L. J. (2009). Polymer microring resonators for high-sensitivity and wideband photoacoustic. *IEEE Transactions on Ultrasonics, Ferroelectrics, and Frequency Control, 56*(11), 2482–2491.

S. Daud et al., *Simulation of Optical Soliton Control in Micro- and Nanoring Resonator Systems*, SpringerBriefs in Physics, DOI 10.1007/978-3-319-15485-5

Chen, W. H., Wilson, J. D., Wijeratne, S. S., Southmayd, S. A., Lin, K. J., & Kiang, C. H. (2012). Principles of single-molecule manipulation and its application in biological physics. *International Journal of Modern Physics B*, *26*(13), 16.

Chin, M. K., Youtsey, C., Zhao, W., Pierson, T., Ren, Z., Wu, S. L., et al. (1999). GaAs microcavity channel-dropping filter based on a race-track resonator. *IEEE Photonics Technology Letters, 11*(12), 1620–1622.

Chu, D. Y., Chin, M. K., Sauer, N. J., & Xu, Z. (1993). InGaAs/InAlGa as quantum-well microdisk lasers. *IEEE Photonics Technology Letters, 5*, 1353–1355.

Crisafuli, F. A. P., Cesconetto, E. C., Ramos, E. B., & Rocha, M. S. (2012). DNA-Isplatin interaction studied with single molecule stretching experiments. *Integrative Biology, 4*(5), 568–574.

Dai, L., Zhang, B., Mair, R. A., Zeng, K., Lin, J., Jigang, H., Botchkarev, A., & Khan, M. A. (1998). Optical Properties and Resonant Modes in GaN/AlGaNandInGaN/GaN Multiple Quantum Well Microdisk Cavities. In *Semiconductor Lasers III*. Beijing, China.

Dienerowitz, M., Mazilu, M., & Dholakia, K. (2008). Optical manipulation of nanoparticles: A review. *Journal of Nanophotonics, 2*(1), 021857.

Djordjev, K., Choi, S. J., & Dapkus, P. D. (2002a). Active semiconductor microdisk devices. *Journal of Lightwave Technology, 20*(1), 105–113.

Djordjev, K., Choi, S. J., & Dapkus, P. D. (2002b). Vertically coupled InP microdisk switching devices with electroabsorptive active regions. *IEEE Photonics Technology Letters, 14*(8), 1115–1117.

Douglas, B., Keith, B., & Thad, W. (2007). Optical forces on particles of arbitrary shape and size. *Journal of Optics A: Pure and Applied Optics, 9*(8), S228.

Drazin, P. G. (1993). *Solitons: An introduction*. New York: Cambridge University Press.

Fangohr, H. (2004). A comparison of C, matlab and python as teaching languages in engineering. In *Computational Science-ICCS, 4th International Conference* (Vol. 3039). Kraków, Poland.

Fazal, F. M., & Block, S. M. (2011). Optical tweezers study life under tension. *Nature Photonics, 5*(6), 318–321.

Geuzebroek, D. (2005). *Flexible optical network components based on densely integrated microring resonators*. Doctor of Philosophy. University of Twente.

Gu, C. H. (1995). *Soliton theory and its applications*. New York: Springer.

Guck, J., Ananthakrishnan, R., Mahmood, H., Moon, T. J., Cunningham, C. C., & Käs, J. (2001). The optical stretcher: a novel laser tool to micromanipulate cells. *Biophysical Journal, 81*(2), 767–784.

Hagness, S. C., Rafizadeh, D., Ho, S. T., & Taflove, A. (1997). FDTD microcavity simulations: Design and experimental ralization of waveguide-coupled single-Mode ring and whispering-gallery-mode disk resonator. *IEEE Journal of Lightwave Technology, 15*(11), 2145–2165.

Hahn, D. W. (2006). *Light scattering theory.* Department of Mechanical and Aeorospace Engineering, University of Florida.

Harada, Y., & Asakura, T. (1996). Radiation forces on a dielectric sphere in the rayleigh scattering regime. *Optics Communications, 124*(5–6), 529–541.

Heebner, J. E., Lepeshkin, N. N., Wicks, G. W., Boyd, R. W., Grover, R., & Ho, P. T. (2004). Enhanced linear and nonlinear optical phase response of algaas microring resonators. *Optics Letters, 29*(7), 769–771.

Heebner, J., Grover, R., & Ibrahim, T. (2008). *Introduction to optical microresonators* (pp. 1–7). Berlin/Heidelberg: Springer.

Ishii, Y., Ishijima, A., & Yanagida, T. (2001). Single molecule nanomanipulation of biomolecules. *Trends in Biology, 19*(6), 211–216.

Jalil, M. A. (2013). *Dark-bright solitons conversion in ring resonator within an add-drop filter towards nanomedicine applications*. Doctor of Philosophy. Skudai: Universiti Teknologi Malaysia.

Jalil, M. A., Innate, K., Suwanpayak, N., Yupapin, P. P., & Ali, J. (2011). Molecular diagnosis using multi drug delivery network and stability. *Artificial Cells, Blood Substitutes, and Biotechnology, 39*(6), 357–365.

Ke, P. C., & Gu, M. (1999). Characterization of trapping force on metallic mie particles. *Applied Optics, 38*(1), 160–167.

Kivshar, Y. S., & Agrawal, G. (2003). *Optical solitons: From fibers to photonic cristals*. Boston: Academic Press.

Kivshar, Y. S., & Agrawal, G. P. (2003). *Optical solitons: From fibers to photonic crystals*. USA: Elsevier Science.

Little, B. E., Chu, S. T., Haus, H. A., Foresi, J., & Laine, J. P. (1997). Microring resonator channel dropping filters. *Journal of Lightwave Technology, 15*(6), 998–1005.

Liu, Z., & Zhao, D. (2012). Radiation forces acting on a rayleigh dielectric sphere produced by highly focused elegant Hermite-Cosine-Gaussian beams. *Optics Express, 20*(3), 2895–2904.

Madsen, C. K., & Zhao, J. H. (1996). A general planar waveguide autoregressive optical filter. *IEEE Journal of Lightwave Technology, 14*(3), 437–447.

Marcatili, E. A. J. (1969). Bends in optical dielectric guides. *Bell System Technical Journal, 48*(7), 2103–2132.

Mario, F. S. (2007). Nonlinear effect in optical fibers: Limitations and benefits. *Proceedings of SPIE, 6793*, 1–10.

Masi, M., Orobtchouk, R., Fan, G., Fedeli, J. M., & Pavesi, L. (2010). Towards a realistic modelling of ultra-compact racetrack resonators. *Journal of Lightwave Technology, 28*(22), 3233–3242.

Mason, S. J. (1953). Feedback theory: Some properties of signal flow graphs. *Proceedings of IRE, 44*(7), 920–926.

McAulay, A. (2005). Nonlinear Microring resonators for all-optical switch. *Laser Focus World, 41* (11), 127–130.

Melnichuk, M., & Wood, L. T. (2010). Direct Kerr electro optic effect in noncentrosymmetric materials. *Physical Review A, 82*(1), 013821.

Minzioni, P., Bragheri, F., Liberale, C., Di Fabrizio, E., & Cristiani, I. (2008). A novel approach to fiber-optic tweezers: Numerical analysis of the trapping efficiency. *IEEE Journal of Selected Topics in Quantum Electronics, 14*(1), 151–157.

Mitatha, S., Moongfangklang, N., Jalil, M. A., Suwanpayak, N., Ali, J., & Yupapin, P. P. (2011). Multi-access drug delivery network and stability. *International Journal of Nanomedicine, 6*, 1757–1764.

Mitatha, S., Putthacharoen, R., & Yupapin, P. P. (2012). THz frequency bands generation for radio-over-fiber systems. *International Journal for Light and Electron Optics, 123*(11), 974–977.

Moffitt, J. R., Izhaky, D., & Bustamante, C. (2006). Differential detection of dual traps improves the spatial resolution of optical tweezers. *Proceedings of the National Academy of Sciences of the United States of America, 103*(24), 9006–9011.

Neuman, K. C., Lionnet, T., & Allemand, J. F. (2007). Single-molecule micromanipulation techniques. *Annual Review of Materials Research, 37*, 33–67.

Neuman, K. C., & Block, S. M. (2004). Optical trapping. *Review of Scientific Instruments, 75*(9), 2787–2809.

Newell, A. C. (1995). Solitons in mathematics and physics. In *MS-NSF Regional Conference Series in Applied Mathematics* (Vol. 48). Philadelphia: SIAM.

Parkin, S., Knöner, G., Nieminen, T. A., Heckenberg, N. R., & Rubinsztein-Dunlop, H. (2006). measurement of the total optical angular momentum transfer in optical tweezers. *Optics Express, 14*(15), 6963–6970.

Polar, A., Threepak, T., Mitatha, S., Bunyatnoparat, P., & Yupapin, P. P. (2009). New wavelength division multiplexing bands generated by using a Gaussian pulse in a microring resonator system. In *Communications and information technology* (pp. 1063–1064).

Poon, J., Scheuer, J., Mookherjea, S., Paloczi, G. T., Huang, Y., & Yariv, A. (2004). Matrix analysis of microring coupled-resonator optical waveguides. *Optics Express, 12*(1), 90–103.

Pralle, A., Prummer, M., Florin, E. L., Stelzer, E. H., & Horber, J. K. (2000). Three-dimensional high-resolution particle tracking for optical tweezers by forward scattered light. *Microscopy Research and Technique, 44*(5), 378–386.

Qiu, C., & Xu, Q. (2011). Controlling normal incident optical waves with an integrated resonator. *Optics Express, 19*(27), 26905–26910.

Rabiei, P., & Steier, W. H. (2003). Tunable polymer double micro-ring filters. *IEEE Photonics Technology Letters, 15*(9), 1255–1257.

Rabiei, P. (2005). Calculation of losses in microring resonators with arbitrary refractive index or shape profile and its applications. *Journal of Lightwave Technology, 23*(3), 1295–1301.

Rabus, D. G., Hamacher, M., & Heidrich, H. (2002). Resonance frequency tuning of a double ring resonator in GaInAsP/InP: experiment and simulation. *Japanese Journal of Applied Physics, Part 1: Regular Papers and Short Notes and Review Papers*, *41*(2B), 1186–1189.

Rabus, D. G., & Hamacher, M. (2001). MMI-coupled ring resonators in GaInAsP-InP. *IEEE Photonics Technology Letters, 13*(8), 812–814.

Rabus, D. G., Hamacher, M., Heidrich, H., & Troppenz, U. (2002a). Box-like filter response of triple ring resonators with integrated SOA sections based on GaInAsP/InP. *Einsteinufer, 37*, 479–482.

Rabus, D. G., Hamacher, M., Heidrich, H., & Troppenz, U. (2002b). High-Q Channel-dropping filters using ring resonators with integrated SOAs. *IEEE Photonics Technology Letters, 14*(10), 1442–1444.

Rabus, D. G., Hamacher, M., Heidrich, H., & Troppenz, U. (2002c). Optical filters based on ring resonators with integrated semiconductor optical amplifiers in GaInAsP-InP. *IEEE Journal on Selected Topics in Quantum Electronics, 8*(6), 1405–1411.

Rabus, D. G. (2010). *Integrated ring resonators: The compendium*. Berlin: Springer.

Rafizadeh, D. (1997). *Experimental realization of nanofabricated semiconductor waveguide-coupled microcavity ring and disk optical resources*. Doctor of Philosophy. Northwestern University.

Rohrbach, A., & Stelzer, E. H. K. (2001). Optical trapping of dielectric particles in arbitrary fields. *Journal of the Optical Society of America A: Optics and Image Science, and Vision, 18*(4), 839–853.

Saeung, P., & Yupapin, P. P. (2008). A design of optical ring resonator filters for WDM applications. *Journal of Nonlinear Optical Physics and Materials (JNOPM), 17*(1), 111–118.

Sarapat, K., Ali, J., Yupapin, P. P., Worrarutkul, A., & Khunnam, W. (2009). White light generation and amplification using a soliton pulse within a nanowaveguide. *Physics Procedia, 2*, 53–57.

Serpengüzel, A. (1999). Semiconductor and dielectric mcrocavity spectroscopy. *Turkish Journal of Physics, 23*, 701–707.

Shen, Y. R. (1984). *Principls of nonlinear optics*. New York: Wiley.

Singh, S. P., & Singh, N. (2007). Nonlinear effects in optical fibers: origin, management and applications. *Progress in Electromagnetics Research, 73*, 249–275.

Stilgoe, A. B., Nieminen, T. A., Knöener, G., Heckenberg, N. R., & Rubinsztein-Dunlop, H. (2008). The effect of mie resonances on trapping in optical tweezers. *Optics Express, 16*(19), 15039–15051.

Stokes, L. F., Chodorow, M., & Shaw, H. J. (1982). All-single-mode fiber resonator. *Optics Letters, 7*(6), 288–290.

Sumetsky, M., Digiovanni, D. J., Dulashko, Y., Fini, J. M., Liu, X., Monberg, E. M., et al. (2002). Surface nanoscale axial photonics: Robust fabrication of high-quality-factor microresonators. *Optics Letter, 36*(24), 4824–4826.

Summers, M. D. (2009). *Optical manipulation of aerosols*. North Haugh: School of Physics and Astronomy. Universitu of St. Andrews

Suwanpayak, N., Teeka, C., & Yupapin, P. P. (2011). Hybrid transistor manipulation controlled by light. *Microwave and Optical Technology Letters, 53*(11), 2533–2537.

Suwanpayak, N., Jalil, M. A., Aziz, M. S., Ismail, F. D., Ali, J., & Yupapin, P. P. (2011). Blood cleaner on-chip design for artificial human kidney manipulation. *International Journal of Nanomedicine, 6*, 957–964.

Svoboda, K., & Block, S. (1994). Biological applications of optical forces. *Annual Review of Biophysics and Biomolecular Structure, 23*(1), 247–285.

Tan, F. (2004). *Integrated optical filters based on microring resonators*. Doctor of Philosophy. University of Twente.

Tasakorn, M., Suwanpayak, N., & Yupapin, P. P. (2012). Blood circulation network incorporation an artificial bone for real time operation. *Journal of Nonlinear Optical Physics and Materials* (pp. 102–105).

Tian, B., & Gao, Y. T. (2005). Symbolic-computation study of the perturbed nonlinear Schrödinger model in inhomogeneous optical fibers. *Physics Letter A., 3*, 228–236.

Timotijevic, B. D., Gardes, F. Y., Headley, W. R., & Masanovic, G. Z. (2006). Multi-stage racetrack resonator filters in silicon-on-insulator. *Journal of Optics A: Pure and Applied Optics, 8*(7), S473–S476.

Turner, A. C., Foster, M. A., Gaeta, A. L., & Lipson, M. (2008). Ultra-low power parametric frequency conversion in a silicon microring resonator. *Optics Express, 16*(7), 4881–4887.

Ulrich, R., & Weber, H. P. (1972). Unidirectional thin-film ring laser. *Applied Physics Letters, 20* (1), 38–40.

Van Mameren, J., Wuite, G. J. L., & Heller, I. (2011). Introduction to optical tweezers: background, system designs, and commercial solutions. *Applied Optics*, *783*, 1–20.

Vanderhaegen B., Rabus, D. G., Hamacher, M., Troppenz, U., & Heidrich, H. (1999). *High Q GaInAsP ring resonator filters* (pp. 381–384). ECIO'99. Torino Italy.

Weber, H. P., & Ulrich, R. (1971). A Thin Film Ring Laser. *Applied Physics Letters., 19*(2), 38–40.

Wen, J. L., Bo, T., Tao, X., Kun, S., & Yan, J. (2010). Bright and dark solitons in the normal dispersion regime on inhomogeneous optical fibers: soliton interaction and soliton control. *Annals of Physics, 32*, 1633–1643.

Wilson, L., Besseling, R., Arlt, J., Poon, W. C. K., Dholakia, K., & Spalding, G. C. (2005). Optical trapping and optical micromanipulation II. *SPIE, 5930*, 71.

Yang, Y., Lou, C., Zhou, H., Wang, J., & Gao, Y. (2006). Simple pulse compression scheme based on filtering self-phase modulation-broadened spectrum and its application in an optical time-division multiplexing system. *Apply Optics, 45*(28), 7524–7528.

Yariv, A. (2000). Universal relations for coupling of optical power between microresonators and dielectric waveguides. *Electronics Letters, 36*(4), 320–322.

Yariv, A. (2002). Critical coupling and its control in optical waveguide ring resonator systems. *IEEE Photonics Technology Letters, 14*(4), 483–485.

Yupapin, P. P., & Suchat, A. (2007). Entangled photon generation using fiber optic mach-zehnder interferometer incorporating the nonlinear effect in a fiber ring resonator. *SPIE: Journal of Nanophotonics*, *1*, 013504.

Yupapin, P. P., Pornsuwancharoen, N., & Chaiyasoonthorn, S. (2008). Attosecond pulse generation using the multistage nonlinear microring resonators. *Microwave and Optical Technology Letters, 50*(12), 3108–3111.

Yupapin, P. P., & Pornsuwanchareon, N. (2008). *Guided wave optics and photonics: microring resonator design for telephone network security*. New York: Nova Science Publisher Inc.

Yupapin, P. P. (2010). Generalized quantum key distribution via microring resonator for mobile telephone networks. *Optics Letter, 121*(5), 422–425.

Zabusky, N. J. (1965). Interpretation of the stabilization distance as evidence of weak shock formation in low-loss longitudinal nonlinear wave propagation experiments. *Journal of Physics and Chemistry of Solids, 26*, 955–958.

Index

S. Daud et al., *Simulation of Optical Soliton Control in Micro- and Nanoring Resonator Systems*, SpringerBriefs in Physics, DOI 10.1007/978-3-319-15485-5